https://doi.org/10.15388/vu.thesis.974
https://orcid.org/0009-0004-4944-112X

VILNIUS UNIVERSITY

Artūras Polita

Design and Application of BODIPY Probes for Fluorescence Lifetime Imaging of Local Viscosity and Polarity in Lipid Microenvironments

DOCTORAL DISSERTATION

Natural Sciences,
Biophysics (N 011)

VILNIUS 2026

This dissertation was written between 2022 and 2026 at Vilnius University.

Academic supervisor – **Dr. Gintaras Valinčius** (Vilnius University, Natural Sciences, Biophysics – N 011).

Dissertation Defence Panel:
Chair – **Prof. Dr. Saulius Bagdonas** (Vilnius University, Natural Sciences, Biophysics – N 011).
Members:
Dr. Lena Golubewa (Vilnius University, Natural Sciences, Chemistry – N 003).
Dr. Gražvydas Lukinavičius (Max Planck Institute for Multidisciplinary Sciences, Natural Sciences, Biochemistry – N 004).
Prof. Dr. Daumantas Matulis (Vilnius University, Natural Sciences, Biophysics – N 011).
Dr. Arūnas Stirkė (Center for Physical Sciences and Technology, Natural Sciences, Biophysics – N 011).

The dissertation shall be defended at a public meeting of the Dissertation Defense Panel at 13 a.m. on 7th September 2026 at the Life Sciences Center of Vilnius University, auditorium R401. Address: Saulėtekio al. 7, LT-10223, Vilnius, Lithuania, tel. +370 5 223 4419; e-mail: info@gmc.vu.lt

https://doi.org/10.15388/vu.thesis.974
https://orcid.org/0009-0004-4944-112X

VILNIAUS UNIVERSITETAS

Artūras Polita

Fluorescencijos gyvavimo trukmės jutiklių kūrimas ir taikymas lokalios klampos ir poliškumo vaizdinimui lipidinėse mikroaplinkose

DAKTARO DISERTACIJA

Gamtos mokslai,
Biofizika (N 011)

VILNIUS 2026

Disertacija rengta 2022 – 2026 metais Vilniaus universitete.

Mokslinis vadovas – **dr. Gintaras Valinčius** (Vilniaus universitetas, gamtos mokslai, biofizika – N 011).

Gynimo taryba:
Pirmininkas – **prof. dr. Saulius Bagdonas** (Vilniaus universitetas, gamtos mokslai, biofizika – N 011).
Nariai:
dr. Lena Golubewa (Vilniaus universitetas, gamtos mokslai, chemija – N 003).
dr. Gražvydas Lukinavičius (Makso Planko institutas, Vokietija, gamtos mokslai, biochemija – N 004.)
prof. dr. Daumantas Matulis (Vilniaus universitetas, gamtos mokslai, biofizika - N 011).
dr. Arūnas Stirkė (Fizinių ir technologijos mokslų centras, gamtos mokslai, biofizika – N 011).

Disertacija ginama viešame Gynimo tarybos posėdyje 2026 m. rugsėjo mėnesio 7 d. 13 val. Vilniaus universiteto Gyvybės mokslų centro R401 auditorijoje. Adresas: Saulėtekio al. 7, LT-10223, Vilnius, Lietuva, tel. +370 5 223 4419; el. paštas: info@gmc.vu.lt.

Table of Contents

Abbreviations

Lipids

- DOPC: 1,2-dioleoyl-sn-glycero-3-phosphocholine
- DPPC: 1,2-dipalmitoyl-sn-glycero-3-phosphocholine
- BSM: brain sphingomyelin
- Chol: cholesterol

Membrane systems

- GUVs: giant unilamellar vesicles
- MLVs: multilamellar vesicles
- LUVs: large unilamellar vesicles
- GPMVs: giant plasma membrane vesicles
- tBLMs: tethered bilayer lipid membranes

Fluorescence techniques

- FLIM: fluorescence lifetime imaging microscopy
- TCSPC: time-correlated single photon counting
- IRF: instrument response function

Photophysical mechanisms

- ICT: intramolecular charge transfer
- TICT: twisted intramolecular charge transfer
- LE: locally excited state

Membrane phases

- L_o: liquid-ordered phase
- L_d: liquid-disordered phase

Fluorophores and probes

- BODIPY: 4,4-difluoro-4-bora-3a,4a-diaza-*s*-indacene
- Laurdan: 6-dodecanoyl-2-dimethylaminonaphthalene
- Nile Red: 9-diethylamino-5H-benzo[α]phenoxazine-5-one
- Neutral Red: 3-amino-7-dimethylamino-2-methylphenazine hydrochloride
- Di-4-ANEPPDHQ: 4-(2-(6-(dioctylamino)-2-naphthalenyl)ethenyl)-1-(3-sulfopropyl)pyridinium
- DCVJ: 9-(2,2-dicyanovinyl)julolidine
- CMAM: 2-cyano-3-(4-dimethylaminophenyl)acrylic acid methyl ester
- MCCA: 7-methoxycoumarin-3-carboxylic acid

Cell lines

- A549: human lung adenocarcinoma cell line
- HepG2: human hepatocellular carcinoma cell line
- MCF-7: human breast adenocarcinoma cell line
- U-87 MG: human glioblastoma cell line

- MDA-MB-231: human triple-negative breast cancer cell line
- HMF: human mammary fibroblast cell line
- WPMY-1: human prostate myofibroblast cell line
- RPE-1: human retinal pigment epithelial cell line
- HEK 293T: human embryonic kidney cell line

Cell biology

- CAD: cationic amphiphilic drug
- LD: lipid droplet

Abstract

This thesis presents the development and application of fluorescence lifetime-based molecular probes for the quantitative characterization of physical properties in live-cell lipid structures. A series of BODIPY-based probes was designed to enable organelle-specific measurements of microviscosity in plasma membranes, lipid droplets, and lysosomes using fluorescence lifetime imaging microscopy (FLIM). The probes exhibit strong viscosity-dependent fluorescence lifetimes with minimal sensitivity to polarity, enabling reliable quantification of local membrane environments in complex biological systems.

These probes were applied to investigate how membrane microviscosity varies across cellular compartments and reflects cellular state. Significant differences were observed between cancerous and noncancerous cells, as well as in response to chemotherapeutic treatment, demonstrating that microviscosity of lipid structures serves as a sensitive indicator of cellular adaptation. Organelle-specific measurements further revealed distinct and heterogeneous changes in lipid droplet and lysosomal microviscosity.

The scope of this work was extended through the development of a polarity-sensitive BODIPY probe for lipid droplets, enabling quantitative mapping of polarity independently of lipid order. This approach revealed that lipid droplet polarity increases during early ferroptosis due to lipid peroxidation and decreases upon the emergence of ferroptosis resistance, accompanied by morphological changes in lipid droplets.

Overall, this work establishes fluorescence lifetime-based measurements of microviscosity and polarity as quantitative, spatially resolved indicators of cellular state and disease-related processes, and demonstrates their utility for probing biophysical adaptations in live cells.

Aim

The aim of this thesis was to develop fluorescence lifetime-based molecular probes for the quantitative characterization of physical properties of cellular lipid structures, and to apply these probes to investigate how variations in microviscosity and polarity reflect cellular state and disease-related processes in live cells.

Objectives

- Design and implement fluorescence lifetime-based molecular rotors and polarity probes with high sensitivity and minimal photophysical artefacts for live-cell imaging.
- Characterize the photophysical properties of the probes in solution and model lipid systems, including their sensitivity to viscosity and polarity, using steady-state and time-resolved fluorescence measurements, and establish quantitative relationships between fluorescence lifetime and environmental parameters.
- Apply the probes in artificial lipid systems and live cells to map spatial variations in microviscosity and polarity across lipid membranes and intracellular structures.
- Demonstrate the biological relevance of these measurements by investigating how variations in microviscosity and polarity reflect cellular state, disease-related processes, and responses to chemical perturbations.

Actuality

The dynamic physical properties of cellular lipid structures, such as microviscosity and polarity, play an important role in membrane organization, lipid metabolism, and cellular adaptation. However, their quantitative characterization in live cells remains challenging due to the lack of suitable probes that combine sensitivity, specificity, interpretability, and compatibility with fluorescence lifetime imaging.

This work addresses these limitations through the development and application of fluorescence lifetime-based molecular rotors and polarity probes tailored for live-cell measurements. Particular emphasis was placed on minimizing common photophysical artefacts, such as polarity–viscosity cross-sensitivity, and on achieving reliable readouts in heterogeneous lipid environments.

While the development of organelle-targeting probes itself is not new, this thesis provides several advances in probe design and application. A fluorescence lifetime-based polarity probe with emission in the deep-red spectral region was developed, enabling quantitative measurements of lipid droplet polarity with minimal interference from viscosity. In addition, it was demonstrated that lipid droplet targeting is not governed solely by hydrophobicity, but is also influenced by molecular geometry, with non-planar, non-polar structures preferentially partitioning into isotropic lipid environments.

The probes developed in this work were applied to investigate biologically relevant processes in live cells. These include changes in lipid droplet microviscosity under chemotherapeutic treatment, alterations in lysosomal membrane viscosity in response to cationic amphiphilic drugs, and polarity changes associated with lipid peroxidation during ferroptosis and the emergence of resistance.

Overall, this work demonstrates that fluorescence lifetime-based measurements of microviscosity and polarity provide quantitative, spatially resolved insight into cellular state and disease-related processes. By linking probe design, photophysical characterization, and biological application, this thesis establishes an approach for using physical parameters of lipid systems as functional readouts of cellular behaviour.

Defending Statements

- Local microviscosity changes in biological compartments reflect physiological and pathological states, enabling the detection of disease-related alterations and drug-induced effects.
- Non-planar molecular geometries favor incorporation of fluorescent probes into isotropic lipid systems.
- Fluorescence-based polarity imaging provides a quantitative readout of lipid peroxidation in lipid environments.

Chapter 1

Introduction

The classical view of cellular lipids as passive structural components or simple energy reservoirs has evolved into a more dynamic understanding of lipid heterogeneity within biological systems. In living cells, lipids are neither uniformly distributed nor randomly organized. Instead, they are partitioned into specialized compartments, ranging from the phospholipid bilayers of cellular organelles, such as mitochondria and lysosomes, to the neutral lipid cores of lipid droplets (LDs).

This spatial diversity extends beyond the level of organelles to the nanoscale organization of biological membranes. Within a single membrane, lipids can segregate into microdomains enriched in specific lipid species, including cholesterol and sphingolipids. Such lateral heterogeneity is not merely a structural consequence of lipid composition but represents an essential feature of cellular organization. Differences in lipid composition between cell types, as well as between individual organelles within the same cell, create distinct physical environments that regulate numerous biological processes.

To understand how lipid structures influence cellular function, it is necessary to consider their local physical properties, particularly microviscosity and polarity. Microviscosity, closely related to lipid packing and membrane order, reflects the resistance of a lipid environment to molecular motion. This parameter plays an important role in regulating the diffusion of membrane proteins, lipids, and signaling molecules. Regions of increased viscosity are often associated with more ordered lipid packing, which can influence the spatial organization of proteins and modulate signaling pathways. Polarity, on the other hand, describes the local dielectric environment within lipid systems and can affect

the localization of peripheral proteins, as well as the orientation and behavior of transmembrane domains.

Together, these physical properties contribute to the functional regulation of cellular processes, ranging from metabolic activity in mitochondria to lipid storage and mobilization in LDs. Alterations in lipid microenvironment properties may occur under conditions such as oxidative stress, metabolic disorders, or disease progression, leading to changes in membrane organization and cellular signaling.

Despite their importance, the experimental characterization of local lipid microenvironments remains challenging. Many classical biophysical techniques provide only bulk-averaged information about membrane properties. Methods such as nuclear magnetic resonance (NMR) and electron paramagnetic resonance (EPR) spectroscopy have been widely used to study lipid organization and dynamics. However, they often lack the spatial resolution required to distinguish between different cellular compartments in living cells. As a result, approaches capable of probing physical properties directly within specific cellular environments are required.

This need has driven the development of environment-sensitive fluorescent probes. Unlike conventional fluorescent labels, these molecules can respond to changes in their local surroundings and therefore act as nanoscale sensors. Among such probes, molecular rotors represent an important class of fluorophores whose fluorescence quantum yield and lifetime depend on intramolecular rotation processes. In environments of higher viscosity, rotational relaxation is restricted, leading to an increase in fluorescence intensity and lifetime. Another important class includes solvatochromic dyes, which exhibit shifts in their emission spectra or fluorescence lifetime depending on the polarity of the surrounding medium.

Among the various fluorophore scaffolds available for the design of such probes, BODIPY dyes have emerged as particularly attractive candidates. Their favorable photophysical properties, including high fluorescence quantum yields, narrow emission bands, and excellent photostability, combined with versatile synthetic modification possibilities, enable the development of probes tailored for specific biological applications. In particular, BODIPY-based probes can be engineered to sense local viscosity and polarity and can be applied in advanced imaging techniques such as fluorescence lifetime imaging microscopy (FLIM), providing detailed insight into the physicochemical properties of lipid microenvironments in living cells.

1.1 Lipid Microenvironments and Physical Properties of Cellular Membranes

Cellular membranes are laterally heterogeneous assemblies composed of lipids with varying degrees of saturation and acyl chain length, together with differing amounts of cholesterol.[1–3] These compositional variations give rise to distinct lipid phases, commonly described by two limiting states: the liquid-ordered (L_o) and liquid-disordered (L_d) phases (Fig. 1.1).[4] L_o phases are typically enriched in saturated lipids and cholesterol, resulting in tightly packed, highly crowded environments.[5] In contrast, L_d phases are enriched in unsaturated lipids and contain lower amounts of cholesterol, resulting in reduced lipid packing and a more disordered environment.[5] Here, molecular crowding refers to the local packing density of lipid molecules within the bilayer.

While lipid composition is a major determinant of membrane organization, biological membranes also contain substantial amounts of membrane-associated and integral proteins.[6] These proteins contribute to local molecular crowding and can influence lipid packing, diffusion, and hydration at the membrane interface.[6] Consequently, the physical properties sensed by environment-sensitive probes reflect the combined effects of lipid composition and protein content.

In addition to lipid packing, membrane environments differ in their degree of interfacial hydration, defined as the extent of water penetration and dynamics at the lipid–water interface (Fig. 1.1).[7] Tightly packed L_o-like regions generally exhibit reduced water penetration into the hydrophobic core, whereas more disordered L_d-like regions allow greater solvent accessibility and dynamic hydration.[8;9]

In biological membranes, however, these phase extremes are rarely observed as large, stable domains. Instead, cellular membranes are characterized by highly dynamic and nanoscale heterogeneity, where ordered and disordered regions are small, transient, and often below the diffraction limit.[10;11] Accordingly, membrane organization is more accurately described as a continuum of lipid environments with gradually varying physical properties, rather than a system composed of well-separated, phase-segregated domains.[10]

Within this framework, molecular crowding (lipid packing density) and interfacial hydration emerge as two fundamental and complementary physical descriptors of local membrane organization. Ordered, tightly packed environments are generally associated with higher mi-

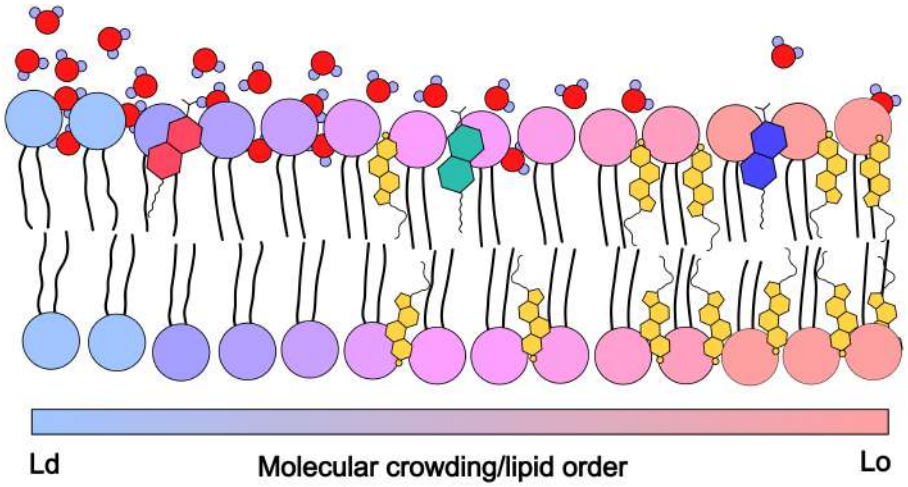

Figure 1.1: Schematic of lipid bilayer heterogeneity depicted as a continuum from L_d-like to L_o-like environments, highlighting increasing lipid packing density (molecular crowding), decreasing solvent accessibility at the interface, and the corresponding solvatochromic response of an environment-sensitive fluorophore.

croviscosity[12] and reduced local polarity,[13] particularly within the hydrophobic core and interfacial regions probed by environment-sensitive fluorophores. In contrast, disordered regions typically exhibit lower microviscosity and increased polarity.[12;13] Thus, molecular crowding primarily reflects local mechanical constraints on molecular motion, whereas interfacial hydration reports on solvent accessibility and dielectric properties.

These parameters provide experimentally accessible readouts of membrane organization, reflecting local molecular crowding and hydration in complex and heterogeneous systems. Importantly, they form the basis for the use of environment-sensitive fluorescent probes, which translate local variations in molecular crowding and hydration into measurable changes in fluorescence lifetime or spectral properties.

The physical state of lipid membranes plays a central role in regulating a wide range of cellular functions and processes. Membrane organization governs the lateral diffusion of lipids and proteins,[14] the localization of membrane-associated proteins,[15;16] and the formation of signaling platforms.[17;18] In addition, membrane physical properties are involved in processes such as membrane trafficking[19] and interactions

with external agents, including pathogens[20] and pharmaceutical compounds.[21] In the following sections, these two dimensions, molecular crowding and interfacial hydration, are addressed using viscosity- and polarity-sensitive fluorescent probes, respectively.

1.2 Fluorescent Probes as Reporters of Membrane Microenvironments

The physical parameters introduced above, molecular crowding and interfacial hydration, are not directly accessible by conventional microscopy. Their characterization therefore relies on indirect approaches capable of translating local physical properties into measurable signals. Among these, fluorescence-based methods are particularly well suited due to their compatibility with live-cell imaging, high spatial and temporal resolution, and minimal invasiveness.[22]

Environment-sensitive fluorescent probes operate as nanoscale reporters, converting variations in local molecular organization into changes in observable photophysical properties.[23;24] In principle, this provides a powerful route to access membrane properties that remain otherwise inaccessible in living systems.[23]

However, a notable disparity exists between probe development and their practical use in biological research. A large number of environment-sensitive fluorophores have been reported, often with increasingly sophisticated photophysical designs, yet their adoption in routine biological studies remains limited. In many cases, biological imaging still relies predominantly on intensity-based measurements, where relatively small changes in fluorescence are interpreted without fully accounting for probe concentration, optical artefacts, or environmental cross-sensitivities.[25–27]

This gap reflects a fundamental challenge: fluorescence signals do not report physical parameters directly, but instead arise from probe-specific excited-state processes that may depend on multiple environmental variables simultaneously.[25] As a result, extracting quantitative or even unambiguous information requires careful consideration of probe behaviour, which is often at odds with the need for simple experimental tools in biological applications.[25]

Consequently, the development of environment-sensitive probes is not only a question of increasing sensitivity, but also of improving

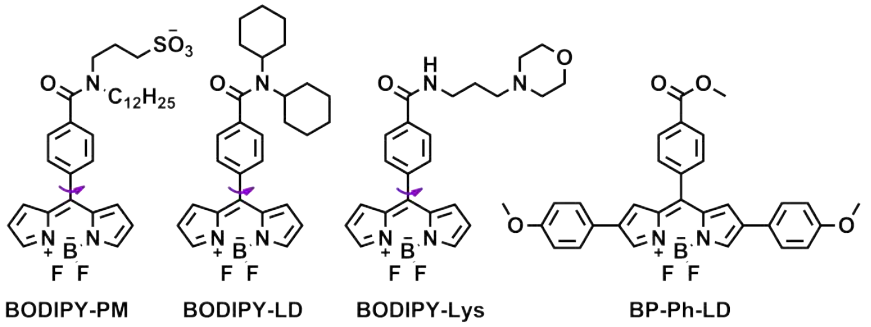

Figure 1.2: Structures of BODIPY probes used in this work.

selectivity and interpretability under complex biological conditions. Probes that minimize cross-sensitivity,[28–30] localize reliably within specific cellular compartments,[31] and provide concentration-independent readouts[32] are more likely to be adopted beyond specialized studies. In this context, two major classes of probes are employed throughout this work: viscosity-sensitive molecular rotors, which report molecular crowding through fluorescence lifetime changes,[32] and polarity-sensitive fluorophores, which report local hydration and environmental polarity.[31]

In this work, BODIPY-based fluorophores are employed as a unified platform to address these challenges (Fig. 1.2). By systematic modification of the molecular structure, these probes can be tuned to selectively report on molecular crowding or interfacial hydration, enabling a more controlled investigation of lipid microenvironments using well-defined photophysical responses.[33–35]

In the following sections, viscosity-sensitive molecular rotors and polarity-sensitive fluorophores are discussed in detail. Molecular rotors are first introduced as reporters of microviscosity, followed by polarity-sensitive probes for mapping interfacial hydration.

1.3 Molecular Rotors

Fluorophores that exhibit viscosity-dependent quantum yields, now broadly termed molecular rotors, trace their origins to the 1980 work of Law, who observed this phenomenon in donor-acceptor malononitrile derivatives, such as *9-(2,2-dicyanovinyl)julolidine DCVJ* (Fig. 1.5A).[36] This

observation revealed that certain fluorescent molecules can respond to the local mechanical properties of their environment by modulating their excited-state dynamics.[36]

This behaviour arises from the competition between radiative and non-radiative decay pathways that are coupled to intramolecular rotation.[37] In low-viscosity solvents, intramolecular rotation can occur freely in the excited state, providing an efficient pathway for non-radiative relaxation via the dissipation of energy into the solvent's vibrational and translational degrees of freedom.[35] As a result, fluorescence is strongly quenched. In contrast, increased solvent viscosity restricts this torsional motion, suppressing non-radiative decay and leading to enhanced fluorescence quantum yields and emission intensities.[35]

It is important to distinguish this specific mechanism from the general viscosity dependence observed in many conventional fluorophores. While many dyes exhibit a modest increase in quantum yield in viscous media, often due to the suppression of collisional quenching or minor vibrational modes,[38] molecular rotors possess a dedicated, large-amplitude internal rotational degree of freedom that is strongly coupled to excited-state relaxation.[33] Consequently, their sensitivity to the environment is typically orders of magnitude greater than that of conventional fluorophores, which lack a dedicated intramolecular rotational deactivation pathway.

Furthermore, this dependence does not arise from macroscopic viscosity itself, but from the extent to which the local environment restricts this specific motion.[39] In this context, molecular rotors probe an effective microviscosity, a parameter more accurately described in terms of solvent free volume,[40] *i.e.*, the local voids between molecules that provide the space necessary for intramolecular rotation.[41;42] Because this sensing mechanism relies on internal rotational motion, this class of probes became known as molecular rotors.

Macroscopic viscosity refers to the bulk dynamic viscosity measured using conventional rheological methods. In contrast, microviscosity describes the local resistance to molecular motion on nanometer length scales. Molecular rotors do not directly measure bulk viscosity, rather, their response reflects an effective microviscosity determined by the local free volume and steric constraints governing intramolecular rotation.[39;40] Consequently, identical bulk viscosities may yield different rotor responses if the local molecular environments differ.[39]

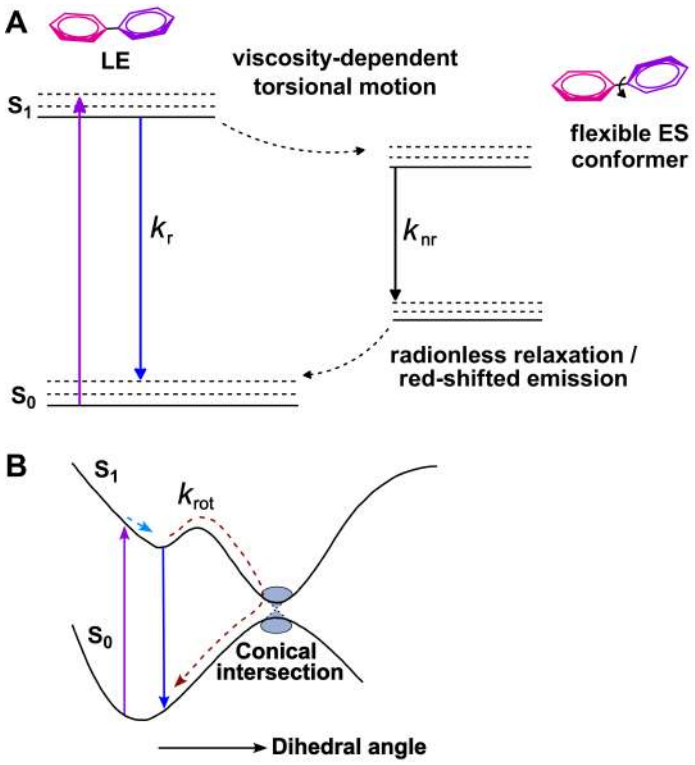

Figure 1.3: (A) Jablonski diagram illustrating the generic working principle of molecular rotors. After excitation to the locally excited (LE) state, the molecule can either undergo radiative relaxation or access a twisted excited state through intramolecular rotation. The competition between these pathways is governed by the viscosity-limited rate of rotation (k_{rot}). (B) Schematic potential energy surface along the torsional reaction coordinate, represented by the dihedral angle between rotating subunits. The diagram illustrates the activation barrier for rotation in the excited state and access to a twisted configuration associated with a conical intersection that facilitates non-radiative decay.

Following excitation to the S_1 state, molecular rotors can relax through two competing pathways (Fig. 1.3A). If intramolecular torsional motion is not restricted, thermal activation enables the molecule to overcome an intrinsic rotational energy barrier.[43] The rate of this process, k_{rot}, follows an Arrhenius-type dependence characteristic of thermally activated barrier crossing and is strongly modulated by the local environment (Fig. 1.3B).[28] In low-viscosity media, k_{rot} is high, enabling efficient population of a twisted excited state, often associated with a minimum-energy conical intersection that facilitates rapid non-radiative decay.[44]

In contrast, in highly viscous or crowded environments, intramolecular rotation is hindered, leading to a reduction in k_{rot} and suppression of non-radiative relaxation. As a result, the molecule remains in the locally excited (LE) state, giving rise to enhanced fluorescence emission.[44] While early descriptions attributed this behaviour primarily to twisted intramolecular charge transfer (TICT) states,[43] it is now recognized that a broader range of twisting-mediated non-radiative pathways, including access to dark states or conical intersections, may be involved depending on molecular structure.[45;46]

The dependence of fluorescence observables on solvent dynamic viscosity (η) for molecular rotors is commonly described by the Förster–Hoffmann relationship (Eq. 1.1):[47]

$$\Phi = A\eta^x \tag{1.1}$$

Here Φ is the fluorescence quantum yield, while A and x are empirical constants characteristic of a given probe. This phenomenological relationship reflects the viscosity-controlled balance between radiative and non-radiative decay pathways and enables calibration of fluorescence response in solvent mixtures of known viscosity. However, deviations from ideal power-law behaviour are commonly observed in highly viscous, heterogeneous, or biologically complex environments.[48]

An analogous relationship can be formulated for fluorescence lifetime τ (Eq. 1.2):

$$\tau = B\eta^x \tag{1.2}$$

Here τ is the fluorescence lifetime, η is the solvent viscosity, and B and x are probe-dependent empirical constants. Because both fluorescence quantum yield and lifetime depend on the relative contributions of radiative and non-radiative decay rates, suppression of non-radiative relaxation in viscous environments leads to an increase in both the fluorescence quantum yield (Φ) and the fluorescence lifetime (τ). In practice, fluorescence lifetime is generally preferred for quantitative measurements, as it is largely independent of probe concentration, excitation intensity, and optical path length. This makes it particularly well suited for microscopy experiments in heterogeneous systems.

An often overlooked but critical requirement for reliable lifetime-based measurements is the simplicity of the underlying excited-state

kinetics. In systems where multiple emissive states are populated, fluorescence decay becomes inherently multiexponential. This introduces significant challenges for quantitative analysis, as accurate lifetime extraction requires substantially higher photon counts, and the fitted parameters become strongly correlated. In such cases, variations in one component can be compensated by changes in another, reducing the certainty and interpretability of the extracted lifetimes.

In contrast, molecular rotor designs that couple intramolecular rotation to non-radiative decay via dark states or conical intersections provide an intrinsic advantage (Fig. 1.3B). By rendering the rotated state effectively non-emissive, these systems reduce the photophysics to an effectively single observable emissive state under ideal conditions.[49;50] As a result, fluorescence decay approaches monoexponential behaviour, greatly improving the reliability and precision of lifetime measurements. Importantly, this advantage becomes even more pronounced in heterogeneous biological environments, where additional sources of complexity are often unavoidable. Starting from a system that already exhibits multiexponential decay in homogeneous solution would only exacerbate these limitations in live-cell imaging.

This design principle is particularly relevant for BODIPY-based molecular rotors, where access to non-radiative decay pathways through dark states or conical intersections enables accurate lifetime readouts.[51] While such considerations are less critical for ratiometric probes, they are central to the performance of fluorescence lifetime-based sensors.

Nevertheless, fluorescence lifetime remains sensitive to additional environmental factors, including quenching by molecular oxygen (O_2), heavy atoms, and significant changes in solvent polarity or hydrogen-bonding capacity, and therefore requires careful interpretation in complex biological environments.[52;53]

Because the rotational rate k_{rot} is thermally activated, both fluorescence quantum yield and lifetime depend not only on viscosity but also on temperature.[54] In practice, calibration and imaging experiments are often performed under different thermal conditions, particularly when comparing model systems at room temperature with live-cell measurements at physiological temperature. Consequently, the temperature dependence of a given molecular rotor should be evaluated to ensure reliable interpretation.

The extent of this temperature sensitivity is governed by the activation energy (E_a) associated with intramolecular rotation (Fig. 1.3B).

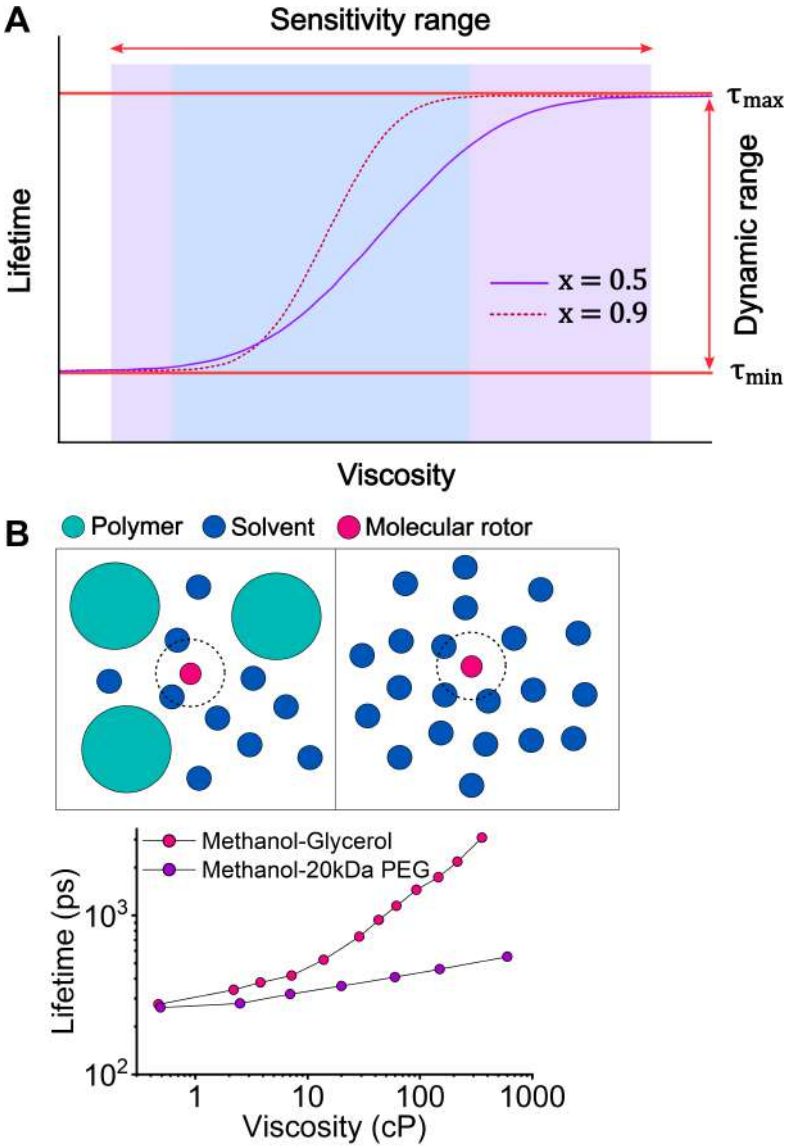

Figure 1.4: (A) Fluorescence lifetime as a function of viscosity when the Förster–Hoffmann constant is varied. If x is increased, the viscosity sensitivity becomes greater but the sensitivity range is reduced.[55] (B) The effect of solvent free volume on the rotor's readout: the signal is independent of bulk viscosity caused by large, sparse structures, and instead reflects the local density and crowding of the environment.[39] Adapted with permission from refs.[39;55]

When $E_a \gg k_{\mathrm{B}}T$, the rotational process is strongly thermally activated, and the probe exhibits marked temperature dependence.[33] In contrast, when $E_a \sim k_{\mathrm{B}}T$, the barrier can be readily overcome, and temperature effects are comparatively weak over biologically relevant ranges. Consequently, both viscosity and temperature contributions to k_{rot} should be considered when interpreting fluorescence-based measurements of microviscosity.

A central parameter in the Förster–Hoffmann relationship (Eqs. 1.1 and 1.2) is the empirical exponent x, which governs how strongly the photophysical response is coupled to viscosity and defines the accessible dynamic range of the probe (Fig. 1.4A). Higher x values correspond to increased sensitivity, providing larger changes in fluorescence lifetime for a given change in viscosity, but at the expense of a reduced dynamic range.[55]

In high-sensitivity systems, the non-radiative decay pathway becomes strongly coupled to intramolecular rotational motion (contributing to the non-radiative decay rate k_{nr}), such that the fluorescence lifetime approaches its theoretical maximum ($\tau_{\max} = 1/k_r$) at moderate viscosities. Once this saturation regime is reached, the τ–η relationship flattens, and the differential sensitivity ($d\tau/d\eta$) approaches zero. In this regime, small experimental uncertainties in lifetime measurements can propagate into large errors in the inferred microviscosity.

Conversely, lower x values provide a broader dynamic range, allowing viscosity changes to be resolved over a wider interval.[55] For lipid environments, where microviscosities typically span tens to hundreds of centipoise and may extend toward $\sim 10^3$ cP, intermediate x values are generally more suitable.

Physically, the exponent x reflects the extent to which non-radiative decay is coupled to intramolecular rotation, and thus depends on molecular structure and the topology of the excited-state potential energy surface.

From an imaging perspective, the choice of x represents an optimization problem rather than a purely sensitivity-driven parameter. In FLIM, where photon statistics limit lifetime precision, an optimal probe maximizes sensitivity within the relevant viscosity range while avoiding operation in the saturation regime. Accordingly, molecular rotors with moderate $x \sim 0.4$–0.6 are generally best suited for quantitative measurements in heterogeneous biological environments.

The distinction between microviscosity and macroscopic viscosity

has significant implications for experimental design (Fig. 1.4B). For instance, solutions that are macroscopically viscous due to the presence of dilute macromolecules, such as polymers or biomolecules, may not produce high viscosity readouts from molecular rotors.[39] In such systems, the local solvent environment around the probe may still possess sufficient free volume to allow intramolecular rotation. In contrast, highly crowded or concentrated macromolecular environments, where solvent free volume is strongly restricted on the nanometer scale, result in increased rotor responses.[39] This makes molecular rotors particularly well suited for studying molecular crowding in cellular interiors, where bulk viscosity and microviscosity often diverge.

A common architectural motif in first-generation molecular rotors is the push-pull framework, where electron-donating and withdrawing groups are coupled via a conjugated bridge. In such donor–acceptor systems, exemplified by *DCVJ*, excitation leads to intramolecular charge transfer (ICT), often followed by the formation of a TICT state (Fig. 1.5A).[30] While this design provides strong sensitivity to environmental constraints, it also introduces an inherent limitation.

The formation of a TICT state involves substantial charge separation, resulting in a large excited-state dipole moment. Consequently, the emission properties become strongly dependent not only on viscosity but also on solvent polarity.[48] In polar environments, stabilization of the TICT state leads to additional solvatochromic shifts and changes in emission intensity.[56] This dual sensitivity complicates the interpretation of fluorescence signals, particularly in biological compartments, where the dielectric constant (ε) can vary significantly. Under such conditions, fluorescence responses may reflect a convolution of viscosity and polarity effects rather than a well-defined mechanical property.[57]

To address these limitations, alternative molecular rotor designs have been developed that minimize changes in dipole moment upon excitation. These include non-polar probes in which intramolecular twisting leads to population of non-emissive dark states or conical intersections without significant TICT character, as well as systems in which multiple emissive states participate in the relaxation process.[58;59] By reducing solvatochromic contributions, these probes provide a more selective response to microviscosity and improve measurement reliability in heterogeneous environments.

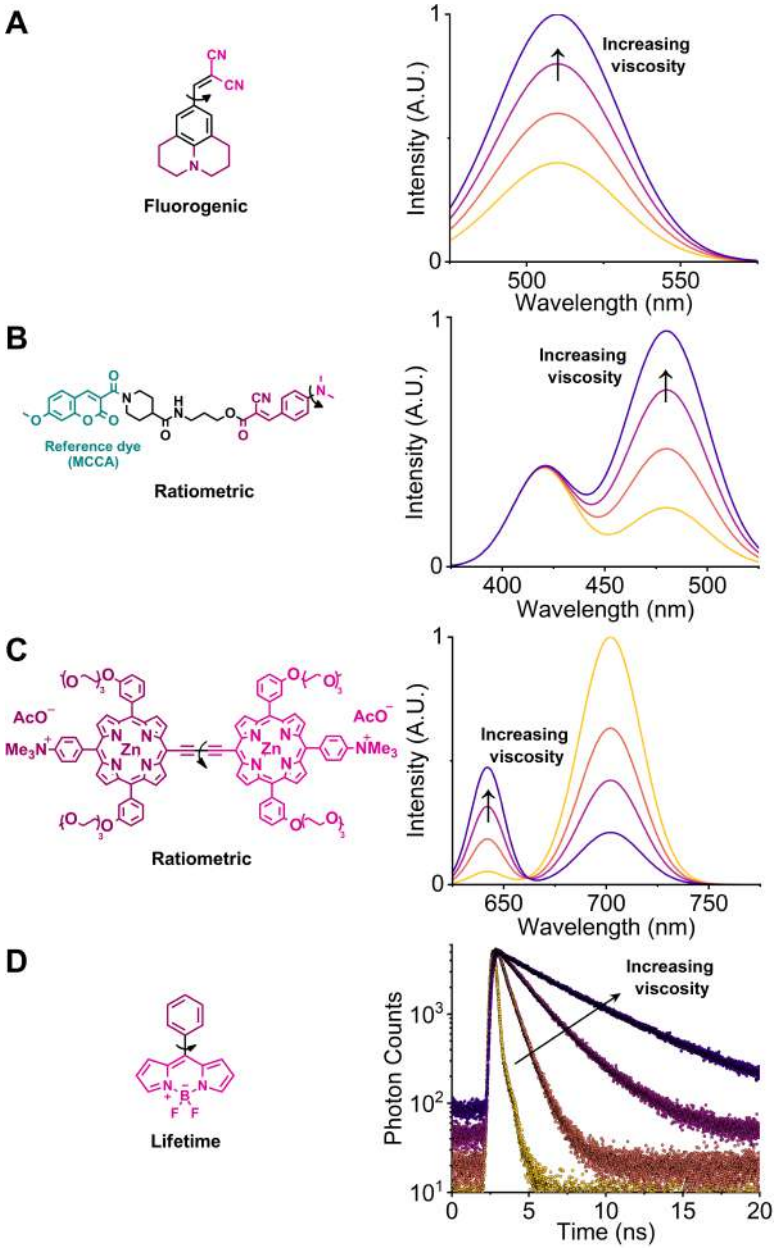

Figure 1.5: Examples of molecular rotor designs employing different readout strategies. (A) Donor–acceptor molecular rotor undergoing TICT state formation.[36] (B) Spectral ratiometric rotor in which a viscosity-sensitive fluorophore is linked to a viscosity-insensitive reference dye.[60] (C) Conformer-based ratiometric rotor where two emissive conformers exhibit viscosity-dependent emission.[61] (D) Fluorescence lifetime-based molecular rotor.[62] Adapted with permission from refs.[32;36;60–62]

Historically, viscosity measurements using molecular rotors relied primarily on fluorescence intensity or quantum yield (Fig. 1.5A).[36] While such approaches are well suited for homogeneous solutions and *in vitro* studies,[63–65] their application in live-cell imaging is inherently limited. Fluorescence intensity depends directly on probe concentration, which is typically unknown and spatially heterogeneous in cellular environments due to variable partitioning and probe redistribution. As a result, intensity-based measurements generally do not allow for quantitative comparison between samples. In addition, intensity readouts are influenced by optical artefacts such as light scattering, absorption, and photobleaching, further complicating data interpretation.

One strategy to mitigate these limitations is the use of spectral ratiometric molecular rotors (Fig. 1.5B,C), in which the viscosity-sensitive emission is referenced to a second signal.[60;61] This enables the response to be expressed as an intensity ratio that is largely independent of probe concentration.

An early implementation of this concept involved a paired fluorescent molecular rotor composed of a viscosity-sensitive *2-cyano-3-(4-dimethylaminophenyl)acrylic acid methyl ester (CMAM)* unit covalently linked to a reference *7-methoxycoumarin-3-carboxylic acid (MCCA)* fluorophore (Fig. 1.5B).[60;66] Alternatively, ratiometric behaviour can arise from viscosity-dependent conformational equilibria within a single molecule. For example, conjugated porphyrin dimers exhibit planar and twisted conformers with distinct emission spectra, where the relative population of each state is governed by environmental viscosity (Fig. 1.5C).[61;67;68]

An alternative approach that avoids concentration- and scattering-related artefacts is FLIM using molecular rotors (Fig. 1.5D).[62] In this case, viscosity is inferred from the fluorescence decay kinetics of the probe,[69–71] providing a readout that is inherently independent of probe concentration and excitation intensity.

Both ratiometric and lifetime-based approaches offer concentration-independent measurements under typical conditions, but they differ in practical implementation. Ratiometric imaging can be performed on standard fluorescence microscopes and does not require specialized instrumentation. However, it remains sensitive to wavelength-dependent optical effects such as scattering and variations in detection efficiency. In contrast, fluorescence lifetime measurements are largely insensitive to such effects, but require pulsed excitation sources and time-resolved detection, and are typically associated with longer acquisition times due to the need for photon counting and decay reconstruction.

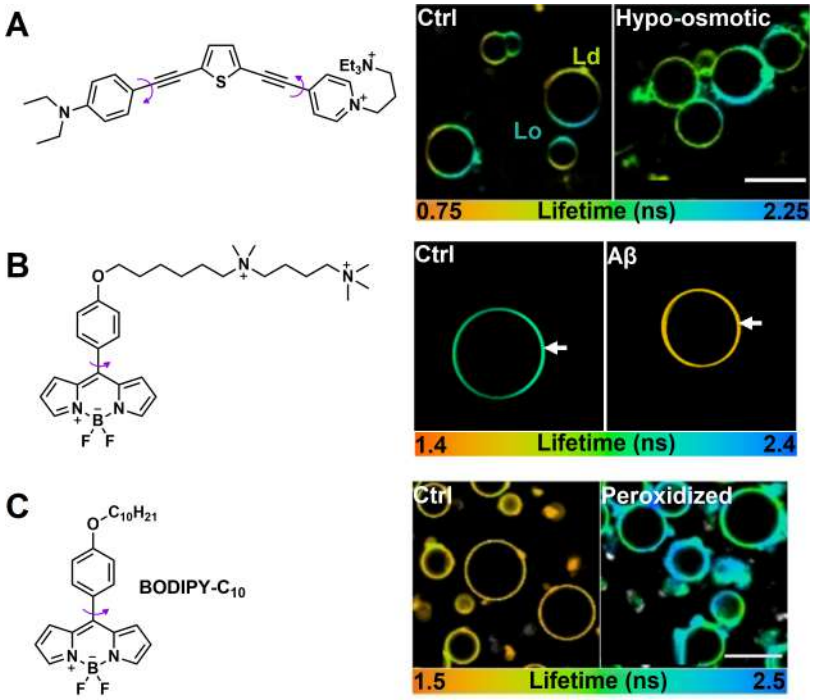

Figure 1.6: Representative applications of molecular rotors for probing membrane microviscosity in model lipid systems. (A) FLIM of a thiophene-based molecular rotor in phase-separated GUVs under native and hypo-osmotic conditions, demonstrating tension-induced changes in membrane microviscosity and reduced contrast between L_o and L_d domains.[72] (B) FLIM of a BODIPY-based molecular rotor in GPMVs, showing a decrease in membrane microviscosity upon interaction with Aβ(1–42) oligomers.[73] (C) FLIM of BODIPY-C_{10} in GUVs composed of native POPC and peroxidized POPC-OOH lipids, revealing the emergence of coexisting membrane domains upon lipid peroxidation.[74] Adapted with permission from refs.[72–74]

Together, these approaches represent complementary strategies for quantitative microviscosity measurements, with the choice depending on the experimental constraints and the required level of accuracy.

Having established the photophysical principles underlying molecular rotors, it is important to consider how these properties can be exploited in practical applications. In particular, the sensitivity of fluorescence quantum yield and lifetime to microviscosity enables molecular rotors to serve as powerful probes of local mechanical properties in complex and heterogeneous lipid environments. Accordingly, molecular

rotors have been widely applied to investigate microviscosity in model lipid systems, live cells, and complex biological environments.[72–74]

Several representative applications of molecular rotors for probing membrane microviscosity in lipid systems are shown in Figure 1.6. In phase-separated GUVs (Fig. 1.6A), molecular rotors readily distinguish between L_o and L_d lipid phases based on their distinct microviscosities, enabling visualization of lateral membrane organization.[72] Moreover, changes in membrane tension, such as those induced by hypo-osmotic conditions, can be directly monitored through shifts in fluorescence lifetime, reflecting alterations in lipid packing and mechanical properties.[72]

Molecular rotors are also well suited for studying membrane–protein interactions. The presence of amyloid-β oligomers leads to a decrease in membrane microviscosity in giant plasma membrane vesicles (GPMVs), demonstrating the membrane-modulating effects of these aggregates (Fig. 1.6B).[73] Such measurements provide a quantitative and spatially resolved means of assessing how biomolecules perturb membrane structure.

Molecular rotors can also be used to investigate chemically induced changes in membrane organization. Lipid peroxidation of POPC results in the emergence of coexisting membrane domains, despite the nominally single-component composition (Fig. 1.6C).[74] This behaviour can be attributed to different configurations of oxidized lipids within the bilayer, which give rise to distinct microviscosities.[74]

Figure 1.7 highlights the application of molecular rotors for probing microviscosity in live-cell environments. Targeted strategies, including the use of HaloTag-conjugated molecular rotors (Fig. 1.7A), enable selective localization of probes to specific organelles, allowing direct comparison of microviscosity and molecular crowding within different cellular compartments.[75] Using this strategy, hypertonic stress was shown to significantly increase the microviscosity of endoplasmic reticulum membranes.

Molecular rotors also provide a means to quantify membrane perturbations induced by pharmacological agents. As shown in Fig. 1.7B, treatment of HeLa cells with cisplatin results in increased plasma membrane microviscosity, reflecting changes in lipid organization and membrane properties.[76]

In addition to lifetime-based approaches, ratiometric molecular rotors can be used to monitor intracellular viscosity changes. For example,

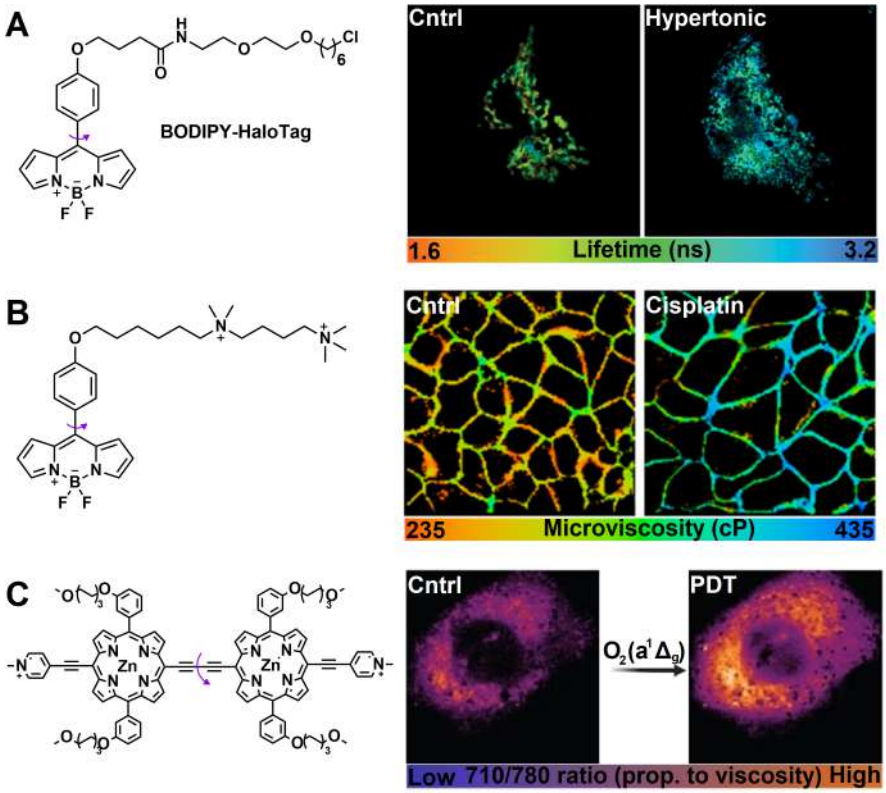

Figure 1.7: Representative applications of molecular rotors for probing membrane microviscosity in live cells. (A) FLIM of a BODIPY-HaloTag molecular rotor targeted to the endoplasmic reticulum of COS-7 cells, showing an increase in microviscosity under hypertonic conditions.[75] (B) FLIM of a BODIPY-based molecular rotor in the plasma membrane of HeLa cells, demonstrating increased microviscosity upon cisplatin treatment.[76] (C) Spectral ratiometric imaging of intracellular microviscosity using a porphyrin-dimer-based rotor in Chinese hamster ovary cells during photodynamic therapy, revealing an increase in viscosity during treatment.[67] Adapted with permission from refs.[67;75;76]

porphyrin-dimer-based rotors (Fig. 1.7C) reveal a substantial increase in intracellular microviscosity during photodynamic therapy, demonstrating the sensitivity of these probes to dynamic changes in cellular state.[67]

Together, these examples highlight the versatility of molecular rotors as probes of membrane microviscosity, capable of reporting on phase behaviour, mechanical perturbations, and biochemical modific-

ations with high spatial resolution in living and model systems. The choice between intensity-based, ratiometric, or lifetime-based probes involves a trade-off between hardware requirements and the need for concentration-independent quantification. Nevertheless, time-resolved approaches provide a reliable and widely adopted route to quantitative viscosity determination, provided that the underlying photophysics, including temperature effects and potential non-viscosity-related quenching pathways, are carefully controlled and accounted for.

1.4 Polarity-Sensitive Probes

Fluorescent polarity probes are widely used to investigate the local physical properties of complex environments such as biological membranes,[31] protein binding sites,[77] as well as intracellular and subcellular compartments.[78] In contrast to bulk dielectric measurements, these probes report the effective polarity experienced by the fluorophore on a molecular scale, which reflects both the dielectric properties of the medium and its dynamic response to excitation.[79]

Polarity is a complex and multifaceted physical property that cannot be fully described by a single parameter. In the context of fluorescent probes, it is more precisely understood as the effective solvation environment experienced by the fluorophore.[79] While bulk solvent polarity is often approximated using macroscopic quantities such as the dielectric constant and refractive index, the local polarity experienced by a fluorophore additionally depends on a combination of nonspecific and specific interactions, including dispersion forces, electrostatic interactions, and hydrogen bonding, as well as the dynamic reorganization of the surrounding environment.[78] As a result, polarity-sensitive probes report a composite response that integrates these contributions at the molecular scale.

A widely used framework for describing the influence of solvent polarity on spectral properties is provided by the Lippert–Mataga orientational polarizability parameter Δf (Eq. 1.3),[80] which depends on the dielectric constant (ε) and refractive index (n) of the solvent:

$$\Delta f = \frac{\varepsilon - 1}{2\varepsilon + 1} - \frac{n^2 - 1}{2n^2 + 1} \tag{1.3}$$

Physically, Δf reflects the relative contributions of the high-frequency

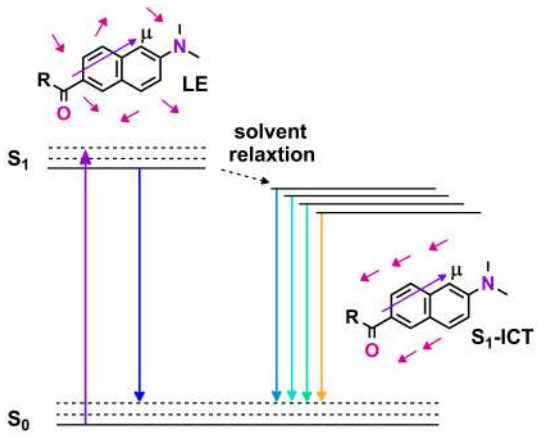

Figure 1.8: Jablonski diagram illustrating the generic working principle of polarity-sensitive probes. Following excitation to the locally excited (LE) state, solvent relaxation in polar environments stabilizes an intramolecular charge transfer (ICT) state, resulting in a lower excited-state energy and red-shifted fluorescence emission.

(electronic) and low-frequency (orientational) responses of the solvent. The refractive index term accounts for the instantaneous electronic polarization, whereas the dielectric constant captures the slower reorientation of permanent dipoles. The subtraction of these terms isolates the orientational contribution to solvation by removing the instantaneous electronic response from the total dielectric polarization. Following excitation to the Franck–Condon state, the solvent initially responds via rapid electronic polarization, which occurs on a sub-picosecond timescale.[81;82] This is followed by slower nuclear reorganization, involving the reorientation of solvent dipoles around the excited-state charge distribution.[81;82] This relaxation process stabilizes the excited state and gives rise to the Stokes shift. The extent to which this stabilization is reflected in the emission depends on the relative timescales of solvent relaxation (τ_s) and fluorescence (τ_f). If solvent relaxation is fast ($\tau_s \ll \tau_f$), emission occurs from a fully relaxed excited state. In contrast, in rigid or viscous environments where τ_s becomes comparable to or exceeds τ_f, emission may occur from a partially relaxed state.

Orientation polarizability parameter Δf is commonly used to relate the Stokes shift ($\Delta\nu$) to solvent polarity, often yielding an approximately linear dependence for fluorophores undergoing ICT.[83;84] However, the Lippert–Mataga model primarily accounts for nonspecific continuum electrostatic interactions. It does not capture specific solute–solvent

interactions such as hydrogen bonding or second-order effects, such as dipoles induced in the solvent molecules by the fluorophore. Consequently, deviations from linearity are frequently observed, particularly in complex or structured environments.[85–87] To address some of these limitations, alternative empirical polarity scales incorporating specific solvent effects, such as the $E_T(30)$ scale, have been developed.[88] The $E_T(30)$ scale is based on the solvatochromic response of a pyridinium *N*-phenolate betaine dye and reflects the transition energy of the dye in a given solvent.[89] As a result, it incorporates both nonspecific dielectric effects and specific interactions, including hydrogen bonding.[88;89] Nevertheless, no single-parameter polarity scale is sufficient to universally describe solvent effects on fluorophore photophysics, as the dominant interactions governing spectral behaviour vary between different molecular systems.

The sensitivity of most polarity probes is closely linked to these ICT processes occurring in the excited state (Fig. 1.8). Following excitation, the fluorophore is initially promoted to a LE state. Subsequent solvent relaxation and intramolecular charge redistribution can lead to the formation of an ICT state characterized by increased charge separation and a larger dipole moment. Stabilization of this state in polar environments gives rise to characteristic changes in fluorescence emission, forming the physical basis for most polarity-sensitive readouts.

Depending on the molecular architecture, these ICT-driven systems can manifest in different experimentally accessible observables, including fluorescence intensity, emission spectra, and fluorescence lifetime (Fig. 1.9). Although these readouts are often treated separately, they originate from the same underlying process: the environment-dependent modulation of excited-state energetics and non-radiative decay pathways.

These mechanistic differences are reflected in the choice of probe for specific applications. One common response is fluorogenic behaviour, where fluorescence intensity increases in less polar or more hydrophobic environments due to the environmental restriction of non-radiative decay pathways (Fig. 1.9A).[90] This is often associated with reduced solvent-mediated relaxation and restricted intramolecular motions. A classical example is *8-anilinonaphthalene-1-sulfonic acid (ANS)*, which exhibits very weak fluorescence in aqueous solution but becomes strongly emissive when bound to hydrophobic sites in proteins or membranes.[90]

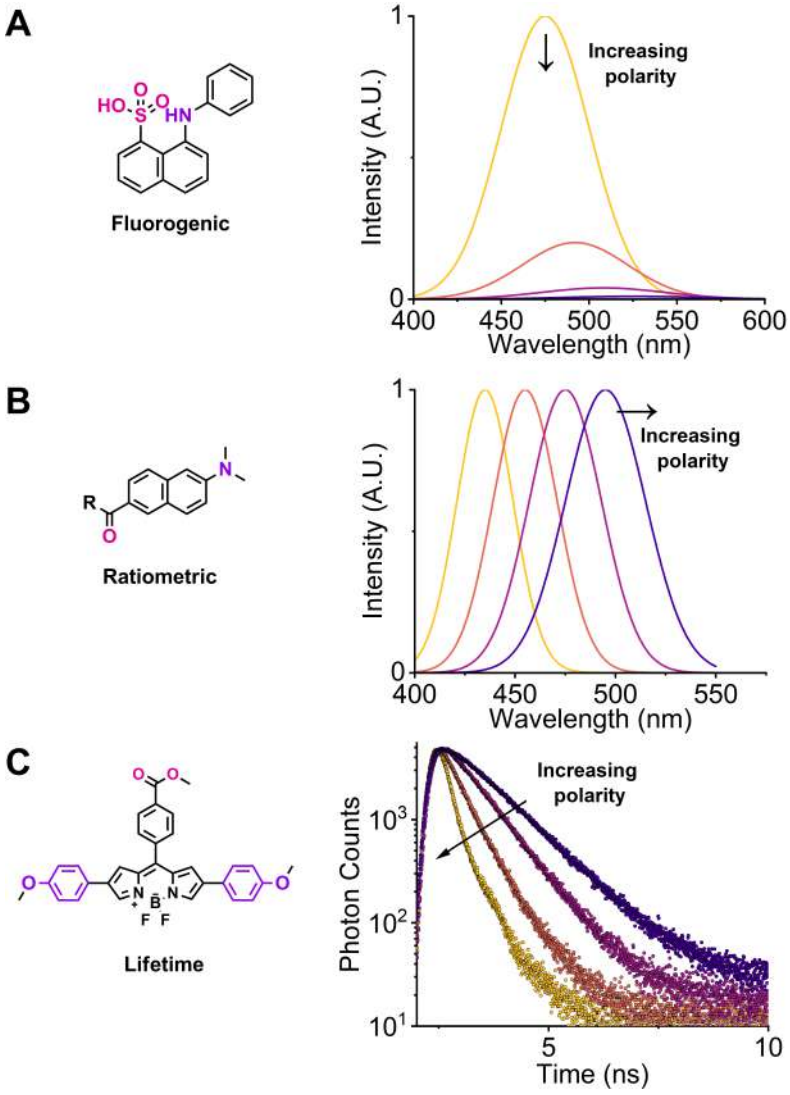

Figure 1.9: Representative polarity probes employing different fluorescence readout strategies. (A) Fluorogenic (intensity-based) probe ANS.[90] (B) Ratiometric (solvatochromic) probe Laurdan.[91] (C) Fluorescence lifetime-based BODIPY probe.[92] Adapted with permission from refs.[90–92]

Another widely used response is solvatochromism, where the emission spectrum shifts as a function of solvent polarity due to differential stabilization of LE and ICT states (Fig. 1.9B).[93] This spectral shift enables ratiometric measurements, which allow polarity changes to be quantified largely independently of probe concentration. A well-known

example is *Laurdan*, whose emission maximum depends strongly on the polarity and hydration of lipid membranes and is commonly used to characterize membrane phase behaviour.[91]

A third type of response involves changes in fluorescence lifetime, where solvent polarity influences the excited-state dynamics of the probe primarily by modulating non-radiative decay pathways (k_{nr}), with smaller contributions from changes in the radiative rate (Fig. 1.9C).[94] In lifetime-based probes, changes in excited-state relaxation kinetics translate into variations in fluorescence lifetime. While this readout allows for the mapping of spatial variations in local environments with high sensitivity, it is typically more sensitive to additional environmental parameters such as local dynamics, temperature, and molecular mobility. Consequently, the development of polarity-sensitive probes based on fluorescence lifetime remains comparatively limited, and only a relatively small number of systems have been reported to date. Certain donor–acceptor fluorophores, including modified *BODIPY* derivatives, have been developed to enable polarity sensing using fluorescence lifetime measurements.[34;92;95]

While these probes differ in their readout modality, they all ultimately report on the same underlying physical quantity: the effective solvation environment experienced by the fluorophore. In biological systems, this quantity is not equivalent to a single thermodynamic parameter such as the dielectric constant, but instead emerges from a convolution of electrostatic interactions, hydrogen bonding, dipolar relaxation, and local structural constraints.[96]

This complexity becomes particularly evident in lipid membranes, where polarity-sensitive probes are widely used to report on membrane organization and lipid phase behaviour.[97;98] In such environments, the measured probe response often reflects a combination of interfacial hydration, the presence of polar or charged species, and the organization of surrounding dipoles. For example, L_d phases are generally associated with higher hydration and increased probe response, whereas L_o phases exhibit reduced hydration and slower solvent relaxation due to tighter lipid packing.[97;98]

However, this interpretation may not hold in the presence of lipid oxidation products, which can locally increase polarity independently of membrane phase.[99] Similarly, the presence of charged proteins, carbohydrates, or other interfacial components can alter water structuring and dipolar organization, leading to complex and sometimes ambiguous probe responses.[100]

In addition, many polarity-sensitive fluorophores exhibit a degree of microviscosity sensitivity, particularly those capable of TICT states.[101] In these systems, excitation leads to the formation of a highly polar excited state with an increased dipole moment, which enhances sensitivity to the surrounding dielectric environment.[102] However, access to the TICT state typically involves intramolecular rotation, such that the rate of non-radiative decay depends not only on solvent polarity but also on the rotational freedom of the molecular framework.[103] This rotational motion is, in turn, modulated by local viscosity, molecular crowding, and temperature, introducing an additional layer of environmental sensitivity.[101;102;104] As a result, the fluorescence response of TICT-based probes reflects a coupled dependence on polarity, microviscosity, and solvent relaxation dynamics. In lipid membranes, polarity and microviscosity are often correlated, resulting in a cooperative enhancement of probe sensitivity.

However, this correlation is not universal. Situations in which polarity and viscosity are decoupled, such as lipid peroxidation, interfacial crowding, or heterogeneous membrane domains can lead to misleading fluorescence responses. Furthermore, many polarity-sensitive probes localize preferentially at the membrane interface rather than the hydrophobic core. At the interface, solvent relaxation processes remain partially active.[105;106] Consequently, changes in probe orientation, depth of insertion, or local microenvironment can significantly influence the measured signal independently of bulk membrane properties.[105;106] These factors highlight that polarity-sensitive fluorescence readouts in lipid systems reflect a convolution of multiple environmental parameters and should be interpreted with careful consideration of the underlying chemical context.

These principles are widely exploited in lipid membrane studies, where polarity-sensitive probes report on membrane organization across systems of increasing structural and biological complexity, from model membranes to live cells (Fig. 1.10).[91;107;108] Despite the interpretive challenges, their diverse readout mechanisms enable the visualization of membrane organization, lipid phase separation, and dynamic cellular processes such as membrane remodeling and programmed cell death.

As was shown with *Laurdan* and related derivatives, sensitivity to polarity and hydration enables imaging of lipid order, which describes the organization of lipid microdomains.[109] The liquid-ordered phase, enriched in cholesterol and saturated lipids, displays lower apparent polarity due to reduced water penetration and slower dipolar relaxation in tightly packed lipid environments.[110]

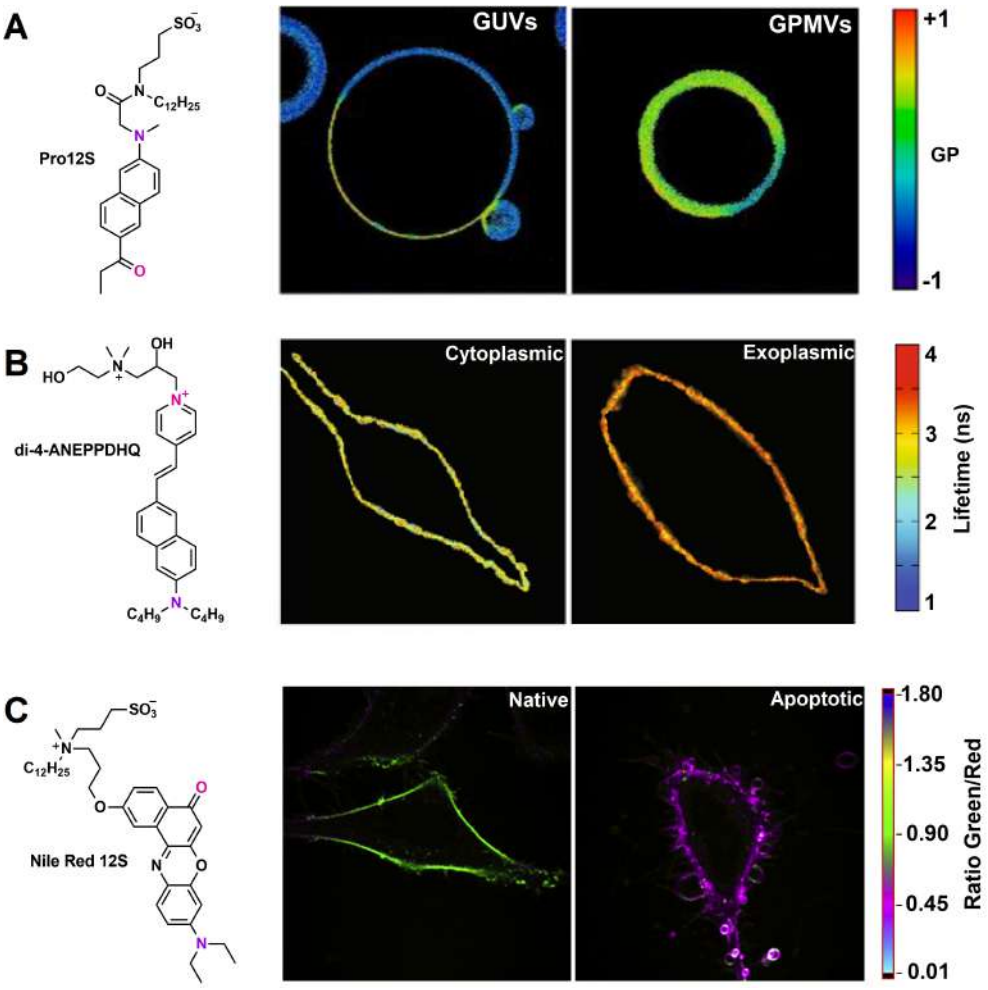

Figure 1.10: Representative applications of polarity probes for imaging polarity in model and live cell membranes. (A) Ratiometric imaging of Pro12S in giant GUVs and GPMVs, displaying distinct membrane order phases through GP.[91] (B) FLIM of di-4-ANEPPDHQ in rat basophilic leukemia mast cells, showing differences in plasma membrane polarity.[107] (C) Ratiometric imaging of Nile Red 12S in HeLa cells displaying differences between intact and apoptotic cells.[108] Adapted with permission from refs.[91;107;108]

Laurdan derivative *Pro12S* was used for ratiometric polarity imaging of GUVs and GPMVs, demonstrating that polarity-based readouts can distinguish lipid phases not only in model systems but also in more complex membrane-derived cellular systems (Fig. 1.10A).[91]

At higher biological complexity, the polarity probe *di-4-ANEPPDHQ*, which exhibits mixed sensitivity to polarity and membrane packing, was used in combination with FLIM to resolve differences between the cytoplasmic and exoplasmic plasma membrane leaflets (Fig. 1.10B).[107] The exoplasmic leaflet was found to be less polar and more ordered, as reflected by longer fluorescence lifetimes compared to the cytoplasmic leaflet. Importantly, although this probe preferentially labels the outer leaflet, inner leaflet properties were accessed via microinjection, enabling direct comparison of leaflet asymmetry.

Finally, apparent changes in plasma membrane polarity during apoptotic cell death were observed using the *Nile Red* derivative *Nile Red 12S* in ratiometric imaging (Fig. 1.10C).[108] A decrease in the GP index suggests that programmed cell death is accompanied by coupled changes in membrane composition, organization, and hydration, which collectively alter the probe-reported polarity.

In summary, while polarity probes must be interpreted within a specific chemical and structural context, they remain uniquely versatile tools for probing complex biological environments. Their sensitivity to subtle environmental changes has enabled applications ranging from model membrane systems to live-cell imaging of pathological states, where multiple physicochemical parameters, such as lipid remodeling, membrane asymmetry, and cellular stress responses, evolve simultaneously. In this sense, polarity-sensitive fluorophores act as reporters of local solvation landscapes, integrating multiple physicochemical parameters into a single measurable signal.

Chapter 2

Experimental

2.1 Materials and Reagents

All chemicals and solvents were obtained from commercial suppliers and used without further purification unless otherwise stated. Most of the reagents were obtained from Sigma-Aldrich. Lipids used in model membrane systems were obtained from Avanti Polar Lipids. Spectroscopic-grade solvents were used for photophysical measurements.

Stock solutions of fluorescent probes (1–2 mM), including *BODIPY-Lys*, *BODIPY-LD*, *BP-Ph-LD*, and *BODIPY-PM*, were prepared in toluene, methanol, water, or dimethyl sulfoxide (DMSO), depending on solubility. These solutions were further diluted in the corresponding solvents or solvent mixtures for spectroscopic and imaging experiments.

Stock solutions of auxiliary dyes used in cellular experiments, including *Neutral Red*, *DCFH-DA*, *BP-ester*, *BODIPY 493/503*, *Nile Red*, and *rhodamine 6G*, were prepared in DMSO at concentrations of 0.1–5 mM.

Stock solutions of pharmacological reagents and cellular perturbation agents, including sertraline, astemizole, doxorubicin, etoposide, α-tocopherol, and erastin, were prepared in DMSO (10 mM) and diluted to the desired concentrations prior to experiments.

2.2 Formation of Artificial Lipid Systems

All artificial lipid membrane systems used in this work, including tethered lipid bilayer membranes (tBLMs), large unilamellar vesicles (LUVs), and giant unilamellar vesicles (GUVs), were prepared from multilamellar vesicles (MLVs). MLVs were generated by dissolving appropriate lipids in chloroform (total lipid concentration 1 mM), evaporating the solvent under a nitrogen stream, and hydrating the resulting lipid film with water or buffer. Depending on the desired membrane system, MLVs were either extruded to produce LUVs, applied to solid surfaces for the preparation of tBLMs, or subjected to electroformation to generate GUVs.

2.2.1 Large Unilamellar Vesicles (LUVs)

LUVs were obtained by extruding MLVs through polycarbonate membranes (100 nm) using a syringe extruder (Avanti Polar Lipids). Lipids were mixed in desired ratios, and BODIPY probes were incorporated at a dye-to-lipid ratio of 1:800 prior to film formation. For compositions containing saturated lipids, such as DOPC/DPPC/Chol (1:5:5), the buffer was preheated to 60 °C, and extrusion was performed above the lipid melting temperature. Lipid suspensions were sonicated for 1 h prior to extrusion to ensure homogeneity.

2.2.2 Tethered Lipid Bilayer Membranes (tBLMs)

tBLMs were formed by applying MLVs onto 100 nm gold-coated mica surfaces in the presence of 20-tetradecyloxy-3,6,9,12,15,18,22-heptaoxahexatriacontane-1-thiol (WC14) and β-mercaptoethanol at a 3:7 molar ratio as an anchoring layer. For lipid mixtures containing saturated lipids (DOPC/DPPC/Cholesterol (Chol), DOPC/Brain sphingomyelin (BSM)/Chol), the MLVs were resuspended in PBS buffer preheated to 60 °C, above the lipid phase transition temperature, and membrane formation was carried out in an oven with slow cooling from 60 °C to 20 °C over 2 h. Membranes were gently washed in PBS and stained with 1 µM BODIPY probes for 3 min. Subsequently, the membranes were rinsed with PBS to remove unbound dye molecules.

2.2.3 Giant Unilamellar Vesicles (GUVs)

GUVs were formed by depositing lipid/BODIPY mixtures (dye-to-lipid ratio 1:800) on indium tin oxide (ITO) slides and evaporating the solvent under nitrogen for at least 2 h. The chamber was assembled with a second ITO slide separated by a spacer and filled with 400 mM sucrose solution. Electroformation was performed by applying a sinusoidal voltage (typically 1 V, 10 Hz, 2 h) with a detachment phase at 2 Hz for 30 min. For saturated lipid mixtures, electroformation was carried out above the lipid melting temperature (60 °C) and increased voltage amplitude (2.5 V). After formation, GUVs were immobilized in 0.5% w/v agarose gel[111] and transferred to μ-Dish imaging chambers (Ibidi).

2.2.4 Artificial Lipid Droplets (aLDs)

Artificial lipid droplets (aLDs) were prepared separately by directly mixing trilinolenin and DOPC at a 90:10 molar ratio, followed by gentle vortexing to ensure homogeneity. BODIPY probes were incorporated at 0.25 µM final concentration (from DMSO stock) prior to imaging.

2.3 Absorption, Steady-State, and Time-Resolved Fluorescence

Absorption spectra were recorded using a Jasco V-670 spectrophotometer. Fluorescence emission spectra were measured with an Edinburgh FLS920 spectrofluorometer (Edinburgh Instruments) equipped with a Fianium white-light laser excitation source. Excitation was selected using band-pass filters (Thorlabs) centered at 488 nm and 633 nm (full width at half maximum, FWHM = $\pm$3 nm). Excitation wavelengths were selected according to the absorption maxima of the investigated probes.

Fluorescence lifetime measurements were performed using time-correlated single-photon counting (TCSPC). Fluorescence decay curves were recorded with 5000 counts at the maximum of the decay histogram, using a 20 ns acquisition window and 4096 time channels. The instrument response function (IRF) was determined using a scattering sample, with a $\mathrm{FWHM_{IRF}}$ of approximately 415 ps.

All spectroscopic measurements were performed in 10 mm quartz cuvettes using BODIPY probe concentrations of up to 2 µM. Fluorescence decay measurements in pure solvents and solvent mixtures were carried out at 20 °C.

2.4 Cell Culture and Imaging Sample Preparation

Cells used for imaging experiments were cultured in Dulbecco's Modified Eagle's Medium (DMEM) supplemented with 10% fetal bovine serum (FBS), 100 IU/mL penicillin, and 100 µg/mL streptomycin (Thermo Fisher Scientific). Cells were maintained at 37 °C in a humidified atmosphere containing 5% CO_2. Experiments were initiated during the exponential (logarithmic) growth phase.

Cell lines used in this study included A549, HEK 293T, U-87 MG, MCF-7, HepG2, MDA-MB-231, HMF, WPMY-1, and RPE-1 cells.

Prior to imaging, cells were seeded into μ-Dish imaging chambers (Ibidi) at a density of approximately $1 \cdot 10^4$ cells per dish and allowed to adhere and grow for 24 h. For fluorescence imaging, BODIPY probes were added to the culture medium from DMSO stock solutions at final concentrations of 0.1–1 µM and incubated for 5–60 min at 37 °C. Imaging experiments were performed in phenol red-free DMEM (supplemented with 10% FBS, 100 IU/mL penicillin, and 100 µg/mL streptomycin).

2.5 Fluorescence Lifetime Imaging Microscopy (FLIM)

FLIM measurements were performed using a Leica SP8 confocal microscope (Leica Microsystems) equipped with a 63× oil immersion objective (HC PL APO, N.A. 1.4). Excitation was provided by a supercontinuum white-light laser using 488 nm and 633 nm laser lines selected via the AOBS system. Emission was collected using the Leica SP8 spectral detection system with detection windows set to 500–550 nm and 650–700 nm.

FLIM images were acquired at a spatial resolution of 512 × 512 pixels with 128 channels in the time domain. For reliable biexponential fitting, pixels were binned to achieve at least 1000 counts at the maximum of the fluorescence decay.

Only pixels corresponding to cellular structures of interest were included in the lifetime analysis. Regions of interest were defined from fluorescence intensity images by selecting the bright organelle-associated signal and excluding background and low-intensity non-specific staining. In most experiments, the fluorescence intensity of the target organelles was typically one to two orders of magnitude higher than that of the surrounding cytoplasm, allowing clear visual discrimination of the structures of interest. Intensity thresholds were adjusted individually for each image to account for variations in signal level and acquisition conditions.

The instrument response function (IRF) was determined by recording the scattered excitation light from a dilute aqueous suspension of Ludox colloidal silica.

2.6 Data Analysis

2.6.1 Time-Correlated Single-Photon Counting (TCSPC)

Solution-phase fluorescence decay curves were analyzed using the native software of the Edinburgh FLS920 spectrofluorometer (Edinburgh Instruments). The decays were fitted using a monoexponential model by iterative reconvolution with the instrument response function (IRF). The quality of the fits was evaluated using the reduced chi-squared (χ^2) statistic, and fits with $\chi^2 \leq 1.5$ were considered acceptable.

2.6.2 Fluorescence Lifetime Imaging Microscopy (FLIM)

FLIM data were analyzed using FLIMfit software (version 4.6.1, Imperial College London).[112] Fluorescence decays were fitted using a biexponential decay model. Intensity-weighted mean lifetimes were calculated according to Equation 2.1:

$$\tilde{\tau} = \frac{\sum_i a_i \tau_i^2}{\sum_i a_i \tau_i} \tag{2.1}$$

where a_i and τ_i represent the amplitude and lifetime of the ith decay component, respectively. The quality of the fits was assessed using the reduced chi-squared (χ^2) statistic, and fits with $\chi^2 \leq 1.3$ were considered

acceptable. The different χ^2 acceptance criteria reflect the different decay models applied in TCSPC (monoexponential) and FLIM (biexponential) analysis.

Chapter 3

Results and Discussion

3.1 Designing a green-emitting viscosity-sensitive 4, 4-difluoro-4-bora-3a, 4a-diaza-s-indacene (BODIPY) probe for plasma membrane viscosity imaging

This work aimed to develop a green-emitting, viscosity-sensitive BODIPY-based fluorescent probe for quantitative fluorescence lifetime imaging of plasma membrane microviscosity in model membranes and live cells. Although numerous BODIPY molecular rotors have been reported, achieving a combination of good aqueous solubility, low polarity sensitivity, and efficient incorporation into both L_o and L_d membrane phases remains challenging.[39;113] To address these requirements, a water-soluble plasma membrane-targeting probe containing a sulfonate group, *BODIPY-PM*, was designed (Fig. 3.1A).[114] The resulting green-emitting fluorophore (500–600 nm) combines aqueous solubility with viscosity-sensitive fluorescence lifetime behavior (Fig. 3.1B,C).

The probe exhibited excellent aqueous solubility and showed no observable aggregation at concentrations up to 4 µM in pure water at pH 7 and room temperature. Photophysical characterization demonstrated a strong viscosity-dependent fluorescence lifetime response, with lifetimes increasing from 122 ps in methanol (1 cP) to 5127 ps in glycerol (930 cP) (Fig. 3.1C). In contrast, solvent polarity exerted only a minor influence on fluorescence lifetime, with values decreasing from 376 ps in chloroform to 264 ps in water despite the substantial difference in solvent

polarity. These results indicate that fluorescence lifetime is governed predominantly by viscosity rather than polarity.

The performance of *BODIPY-PM* was evaluated in LUVs, tBLMs, and live cells. In LUVs, the probe successfully incorporated into both L_o and L_d membrane phases without detectable aggregation. Intensity-weighted fluorescence lifetimes were 877 ps in DOPC LUVs, representing L_d membranes, compared with 3321 ps in DOPC:DPPC:Chol (1:5:5) LUVs corresponding to the L_o phase.[115;116] In phase-separated DOPC:DPPC:Chol (1:1:1) LUVs,[117] FLIM resolved coexisting L_o and L_d domains, demonstrating that the probe provides sufficient fluorescence signal in both lipid phases (Fig. 3.1D).

Additional studies in tBLMs revealed a progressive increase in fluorescence lifetime from approximately 500 ps in pure DOPC membranes to approximately 1900 ps in DOPC (50:50) membranes, confirming sensitivity to cholesterol-induced membrane ordering.[118]

Application of *BODIPY-PM* to live A549 cells demonstrated preferential localization to the plasma membrane and enabled quantitative determination of membrane microviscosity (Fig. 3.1E). Fluorescence lifetimes corresponded to plasma membrane viscosities of approximately 300–400 cP, in good agreement with previously reported values for mammalian cell plasma membranes.[76]

Overall, this study introduces a water-soluble viscosity-sensitive molecular rotor with reduced polarity artefacts, broad viscosity sensitivity, and balanced partitioning between L_o and L_d lipid phases. These properties enable quantitative FLIM-based measurements of plasma membrane microviscosity in both model membrane systems and live cells, providing a versatile tool for investigating membrane organization.

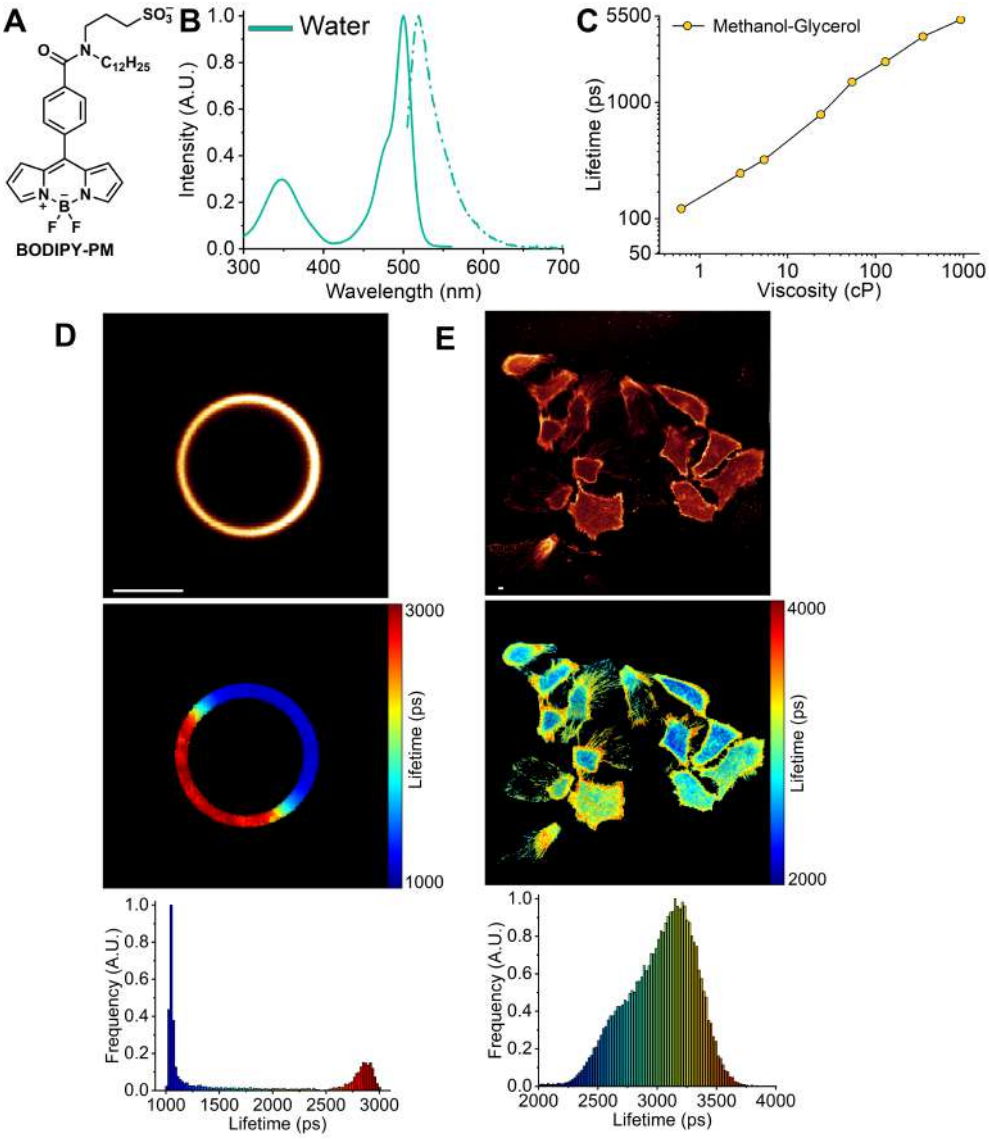

Figure 3.1: Application of the viscosity-sensitive plasma membrane probe BODIPY-PM. (A) Chemical structure of BODIPY-PM. (B) Absorption (solid line) and fluorescence emission (dash-dotted line) spectra of BODIPY-PM in water. (C) Fluorescence lifetime dependence of BODIPY-PM on viscosity in methanol–glycerol mixtures. (D) FLIM of BODIPY-PM DOPC:DPPC:Chol (1:1:1) LUVs. (E) FLIM of BODIPY-PM in A549 cells. For panels D and E, the upper row shows fluorescence intensity images, the middle row shows fluorescence lifetime maps, and the lower row shows the corresponding fluorescence lifetime histograms. Scale bars: 1 µm.

3.2 Bimodal effects on lipid droplets induced in cancer and non-cancer cells by chemotherapy drugs as revealed with a green-emitting BODIPY fluorescent probe

The primary aim of this study was to develop a LD-specific, viscosity-sensitive fluorescent probe suitable for quantitative FLIM measurements of LD microviscosity and to apply it to investigate LD physicochemical properties in different cellular models and under chemotherapeutic stress. LDs have attracted considerable attention in cancer biology because their abundance is frequently elevated in malignant cells and tumor tissues, where they are increasingly recognized as biomarkers of cancer progression.[119–121] Furthermore, LD accumulation has been linked to altered drug distribution, impaired apoptosis, and the emergence of chemotherapy resistance.[119;122] While LD abundance is routinely evaluated, considerably less is known about how the physical properties of LDs, such as microviscosity, vary between cellular phenotypes or respond to chemotherapeutic treatment. To address this question, a bulky and hydrophobic molecular rotor, *BODIPY-LD*, was designed by introducing two cyclohexyl substituents at the *meso*-phenyl group of the BODIPY core (Fig. 3.2A).[123] The resulting green-emitting probe (500–600 nm) preferentially partitions into the neutral lipid core of LDs, enabling highly selective staining of these organelles.

Photophysical characterization demonstrated a strong fluorescence lifetime dependence on viscosity over a broad range, spanning from 0.63 to 1457 cP and producing lifetime changes from 92 to 4639 ps (Fig. 3.2B). In contrast, the influence of solvent polarity on the fluorescence decay was comparatively small, with fluorescence lifetimes varying only from 92 ps in methanol ($\Delta f = 0.30$) to 147 ps in cyclohexane ($\Delta f = 0$). In model membrane systems, the probe clearly discriminated between lipid compositions known to form L_o and L_d phases. Intensity-weighted fluorescence lifetimes were 3.6 ns in DOPC:DPPC:Chol (1:5:5) LUVs, a composition corresponding to the L_o phase,[115;116] compared with 1.24 ns in DOPC and 1.30 ns in POPC LUVs representing L_d membranes, an approximately three-fold difference. Addition of cholesterol to DOPC LUVs progressively increased the fluorescence lifetime from 1.24 ns to 1.63 ns (25 mol% cholesterol) and 2.13 ns (50 mol% cholesterol), demonstrating sensitivity to cholesterol-induced membrane ordering.[118]

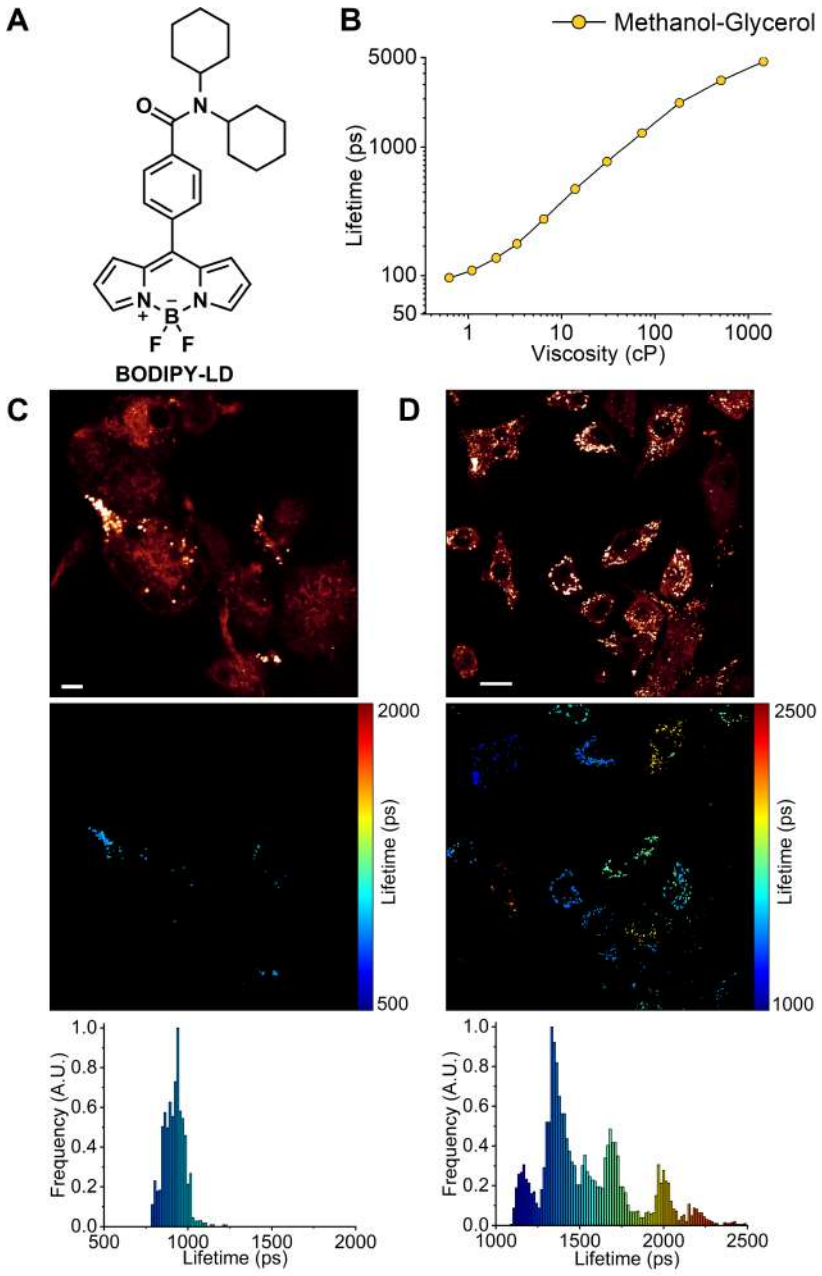

Figure 3.2: Application of the viscosity-sensitive LD probe BODIPY-LD. (A) Chemical structure of BODIPY-LD. (B) Fluorescence lifetime dependence of BODIPY-LD on viscosity in methanol–glycerol mixtures. (C) Representative FLIM images of BODIPY-LD in HEK 293T cells. (D) Representative FLIM images of BODIPY-LD in A549 cells. For panels C and D, the upper row shows fluorescence intensity images, the middle row shows fluorescence lifetime maps, and the lower row shows the corresponding fluorescence lifetime histograms. Scale bars: 10 μm.

Live-cell imaging confirmed highly selective localization of *BODIPY-LD* to LDs. In A549 cells, fluorescence intensities within LDs were typically around 100-fold higher than those observed in the surrounding cytoplasm, while co-localization experiments with Nile Red verified the identity of the stained structures as LDs.[124]

To evaluate whether LD microviscosity differs between distinct cellular phenotypes, FLIM measurements were performed in immortalized HEK 293T cells and malignant A549 lung adenocarcinoma cells. HEK 293T cells contained relatively few LDs and exhibited narrow fluorescence lifetime distributions corresponding to microviscosities of approximately 25–50 cP (Fig. 3.2C). In contrast, A549 cells displayed a substantially higher abundance of LDs together with pronounced intercellular heterogeneity, with LD microviscosities spanning approximately 60–270 cP (Fig. 3.2D). While LDs within individual A549 cells generally exhibited similar microviscosities, the average values varied markedly between cells, resulting in multiple distinct LD microviscosity populations across the cell population. These observations indicate significant cell-to-cell differences in LD microviscosities and suggest that LD microviscosity provides information beyond LD abundance alone, reflecting variations in LD composition and organization associated with malignant phenotypes.[125;126]

The effects of the chemotherapeutic agents doxorubicin (DOX) and etoposide (ETP) on LD microviscosity were further examined in A549 cells. Both drugs increased LD abundance and induced remodeling of LD microviscosity distributions. After 24 h of DOX treatment, a bimodal microviscosity distribution emerged, with low-viscosity LD populations (30–50 cP) and high-viscosity LD populations (180–300 cP) coexisting within the same cells, while the intermediate-viscosity population ($\sim$90 cP) largely disappeared.

Overall, this study establishes *BODIPY-LD* as a selective and reliable probe for quantitative FLIM-based measurements of LD microviscosity. The results demonstrate that LD microviscosity provides complementary information to LD abundance, revealing differences between cellular phenotypes and drug-induced remodeling of LDs.

3.3 Cancer Cell Identification via Lysosomal Membrane Microviscosities using a Green-Emitting BODIPY Molecular Rotor

This work aimed to develop a lysosome-targeting, viscosity-sensitive molecular rotor for quantitative imaging of lysosomal membrane microviscosity in live cells and to evaluate whether lysosomal membrane microviscosity can serve as a distinguishing feature of cancer-derived and non-malignant cell phenotypes. A green-emitting BODIPY-based probe, BODIPY-Lys, was designed by introducing a morpholine targeting group into the BODIPY scaffold (Fig. 3.3A), producing fluorescence in the 500–600 nm spectral region.[127]

Photophysical characterization demonstrated strong fluorescence lifetime sensitivity to viscosity over a broad range, with lifetimes increasing from 71 ps in methanol (0.6 cP) to 4545 ps in glycerol (1457 cP) (Fig. 3.3B). In contrast, solvent polarity exerted only a minor influence on the fluorescence decay, with lifetimes varying from 71 ps in methanol to 126 ps in cyclohexane. Fluorescence lifetimes were also largely insensitive to temperature over the investigated range (20–70 °C, DMSO), exhibiting a relative fluorescence lifetime sensitivity of only 0.15% $°C^{-1}$.

Live-cell imaging demonstrated selective accumulation of *BODIPY-Lys* in lysosomes, with fluorescence intensities approximately 10–100-fold higher than those observed in the surrounding cytoplasm. Colocalization experiments with the lysosomal marker Neutral Red[128] confirmed lysosomal targeting.

Lysosomal membrane organization may differ between cancer-derived and non-malignant cells as a consequence of altered lipid metabolism. Malignant transformation is frequently accompanied by increased reactive oxygen species production and changes in lipid composition, including elevated levels of saturated lipids and oxidized lipid species.[129–131] Such compositional changes can modify lipid packing and membrane order,[5;74;132] suggesting that lysosomal membrane microviscosity may provide information on phenotypic differences between cell types.

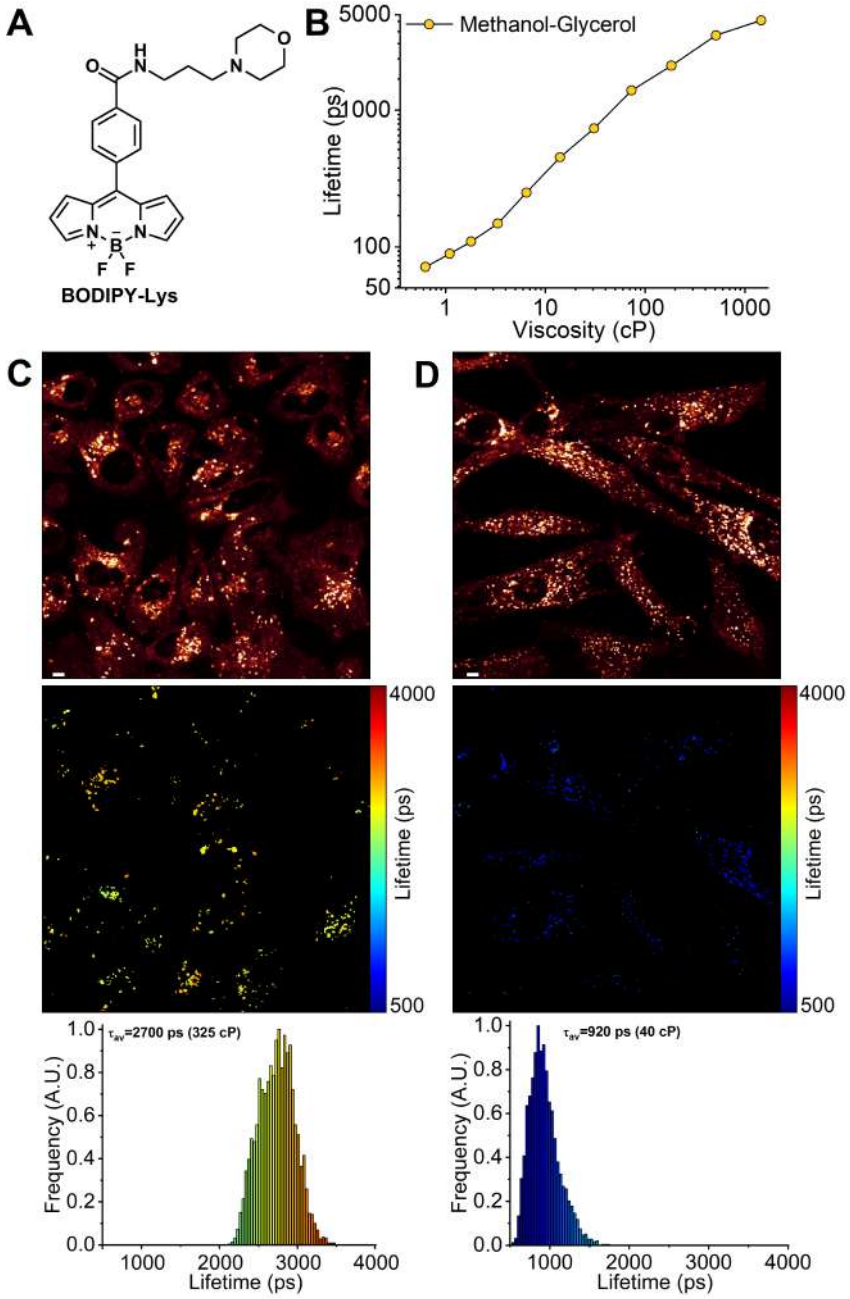

Figure 3.3: Application of the lysosome-targeting viscosity probe BODIPY-Lys. (A) Chemical structure of BODIPY-Lys. (B) Fluorescence lifetime dependence of BODIPY-Lys on viscosity. (C) FLIM of BODIPY-Lys in A549 cells. (D) FLIM of BODIPY-Lys in HMF cells. For panels C and D, the upper row shows fluorescence intensity images, the middle row shows fluorescence lifetime maps, and the lower row shows the corresponding fluorescence lifetime histograms. Scale bars: 5 μm.

FLIM measurements were subsequently performed in four cancer-derived cell lines (A549, U-87 MG, MCF-7, and HepG2) and four non-malignant or immortalized cell lines (HMF, WPMY-1, RPE-1, and HEK 293T). Lysosomal membrane microviscosities were consistently higher in cancer-derived cells, ranging from approximately 200 to 325 cP, compared with 40 to 135 cP in the non-malignant and immortalized cell lines. Mean microviscosities were approximately 325 cP for A549, 200 cP for U-87 MG, 250 cP for MCF-7, and 250 cP for HepG2 cells, whereas HMF, WPMY-1, RPE-1, and HEK 293T cells exhibited values of approximately 40, 85, 90, and 135 cP, respectively (Fig. 3.3C and D). These results demonstrate that lysosomal membrane microviscosity differs substantially between cell types and can distinguish cancer-derived cells from non-malignant and immortalized cell models.

Lysosomes have emerged as attractive therapeutic targets in cancer because lysosomal membrane permeabilization can trigger lysosome-dependent cell death through the release of hydrolytic enzymes into the cytoplasm.[133–135] Unlike apoptosis, this pathway can operate independently of caspase activation and may therefore be effective against apoptosis-resistant cancers.[133;136] Among the compounds capable of inducing lysosome-dependent cell death are cationic amphiphilic drugs (CADs), which preferentially accumulate within acidic lysosomes and perturb lysosomal membrane integrity.[135–137]

To investigate how pharmacological induction of lysosomal membrane permeabilization affects membrane organization, cells were treated with the CADs sertraline and astemizole. FLIM measurements revealed that these compounds exerted markedly different effects on lysosomal membrane microviscosity. In MCF-7 cells, sertraline increased lysosomal microviscosity from approximately 250 cP to 410 cP, while astemizole decreased it to approximately 150 cP. Similar trends were observed in HepG2 cells. Although both compounds are commonly used to induce lysosomal membrane permeabilization,[136;138] they produced opposite effects on lysosomal membrane microviscosity and, consequently, lipid packing. These observations suggest that lysosomal membrane permeabilization may be achieved through different molecular mechanisms depending on the CAD employed.

Overall, this study establishes *BODIPY-Lys* as a selective and quantitative FLIM probe for investigating lysosomal membrane microviscosity in live cells. The results demonstrate that lysosomal membrane microviscosity reflects both cell phenotype and pharmacologically induced membrane remodeling, providing a sensitive biophysical marker of lysosomal membrane organization.

3.4 Quantitative FLIM Imaging of Lipid Droplet Polarity with a BODIPY Probe Reveals Biophysical Signatures of Ferroptosis Resistance

This work aimed to develop a polarity-sensitive fluorescent probe for quantitative imaging of LD polarity and its role in ferroptosis and the emergence of drug resistance. LDs are increasingly recognized as dynamic organelles involved in cellular lipid homeostasis and protection against oxidative stress, serving as reservoirs that can sequester and remodel lipids during metabolic adaptation.[139;140] Recent studies have implicated LDs in ferroptosis,[139;141] a non-apoptotic, iron-dependent form of regulated cell death driven by lipid peroxidation.[142] A deep-red-emitting BODIPY-based probe *(BP-Ph-LD)*[92] was designed with two methoxyphenyl substituents attached to the BODIPY core (Fig. 3.4D, lower panel). This substitution eliminates the viscosity sensitivity[34;143] characteristic of molecular rotors and shifts the fluorescence emission into the far-red spectral region (650–800 nm, Fig. 3.4A).

Photophysical characterization established the probe's sensitivity and selectivity. BP-Ph-LD exhibited monoexponential fluorescence decays in organic solvents, with lifetimes decreasing from 1025 ps in non-polar cyclohexane ($\Delta f = 0$) to 178 ps in methanol ($\Delta f = 0.30$), a nearly six-fold range (Fig. 3.4B). The fluorescence lifetime correlated with the orientation polarizability (Δf) and was essentially insensitive to viscosity, exhibiting identical fluorescence decays in low-viscosity toluene (0.6 cP) and highly viscous castor oil (930 cP). Fluorescence lifetimes were also largely insensitive to temperature over the investigated range (10–70 °C, toluene), exhibiting a relative fluorescence lifetime sensitivity of only 0.6% $°C^{-1}$.

In aLDs containing increasing fractions of peroxidised trilinolenin (TL-OOH), the intensity-weighted lifetime decreased systematically from 850 ps (0% TL-OOH) to 390 ps (100% TL-OOH), directly linking lifetime to the chemical polarity conferred by lipid peroxides (Fig. 3.4C).

Simultaneous staining of a mixed aLD/MLV system with *BP-Ph-LD* and a planar BODIPY analogue *BP-ester*[144] demonstrated that LD selectivity arises from molecular shape, not hydrophobicity alone: the planar *BP-ester* labeled both structures, whereas *BP-Ph-LD* accumulated almost exclusively in aLDs (Fig. 3.4D).

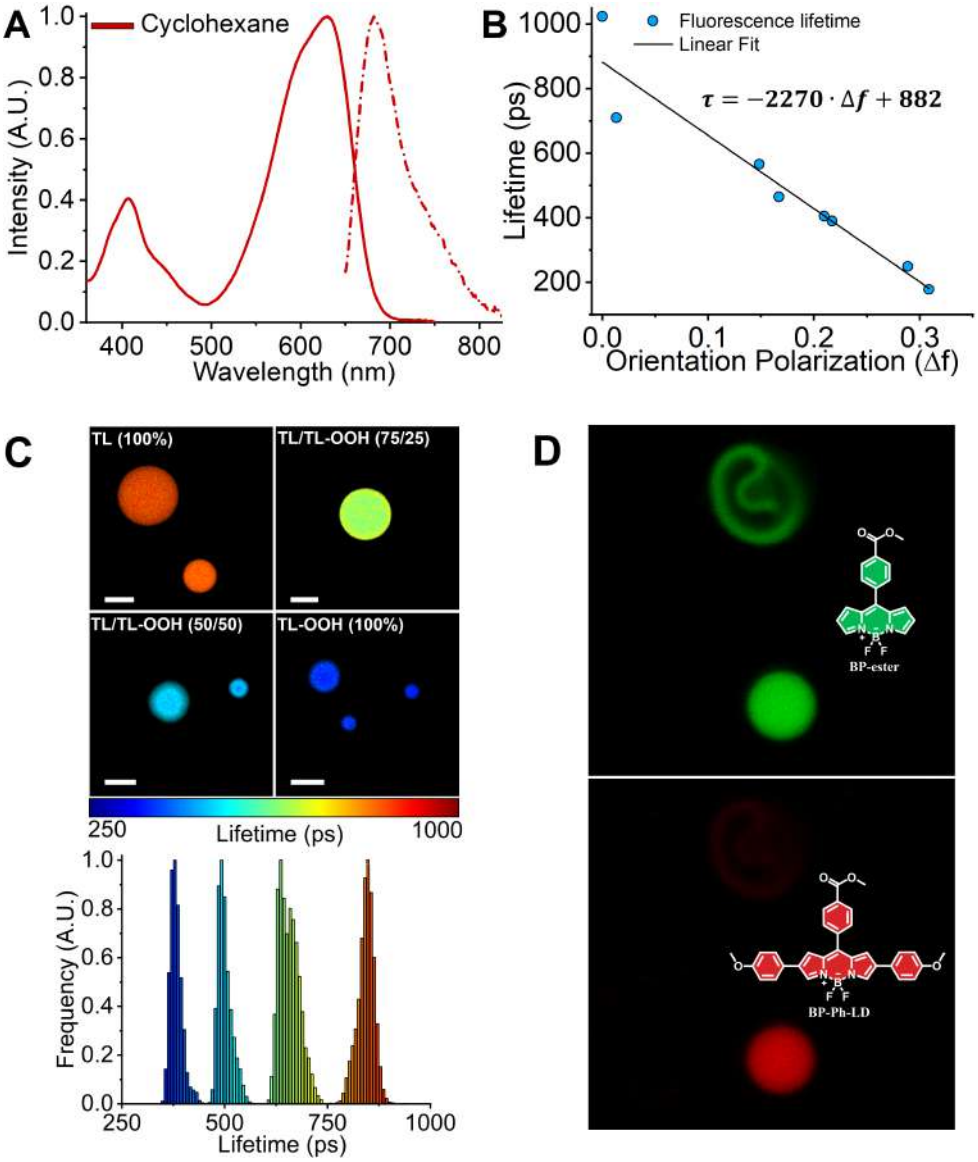

Figure 3.4: Application of the polarity-sensitive LD probe BP-Ph-LD. (A) Absorption (solid line) and fluorescence emission (dash-dotted line) spectra of BP-Ph-LD in cyclohexane. (B) Dependence of fluorescence lifetime on solvent polarity. (C) FLIM images of BP-Ph-LD in aLDs containing different fractions of lipid peroxides (TL-OOH). The corresponding fluorescence lifetime histograms are shown below. (D) Fluorescence intensity images of BP-ester (green, upper row) and BP-Ph-LD (red, lower row) in a mixed aLD/MLV system stained simultaneously with both probes. Scale bars: 5 µm.

Having validated the probe, *BP-Ph-LD* was applied to live MDA-MB-231 breast cancer cells to investigate LD polarity during ferroptosis and the emergence of ferroptosis resistance. Co-localization experiments with the established LD marker BODIPY 493/503[145] confirmed selective accumulation of *BP-Ph-LD* within LDs. Unlike conventional polarity probes that primarily report membrane hydration or lipid packing, *BP-Ph-LD* localizes within the hydrophobic core of LD, where water content is extremely low. Consequently, changes in fluorescence lifetime can be interpreted predominantly in terms of lipid composition, particularly the accumulation of polar lipid peroxidation products.[146;147]

Under basal conditions, LDs exhibited a mean fluorescence lifetime of approximately 800 ps, consistent with the low polarity expected for neutral lipid stores. Treatment with the ferroptosis inducer erastin resulted in a progressive decrease in fluorescence lifetime, from approximately 800 ps under basal conditions to 640 ps after 72 h, indicating increased LD polarity consistent with the accumulation of lipid peroxides during ferroptosis. After prolonged treatment, cells that acquired resistance exhibited a partial recovery of fluorescence lifetime to approximately 680 ps (120 h), suggesting a shift toward less polar and potentially less peroxidation-prone lipid compositions.

In addition to polarity changes, ferroptosis-resistant cells displayed morphological LD remodeling. Many LDs adopted irregular, non-spherical morphologies, which may reflect increased lipid saturation and a transition toward more ordered or semi-solid lipid phases.[148] FLIM-derived polarity maps further revealed spatial segregation of LD populations, with less polar LDs preferentially localized near the perinuclear region and more polar LDs distributed toward the cell periphery.

These observations indicate that LD polarity reflects underlying lipid composition and remodeling during ferroptosis and adaptation to ferroptotic stress. Furthermore, the probe design demonstrated that LD targeting is governed not only by hydrophobicity but also by molecular shape. The non-planar architecture of *BP-Ph-LD* promoted selective partitioning into isotropic LD environments, whereas a planar analogue distributed between LDs and lipid bilayers.

Overall, this study establishes *BP-Ph-LD* as a quantitative FLIM probe for monitoring LD polarity and demonstrates that reduced LD polarity, non-spherical droplet morphology, and spatial segregation of LD populations constitute biophysical signatures associated with the emergence of ferroptosis resistance.

Conclusions

This work demonstrates the development and application of fluorescence lifetime-based molecular probes for quantitative characterization of lipid microenvironments in live cells. A series of BODIPY-based fluorescent probes was designed to enable organelle-specific measurements of microviscosity in plasma membranes, LDs, and lysosomes, establishing FLIM as a quantitative approach for investigating local physicochemical properties in complex biological systems.

Using viscosity-sensitive molecular rotors, significant differences in membrane microviscosity were identified between cancer-derived and non-malignant cell models. Lysosomal membrane microviscosities were consistently higher in cancer-derived cell lines, enabling their discrimination based on membrane organization. In lipid droplets, cancer cells exhibited substantially greater organelle abundance together with broader and more heterogeneous microviscosity distributions than non-malignant cells, demonstrating that lipid droplet microviscosity provides information beyond organelle abundance alone.

The developed probes also enabled quantitative investigation of lipid remodeling induced by pharmacological treatments. Chemotherapeutic agents triggered redistribution of LD microviscosity populations, revealing dynamic changes in LD organization during cellular adaptation to chemotherapeutic stress. In lysosomes, CADS produced opposite effects on membrane microviscosity despite both inducing lysosomal membrane permeabilization, suggesting that lysosomal leakage may be achieved through distinct alterations of membrane organization.

The scope of this approach was further extended through the development of a polarity-sensitive LD probe capable of quantifying polarity independently of viscosity. This probe demonstrated that LD polarity increases during ferroptosis as a consequence of lipid peroxidation and partially decreases upon the emergence of ferroptosis res-

istance. Ferroptosis-resistant cells additionally exhibited characteristic biophysical signatures, including reduced LD polarity, non-spherical LD morphologies, and spatial segregation of LD populations according to polarity.

Beyond the biological applications, this work provides insight into the design principles of organelle-targeting fluorophores. In particular, selective targeting of LDs was shown to depend not only on hydrophobicity but also on molecular geometry, with non-planar fluorophores preferentially partitioning into isotropic LD environments rather than anisotropic lipid bilayers.

Overall, this thesis establishes fluorescence lifetime-based measurements of microviscosity and polarity as quantitative and spatially resolved indicators of membrane organization, lipid composition, and cellular adaptation. The results demonstrate that these parameters can reveal biophysical changes associated with cancer, chemotherapeutic stress, lysosomal membrane permeabilization, ferroptosis, and the emergence of drug resistance, providing new tools for investigating disease-related cellular remodeling in living systems.

Bibliography

[1] B. Fadeel and D. Xue. The ins and outs of phospholipid asymmetry in the plasma membrane: roles in health and disease. *Critical Reviews in Biochemistry and Molecular Biology*, 44:264–277, 2009. doi: 10.1080/10409230903193307.

[2] Y. Zhang and J. Lou. Impact of lipid asymmetry on membrane biophysical properties: Insights from molecular dynamics simulations. *Critical Reviews in Biochemistry and Molecular Biology*, 13:e89, 2025. doi: 10.1002/qub2.89.

[3] G. J. Schütz and G. Pabst. The asymmetric plasma membrane–a composite material combining different functionalities? *BioEssays*, 45:2300116, 2023. doi: 10.1002/bies.202300116.

[4] I. Schachter, R. O. Paananen, B. Fábián, P. Jurkiewicz, and M. Javanainen. The two faces of the liquid ordered phase. *The Journal of Physical Chemistry Letters*, 13:1307–1313, 2022. doi: 10.1021/acs.jpclett.1c03712.

[5] H.-J. Kaiser, D. Lingwood, I. Levental, J. L. Sampaio, L. Kalvodova, L. Rajendran, and K. Simons. Order of lipid phases in model and plasma membranes. *Proceedings of the National Academy of Sciences USA*, 106:16645–16650, 2009. doi: 10.1073/pnas.0908987106.

[6] D. M. Engelman. Membranes are more mosaic than fluid. *Nature*, 438:578–580, 2005. doi: 10.1038/nature04394.

[7] A. Ghysels, A. Krämer, R. M. Venable, W. E. Teague Jr., E. Lyman, K. Gawrisch, and R. W. Pastor. Permeability of membranes in the liquid ordered and liquid disordered phases. *Nature Communications*, 10:5616, 2019. doi: 10.1038/s41467-019-13432-7.

[8] G. M'Baye, Y. Mély, G. Duportail, and A. S. Klymchenko. Liquid ordered and gel phases of lipid bilayers: Fluorescent probes reveal close fluidity but different hydration. *Biophysical Journal*, 95:1217–1225, 2008. doi: 10.1529/biophysj.107.127480.

[9] D. Arrais and J. Martins. Bilayer polarity and its thermal dependency in the lo and ld phases of binary phosphatidylcholine/cholesterol mixtures. *Biochimica et Biophysica Acta – Biomembranes*, 1768:2914–2922, 2007. doi: 10.1016/j.bbamem.2007.

08.012.

[10] E. Sezgin, I. Levental, S. Mayor, and C. Eggeling. The mystery of membrane organization: composition, regulation and roles of lipid rafts. *Nature Reviews Molecular Cell Biology*, 18:361–374, 2017. doi: 10.1038/nrm.2017.16.

[11] E. Sezgin, F. Schneider, S. Galiani, I. Urbančič, D. Waithe, B. C. Lagerholm, and C. Eggeling. Measuring nanoscale diffusion dynamics in cellular membranes with super-resolution sted–fcs. *Nature Protocols*, 14:1054–1083, 2019. doi: 10.1038/s41596-019-0127-9.

[12] Y. Wu, M. Štefl, A. Olzyńska, M. Hof, G. Yahioglu, P. Yip, D. R. Casey, O. Ces, J. Humpolíčková, and M. K. Kuimova. Molecular rheometry: direct determination of viscosity in lo and ld lipid phases via fluorescence lifetime imaging. *Physical Chemistry Chemical Physics*, 15:14986–14993, 2013. doi: 10.1039/C3CP51953H.

[13] S. Oncul, A. S. Klymchenko, O. A. Kucherak, A. P. Demchenko, S. Martin, M. Dontenwill, Y. Arntz, P. Didier, G. Duportail, and Y. Mély. Liquid ordered phase in cell membranes evidenced by a hydration-sensitive probe: Effects of cholesterol depletion and apoptosis. *Biochimica et Biophysica Acta – Biomembranes*, 1798:1436–1443, 2010. doi: 10.1016/j.bbamem.2010.01.013.

[14] M. Javanainen, O. H. S. Ollila, and H. Martinez-Seara. Rotational diffusion of membrane proteins in crowded membranes. *The Journal of Physical Chemistry B*, 124:2994–3001, 2020. doi: 10.1021/acs.jpcb.0c00884.

[15] H. Raghu, P. K. Sodadasu, R. R. Malla, C. S. Gondi, N. Estes, and J. S. Rao. Localization of upar and mmp-9 in lipid rafts is critical for migration, invasion and angiogenesis in human breast cancer cells. *BMC Cancer*, 10:647, 2010. doi: 10.1186/1471-2407-10-647.

[16] J. B. Larsen, M. B. Jensen, V. K. Bhatia, S. L. Pedersen, T. Bjørnholm, L. Iversen, M. Uline, I. Szleifer, K. J. Jensen, N. S. Hatzakis, and D. Stamou. Membrane curvature enables n-ras lipid anchor sorting to liquid-ordered membrane phases. *Nature Chemical Biology*, 11:192–194, 2015. doi: 10.1038/nchembio.1733.

[17] K. A. Field, D. Holowka, and B. Baird. Fc epsilon ri-mediated recruitment of p53/56lyn to detergent-resistant membrane domains accompanies cellular signaling. *Proceedings of the National Academy of Sciences USA*, 92:9201–9205, 1995. doi: 10.1073/pnas.92.20.9201.

[18] P. Varshney, V. Yadav, and N. Sain. Lipid rafts in immune signalling: current progress and future perspective. *Immunology*, 149: 13–14, 2016. doi: 10.1111/imm.12617.

[19] K. Simons and J. L. Sampaio. Membrane organization and lipid rafts. *Cold Spring Harbor Perspectives in Biology*, 3:a004697, 2011. doi: 10.1101/cshperspect.a004697.

[20] A. M. Farnoud, A. M. Toledo, J. B. Konopka, M. Del Poeta, and Erwin London. Raft-like membrane domains in pathogenic microorganisms. *Current Topics in Membranes*, 75:233–268, 2015. doi: 10.1016/bs.ctm.2015.03.005.

[21] C. Peetla, A. Stine, and V. Labhasetwar. Biophysical interactions with model lipid membranes: Applications in drug discovery and drug delivery. *Molecular Pharmaceutics*, 6:1264–1276, 2009. doi: 10.1021/mp9000662.

[22] A. A. Combs. Fluorescence microscopy: A concise guide to current imaging methods. *Current Protocols in Neuroscience*, 50:2.1.1–2.1.14, 2010. doi: 10.1002/0471142301.ns0201s50.

[23] R. B. Lira, L. S. Dillingh, J.-J. Schuringa, G. Yahioglu, K. Suhling, and W. H. Roos. Fluorescence lifetime imaging microscopy of flexible and rigid dyes probes the biophysical properties of synthetic and biological membranes. *Biophysical Journal*, 123:1592–1609, 2024. doi: 10.1016/j.bpj.2024.04.033.

[24] E. D'Este, G. Lukinavičius, R. Lincoln, F. Opazo, and E. F. Fornasiero. Advancing cell biology with nanoscale fluorescence imaging: essential practical considerations. *Trends in Cell Biology*, 34:671–684, 2024. doi: 10.1016/j.tcb.2023.12.001.

[25] H. Szmacinski and J. R. Lakowicz. Fluorescence lifetime-based sensing and imaging. *Sensors and Actuators B: Chemical*, 29:16–24, 1995. doi: 10.1016/0925-4005(95)01658-9.

[26] K. Suhling, L. M. Hirvonen, J. A. Levitt, P.-H. Chung, C. Tregidgo, A. Le Marois, D. A. Rusakov, K. Zheng, S. Ameer-Beg, S. Poland, S. Coelho, R. Henderson, and N. Krstajic. Fluorescence lifetime imaging (flim): Basic concepts and some recent developments. *Medical Photonics*, 27:3–40, 2015. doi: 10.1016/j.medpho.2014.12.001.

[27] R. Datta, T. M. Heaster, J. T. Sharick, A. A Gillette, and M. C. Skala. Fluorescence lifetime imaging microscopy: fundamentals and advances in instrumentation, analysis, and applications. *Journal of Biomedical Optics*, 25:071203, 2020. doi: 10.1117/1.JBO.25.7.071203.

[28] A. Vyšniauskas, M. Qurash, N. Gallop, M. Balaz, H. L. Anderson, and M. K. Kuimova. Unravelling the effect of temperature on viscosity-sensitive fluorescent molecular rotors. *Chemical Science*, 6:5773–5778, 2015. doi: 10.1039/C5SC02248G.

[29] S.-C. Lee, J. Heo, H. C. Woo, J.-A. Lee, Y. H. Seo, C.-L. Lee, S. Kim, and O-P. Kwon. Fluorescent molecular rotors for viscosity sensors. *Chemistry – A European Journal*, 24:13706–13718, 2018. doi: 10.1002/chem.201801389.

[30] A. Vyšniauskas and M. K. Kuimova. A twisted tale: measuring viscosity and temperature of microenvironments using molecular

rotors. *International Reviews in Physical Chemistry*, 37:259–285, 2018. doi: 10.1080/0144235X.2018.1510461.

[31] A. S. Klymchenko. Fluorescent probes for lipid membranes: From the cell surface to organelles. *Accounts of Chemical Research*, 56: 1–12, 2023. doi: 10.1021/acs.accounts.2c00586.

[32] M. Paez-Perez and M. K. Kuimova. Fluorescence microscopy: A concise guide to current imaging methods. *Angewandte Chemie International Edition*, 63:e202311233, 2023. doi: 10.1002/anie.202311233.

[33] S. Ye, H. Zhang, J. Fei, C. H. Wolstenholme, and X. Zhang. A general strategy to control viscosity sensitivity of molecular rotor-based fluorophores. *Angewandte Chemie*, 60:1339–1346, 2020. doi: 10.1002/anie.202011108.

[34] R. Žvirblis, K. Maleckaitė, J. Dodonova-Vaitkūnienė, D. Jurgutis, R. Žilėnaitė, V. Karabanovas, S. Tumkevičius, and A. Vyšniauskas. A red-emitting thiophene-modified bodipy probe for fluorescence lifetime-based polarity imaging of lipid droplets in living cells. *Journal of Materials Chemistry B*, 11:3919–3928, 2023. doi: 10.1039/D3TB00305A.

[35] M. K. Kuimova, G. Yahioglu, J. A. Levitt, and K. Suhling. Molecular rotor measures viscosity of live cells via fluorescence lifetime imaging. *Journal of the American Chemical Society*, 130:6672–6673, 2008. doi: 10.1021/ja800570d.

[36] K. Y. Law. Fluorescence probe for microenvironments: anomalous viscosity dependence of the fluorescence quantum yield of p-n,n-dialkylaminobenzylidenemalononitrile in 1-alkanols. *Chemical Physics Letters*, 75:545–549, 1980. doi: 10.1016/0009-2614(80)80574-4.

[37] M. K. Kuimova. Mapping viscosity in cells using molecular rotors. *Physical Chemistry Chemical Physics*, 14:12671–12686, 2012. doi: 10.1039/C2CP41674C.

[38] M. H. Winkler. Some notes on fluorescence intensity. *Biophysical Journal*, 7:719–725, 1967. doi: 10.1016/S0006-3495(67)86618-9.

[39] A. Polita, S. Toliautas, R. Žvirblis, and A. Vyšniauskas. The effect of solvent polarity and macromolecular crowding on the viscosity sensitivity of a molecular rotor bodipy-c10. *Physical Chemistry Chemical Physics*, 22:8296–8303, 2020. doi: 10.1039/C9CP06865A.

[40] R. O. Loutfy and B. A. Arnold. Effect of viscosity and temperature on torsional relaxation of molecular rotors. *The Journal of Physical Chemistry*, 86:4205–4211, 1982. doi: 10.1021/j100218a023.

[41] A. K. Doolittle. Studies in newtonian flow. ii. the dependence of the viscosity of liquids on free-space. *Journal of Applied Physics*, 22: 1471–1475, 1951. doi: 10.1063/1.1699894.

[42] G. Mauviel and E. Favre. Free-volume theory applied to diffusion in liquids: A critical analysis. *Industrial & Engineering Chemistry Research*, 43:6847–6854, 2004. doi: 10.1021/ie049719w.

[43] S. Howell, M. Dakanali, E. A Theodorakis, and M. A. Haidekker. Intrinsic and extrinsic temperature-dependency of viscosity-sensitive fluorescent molecular rotors. *Journal of Fluorescence*, 22: 457–465, 2011. doi: 10.1007/s10895-011-0979-z.

[44] S. Toliautas, J. Dodonova, A. Žvirblis, I. Čiplys, A. Polita, A. Devižis, S. Tumkevičius, J. Šulskus, and A. Vyšniauskas. Enhancing the viscosity-sensitive range of a bodipy molecular rotor by two orders of magnitude. *Chemistry–A European Journal*, 25: 10342–10349, 2019. doi: 10.1002/chem.201901315.

[45] F. Zhou, J. Shao, Y. Yang, J. Zhao, H. Guo, X. Li ans S. Ji, and Z. Zhang. Molecular rotors as fluorescent viscosity sensors: Molecular design, polarity sensitivity, dipole moments changes, screening solvents, and deactivation channel of the excited states. *European Journal of Organic Chemistry*, 2011:4773–4787, 2011. doi: 10.1002/ejoc.201100606.

[46] T. Suhina, S. Amirjalayer, B. Mennucci, S. Woutersen, M. Hilbers, D. Bonn, and A. M. Brouwer. Excited-state decay pathways of molecular rotors: Twisted intermediate or conical intersection? *The Journal of Physical Chemistry Letters*, 21:4285–4290, 2016. doi: 10.1021/acs.jpclett.6b02277.

[47] T. Förster and G. Hoffmann. Effect of viscosity on the fluorescence quantum yield of some dye systems. *Zeitschrift fur physikalische chemie*, 75:63–76, 1971.

[48] M. A. Haidekker and E. A. Theodorakis. Environment-sensitive behavior of fluorescent molecular rotors. *Journal of Biological Engineering*, 4:11, 2010. doi: 10.1186/1754-1611-4-11.

[49] Y. Karibjanova, I. Rodriguez-Ruiz, A. Orte, J. A. Gavira, P. Roblin, and S. Teychené. Fluorescence lifetime measurements of molecular rotors for protein solubility prediction through non-specific interactions characterization. *Journal of Molecular Liquids*, 415: 126350, 2024. doi: 10.1016/j.molliq.2024.126350.

[50] L. E. Shimolina, M. A. Izquierdo, I. López-Duarte, J. A. Bull, M. V. Shirmanova, L. G. Klapshina, E. V. Zagaynova, and M. K. Kuimova. Imaging tumor microscopic viscosity in vivo using molecular rotors. *Scientific Reports*, 7:41097, 2017. doi: 10.1038/srep41097.

[51] A. Prlj, L. Vannay, and C. Corminboeuf. Fluorescence quenching in bodipy dyes: The role of intramolecular interactions and charge transfer. *Helvetica*, 100:e1700093, 2017. doi: 10.1002/hlca.201700093.

[52] J. R. Lakowicz and G. Weber. Quenching of fluorescence by oxygen. probe for structural fluctuations in macromolecules. *Biochemistry*, 12:4161–4170, 1973. doi: 10.1021/bi00745a020.

[53] M. Kasha. Collisional perturbation of spin-orbital coupling and the mechanism of fluorescence quenching. a visual demonstration of the perturbation. *Journal of Chemical Physics*, 20:71–74, 1952. doi: 10.1063/1.1700199.

[54] A. Vyšniauskas, I. López-Duarte, N. Duchemin, T.-T. Vu, Y. Wu, E. M. Budynina, Y. A. Volkova, E. P. Cabrera, D. E. Ramírez-Ornelas, and M. K. Kuimova. Exploring viscosity, polarity and temperature sensitivity of bodipy-based molecular rotors. *Physical Chemistry Chemical Physics*, 19:25252–25259, 2017. doi: 10.1039/c7cp03571c.

[55] K. Maleckaitė, D. Narkevičius, R. Žilėnaitė, J. Dodonova-Vaitkūnienė, S. Toliautas, S. Tumkevičius, and A. Vyšniauskas. Give or take: Effects of electron-accepting/-withdrawing groups in red-fluorescent bodipy molecular rotors. *Molecules*, 27:23, 2022. doi: 10.3390/molecules27010023.

[56] M. A. Haidekker, T. P. Brady, D. Lichlyter, and E. A. Theodorakis. Effects of solvent polarity and solvent viscosity on the fluorescent properties of molecular rotors and related probes. *Bioorganic Chemistry*, 33:415–425, 2005. doi: 10.1016/j.bioorg.2005.07.005.

[57] V. I. Stsiapura, S. A. Kurhuzenkau, V. A. Kuzmitsky, O. V. Bouganov, and S. A. Tikhomirov. Solvent polarity effect on nonradiative decay rate of thioflavin t. *The Journal of Physical Chemistry A*, 120:5481–5496, 2016. doi: 10.1021/acs.jpca.6b02577.

[58] M. A. Haidekker and E. A. Theodorakis. Molecular rotors–fluorescent biosensors for viscosity and flow. *Organic & Biomolecular Chemistry*, 5:1669–1678, 2007. doi: 10.1039/B618415D.

[59] A. H. Ashoka, P. Ashokkumar, Y. P. Kovtun, and A. S. Klymchenko. Solvatochromic near-infrared probe for polarity mapping of biomembranes and lipid droplets in cells under stress. *The Journal of Physical Chemistry Letters*, 10:2414–2421, 2019. doi: 10.1021/acs.jpclett.9b00668.

[60] M. A. Haidekker, T. P. Brady, D. Lichlyter, and E. A. Theodorakis. A ratiometric fluorescent viscosity sensor. *Journal of the American Chemical Society*, 128:398–399, 2006. doi: 10.1021/ja056370a.

[61] A. Vyšniauskas, D. Ding, M. Qurashi, I. Boczarow, M. Balaz, H. L. Anderson, and M. K. Kuimova. Tuning the sensitivity of fluorescent porphyrin dimers to viscosity and temperature. *Chemistry – A European Journal*, 23(4):11001–11010, 2017. doi: 10.1002/chem.201700740.

[62] N. A. Hosny, G. Mohamedi, P. Rademeyer, J. Owen, Y. Wu, M.-X.

Tang, R. J. Eckersley, E. Stride, and M. K. Kuimova. Mapping microbubble viscosity using fluorescence lifetime imaging of molecular rotors. *Proceedings of the National Academy of Sciences USA*, 110:9225–9230, 2013. doi: 10.1073/pnas.1301479110.

[63] V. I. Stsiapura, A. A. Maskevich, V. A. Kuzmitsky, V. N. Uversky, I. M. Kuznetsova, and K. K. Turoverov. Thioflavin t as a molecular rotor: Fluorescent properties of thioflavin t in solvents with different viscosity. *The Journal of Physical Chemistry B*, 112:15893–15902, 2008. doi: 10.1021/jp805822c.

[64] K. Daus, S. Tharamak, W. Pluempanupat, P. A. Galie, M. A. Theodoraki, E. A. Theodorakis, and M. L. Alpaugh. Fluorescent molecular rotors as versatile in situ sensors for protein quantitation. *Scientific Reports*, 13:20529, 2023. doi: 10.1038/s41598-023-46571-5.

[65] A. Briole, T. Podgorski, and B. Abou. Thioflavin t as a molecular rotor: Fluorescent properties of thioflavin t in solvents with different viscosity. *Soft Matter*, 17:4525–4537, 2021. doi: 10.1039/D1SM00321F.

[66] M. E. Nipper, M. Dakanali, E. Theodorakis, and M. A Haidekker. Detection of liposome membrane viscosity perturbations with ratiometric molecular rotors. *Biochimie*, 93:988–994, 2011. doi: 10.1016/j.biochi.2011.02.002.

[67] M. K. Kuimova, S. W. Botchway, A. W. Parker, M. Balaz, H. A. Collins, H. L. Anderson, K. Suhling, and P. R. Ogilby. Imaging intracellular viscosity of a single cell during photoinduced cell death. *Nature Chemistry*, 1:69–73, 2009. doi: 10.1038/nchem.120.

[68] M. A. Izquierdo, A. Vyšniauskas, S. A. Lermontova, I. S. Grigoryev, N. Y. Shilyagina, I. V. Balalaeva, L. G. Klapshina, and M. K. Kuimova. Dual use of porphyrazines as sensitizers and viscosity markers in photodynamic therapy. *Journal of Materials Chemistry B*, 3:1089–1096, 2015. doi: 10.1038/nchem.120.

[69] I. López-Duarte, T. T. Vu, M. A. Izquierdo, J. A. Bull, and M. K. Kuimova. A molecular rotor for measuring viscosity in plasma membranes of live cells. *Chemical Communications*, 50:5282–5284, 2014. doi: 10.1039/c3cc47530a.

[70] Y. Liu, B. Guo, X. Zhang, and J. Jing. Fluorescence intensity and lifetime imaging of a viscosity sensitive zwitterionic amphiphile for cell membrane tension and apoptosis bodies. *Sensors and Actuators B: Chemical*, 432:137474, 2025. doi: 10.1016/j.snb.2025.137474.

[71] S.-C. Lee, J. Heo, J.-W. Ryu, C.-L. Lee, S. Kim, J.-S. Tae, B.-O. Rhee, S.-W. Kim, and O.-P. Kwon. Pyrrolic molecular rotors acting as viscosity sensors with high fluorescence contrast. *Chemical*

Communications, 52:13695–13698, 2016. doi: 10.1039/C6CC06521J.

[72] M. Páez-Pérez, I. López-Duarte, A. Vyšniauskas, N. J. Brooks, and M. K. Kuimova. Imaging non-classical mechanical responses of lipid membranes using molecular rotors. *Chemical Science*, 12: 2604–2613, 2021. doi: 10.1039/D0SC05874B.

[73] M. Kubánková, I. López-Duarte, D. Kiryushko, and M. K Kuimova. Molecular rotors report on changes in live cell plasma membrane microviscosity upon interaction with beta-amyloid aggregates. *Soft Matter*, 14:9466–9474, 2018. doi: 10.1039/c8sm01633j.

[74] M. Paez-Perez, A. Vyšniauskas, I. López-Duarte, E. J. Lafarge, R. López-Ríos De Castro, C. M. Marques, A. P. Schroder, P. Muller, C. D. Lorenz, N. J. Brooks, and M. K. Kuimova. Directly imaging emergence of phase separation in peroxidized lipid membranes. *Communications Chemistry*, 6:15, 2023. doi: 10.1038/s42004-022-00809-x.

[75] J. E. Chambers, M. Kubánková, R. G. Huber, I. López-Duarte, E. Avezov, P. J. Bond, S. J. Marciniak, and M. K. Kuimova. An optical technique for mapping microviscosity dynamics in cellular organelles. *ACS Nano*, 12:4398–4407, 2018. doi: 10.1021/acsnano.8b00177.

[76] L. E Shimolina, A. A. Gulin, M. Paez-Perez, I. López-Duarte, I. N. Druzhkova, M. M. Lukina, M. V. Gubina, N. J. Brooks, E. V. Zagaynova, M. K Kuimova, and M. V. Shirmanova. Mapping cisplatin-induced viscosity alterations in cancer cells using molecular rotor and fluorescence lifetime imaging microscopy. *Journal of Biomedical Optics*, 25:126004, 2020. doi: 10.1117/1.JBO.25.12.126004.

[77] X. Qin, X. Yang, L. Du, and M. Li. Polarity-based fluorescence probes: properties and applications. *RSC Medicinal Chemistry*, 12: 1826–1838, 2021. doi: 10.1039/D1MD00170A.

[78] M. C. Gonzalez-Garcia, M. J. Ruedas-Rama, J. A. González-Vera, E. Garcia-Fernandez, and A. Orte. Fluorescent dyes for probing intracellular and subcellular polarity. *Chemistry–Methods*, 6: e202500072, 2025. doi: 10.1002/cmtd.202500072.

[79] C. Reichardt. Solvatochromic dyes as solvent polarity indicators. *Chemical Reviews*, 94:2319–2358, 1994. doi: 10.1021/cr00032a005.

[80] E. Lippert. Spektroskopische bestimmung des dipolmomentes aromatischer verbindungen im ersten angeregten singulettzustand. *Zeitschrift für Elektrochemie, Berichte der Bunsengesellschaft für physikalische Chemie*, 61:962–975, 1957. doi: 10.1002/bbpc.19570610819.

[81] R. Adhikary, C. A. Barnes, and J. W. Petrich. Solvation dynamics of the fluorescent probe prodan in heterogeneous environments:

Contributions from the locally excited and charge-transferred states. *The Journal of Physical Chemistry B*, 113:11999–12004, 2009. doi: 10.1021/jp905139n.

[82] M. Varne, V. Samant, J. A. Mondal, S. K. Nayak, H. N. Ghosh, and D. K. Palit. Ultrafast relaxation dynamics of the excited states of 1-amino- and 1-(n,n-dimethylamino)-fluoren-9-ones. *ChemPhysChem*, 10:2979–2994, 2009. doi: 10.1002/cphc.200900309.

[83] M. E. Vázquez, J. B. Blanco, and B. Imperiali. Photophysics and biological applications of the environment-sensitive fluorophore 6-n,n-dimethylamino-2,3-naphthalimide. *Journal of the American Chemical Society*, 127:1300–1306, 2005. doi: 10.1021/ja0449168.

[84] A. Boruah, F. Abid, P. K. Baruah, and B. K. Rajbongshi. Investigation of the effect of solvent polarity and viscosity on the stokes shift of chromeno[2,3-b]indoles. *Discover Chemistry*, 3:159, 2026. doi: 10.1007/s44371-026-00611-x.

[85] M. M. Lindic, M. Zajonz, M.-L. Hebestreit, M. Schneider, W. L. Meerts, and M. Schmitt. Determination of excited state dipole moments in solution via thermochromic methods. *MethodsX*, 7: 101101, 2020. doi: 10.1016/j.mex.2020.101101.

[86] N. Acar, J. Kurzawa, N. Fritz, A. Stockmann, C. Roman, S. Schneider, and T. Clark. Phenothiazine–pyrene dyads: Photoinduced charge separation and structural relaxation in the ct state. *The Journal of Physical Chemistry A*, 107:9530–9541, 2003. doi: 10.1021/jp036250u.

[87] G. V. Loukova, V. P. Vasiliev, A. A. Milov, V. A. Smirnov, and V. I. Minkin. Unraveling electronic properties of an organometallic solute: Lippert-mataga and quantum-chemical extensive study. *Journal of Photochemistry and Photobiology A: Chemistry*, 327:6–14, 2016. doi: 10.1016/j.jphotochem.2016.04.023.

[88] K. Dimroth, C. Reichardt, T. Siepmann, and F. Bohlmann. Pyridinium n-phenolbetaines and their use for the characterization of the polarity of solvents. *Justus Liebigs Annalen der Chemie*, 661:1, 1963.

[89] F. Shakerizadeh-Shirazi, B. Hemmateenejad, and A. M. Mehranpour. Determination of the empirical solvent polarity parameter et(30) by multivariate image analysis. *Analytical Methods*, 5:891–896, 2013. doi: 10.1039/C2AY26185E.

[90] M. Mohapatra and A. K. Mishra. Photophysical behavior of 8-anilino-1-naphthalenesulfonate in vesicles of pulmonary surfactant dipalmitoylphosphatidylcholine (dppc) and its sensitivity toward the bile salt–vesicle interaction. *Langmuir*, 29:11396–11404, 2013. doi: 10.1021/la402355j.

[91] D. I. Danylchuk, E. Sezgin, P. Chabert, and A. S. Klymchenko.

Redesigning solvatochromic probe laurdan for imaging lipid order selectively in cell plasma membranes. *Analytical Chemistry*, 92: 14798–14805, 2020. doi: 10.1021/acs.analchem.0c03559.

[92] R. Bagdonaite, Z. O. Cinar, R. Zvirblis, J. Dodonova-Vaitkuniene, and A. Polita. Quantitative flim of lipid droplet polarity with a deep-red bodipy probe reveals signatures of ferroptosis resistance. *Chemical & Biomedical Imaging*, 29:11396–11404, 2026. doi: 10.1021/cbmi.5c00193.

[93] A. S. Klymchenko and Y. Mely. Fluorescent environment–sensitive dyes as reporters of biomolecular interactions. *Progress in Molecular Biology and Translational Science*, 113:35–58, 2013. doi: 10.1016/B978-0-12-386932-6.00002-8.

[94] M. Shaikh, J. Mohanty, P. K. Singh, A. C. Bhasikuttan, R. N. Rajule, V. S. Satam, S. R. Bendre, V. R. Kanetkar, and H. Pal. Contrasting solvent polarity effect on the photophysical properties of two newly synthesized aminostyryl dyes in the lower and in the higher solvent polarity regions. *The Journal of Physical Chemistry A*, 114: 4507–4519, 2010. doi: 10.1021/jp9107969.

[95] Z. Zhan, R. Huang, L. Chai, H. Yang, Y. Dai, M. Chen, G. Gu, and Y. Lv. Fluorescence lifetime imaging: A novel approach to simultaneous visualizing lipid droplets and endoplasmic reticulum polarity in live cells and fatty liver. *Sensors and Actuators B: Chemical*, 422:136699, 2025. doi: 10.1016/j.snb.2024.136699.

[96] H. Xiao, P. Li, and B. Tang. Recent progresses in fluorescent probes for detection of polarity. *Coordination Chemistry Reviews*, 427:213582, 2021. doi: 10.1016/j.ccr.2020.213582.

[97] D. I. Danylchuk, P.-H. Jouard, and A. S. Klymchenko. Targeted solvatochromic fluorescent probes for imaging lipid order in organelles under oxidative and mechanical stress. *Journal of the American Chemical Society*, 143:912–924, 2021. doi: 10.1021/jacs.0c10972.

[98] E. Sezgin, F. Schneider, V. Zilles, I. Urbančič, E. Garcia, D. Waithe, A. S. Klymchenko, and C. Eggeling. Polarity-sensitive probes for superresolution stimulated emission depletion microscopy. *Biophysical Journal*, 113:1321–1330, 2017. doi: 10.1016/j.bpj.2017.06.050.

[99] M. Xie, E. H. W. Koch, C. A. van Walree, A. Sobota, A. F. P. Sonnen, E. Breukink, J. A. Killian, and J. H. Lorent. Two separate mechanisms are involved in membrane permeabilization during lipid oxidation. *Biophysical Journal*, 122:4503–4517, 2023. doi: 10.1016/j.bpj.2023.10.028.

[100] M. Sarkar, K. Das, A. Datta, S. Das, and K. Bhattacharyya. Solvation dynamics of coumarin 480 in reverse micelles. slow relaxation of water molecules. *The Journal of Physical Chemistry B*, 100:10523–

10527, 1996. doi: 10.1021/jp953658l.

[101] Y. Wu, H.-M. Wang, X.-L. Hu, Y. Zang, J. Li, H.-H. Han, X.-P. He, S. E. Lewis, H. M. Ismail, and Tony D. James. Twisted intramolecular charge transfer (tict) based fluorescent probes and imaging agents. *Chemical Society Reviews*, 54:12080–12141, 2025. doi: 10.1039/D3CS01118F.

[102] K. Colas, S. Doloczki, A. Kesidou, L. Sainero-Alcolado, A. Rodriguez-Garcia, M. Arsenian-Henriksson, and C. Dyrager. Photophysical characteristics of polarity-sensitive and lipid droplet-specific phenylbenzothiadiazoles. *ChemPhotoChem*, 5:632–643, 2021. doi: 10.1002/cptc.202100040.

[103] S. Sasaki, G. P. C. Drummen, and G. i. Konishi. Recent advances in twisted intramolecular charge transfer (tict) fluorescence and related phenomena in materials chemistry. *Journal of Materials Chemistry C*, 4:2731–2743, 2016. doi: 10.1039/C5TC03933A.

[104] T. Wang, J. Liu, H. Wei, Q. Jiang, T. Yang, X. Zhang, and P. Xing. Developing a polarity-specialized tict fluorescent probe for wash-free and long-term monitoring lipid droplets dynamics. *Talanta*, 294:128191, 2025. doi: 10.1016/j.talanta.2025.128191.

[105] P. Jurkiewicz, L. Cwiklik, P. Jungwirth, and M. Hof. Lipid hydration and mobility: an interplay between fluorescence solvent relaxation experiments and molecular dynamics simulations. *Biochimie*, 94:26–32, 2012. doi: 10.1016/j.biochi.2011.06.027.

[106] D. A. Kelkar and A. Chattopadhyay. Depth-dependent solvent relaxation in reverse micelles: A fluorescence approach. *The Journal of Physical Chemistry B*, 108:12151–12158, 2004. doi: 10.1021/jp048645z.

[107] J. H. Lorent, K. R. Levental, L. Ganesan, G. Rivera-Longsworth, E. Sezgin, M. Doktorova, E. Lyman, and I. Levental. Plasma membranes are asymmetric in lipid unsaturation, packing and protein shape. *Nature Chemical Biology*, 16:644–652, 2020. doi: 10.1038/s41589-020-0529-6.

[108] Z. Darwich, A. S. Klymchenko, O. A. Kucherak, L. Richert, and Y. Mély. Detection of apoptosis through the lipid order of the outer plasma membrane leaflet. *Biochimica et Biophysica Acta (BBA) – Biomembranes*, 1818:3048–3054, 2012. doi: 10.1016/j.bbamem.2012.07.017.

[109] C. Dietrich, L.A. Bagatolli, Z. N. Volovyk, N. L. Thompson, M. Levi, K. Jacobson, and E. Gratton. Lipid rafts reconstituted in model membranes. *Biophysical Journal*, 80:1417–1428, 2001. doi: 10.1016/S0006-3495(01)76114-0.

[110] A. S. Klymchenko and R. Kreder. Fluorescent probes for lipid rafts: From model membranes to living cells. *Chemistry & Biology*,

21:97–113, 2014. doi: 10.1016/j.chembiol.2013.11.009.

[111] R. B. Lira, J. Steinkühler, R. L. Knorr, R. Dimova, and K. A. Riske. Posing for a picture: vesicle immobilization in agarose gel. *Scientific Reports*, 6:25254, 2016. doi: 10.1038/srep25254.

[112] S. C. Warren, A. Margineanu, D. Alibhai, D. J. Kelly, C. Talbot, Y. Alexandrov, I. Munro, M. Katan, C. Dunsby, and P. M. W. French. Rapid global fitting of large fluorescence lifetime imaging microscopy datasets. *PLoS ONE*, 8:e70687, 2013. doi: 10.1371/journal.pone.0070687.

[113] M. R. Dent, I. Lopez Duarte, C. J. Dickson, N. D. Geoghegan, J. M. Cooper, I. R. Gould, R. Krams, J. A. Bull, N. J. Brooks, and M. K. Kuimova. Imaging phase separation in model lipid membranes through the use of bodipy based molecular rotors. *Physical Chemistry Chemical Physics*, 17:18393–18402, 2015. doi: 10.1039/C5CP01937K.

[114] A. Polita, M. Stancikaitė, R. Žvirblis, K. Maleckaitė, J. Dodonova-Vaitkūnienė, S. Tumkevičius, A. P. Shivabalan, and G. Valinčius. Designing a green-emitting viscosity-sensitive 4, 4-difluoro-4-bora-3a, 4a-diaza-s-indacene (bodipy) probe for plasma membrane viscosity imaging. *RSC advances*, 13:19257–19264, 2023. doi: 10.1039/D3RA04126C.

[115] P. Uppamoochikkal, S.Tristram-Nagle, and J. F. Nagle. Orientation of tie-lines in the phase diagram of dopc/dppc/cholesterol model biomembranes. *Langmuir*, 26:17363–17368, 2010. doi: 10.1021/la103024f.

[116] J. H. Davis, J. J. Clair, and J. Juhasz. Phase equilibria in dopc/dppc-d62/cholesterol mixtures. *Biophysical Journal*, 96:521–539, 2009. doi: 10.1016/j.bpj.2008.09.042.

[117] S. L. Veatch and S. L. Keller. Separation of liquid phases in giant vesicles of ternary mixtures of phospholipids and cholesterol. *Biophysical Journal*, 85:3074–3083, 2003. doi: 10.1016/S0006-3495(03)74726-2.

[118] T. Róg, M. Pasenkiewicz-Gierula, I. Vattulainen, and M. Karttunen. Ordering effects of cholesterol and its analogues. *Biochimica et Biophysica Acta (BBA) – Biomembranes*, 1788:97–121, 2009. doi: 10.1016/j.bbamem.2008.08.022.

[119] Z. Li, H. Liu, and X. Luo. Lipid droplet and its implication in cancer progression. *American Journal of Cancer Research*, 10:4112–4122, 2020.

[120] Y. Jin, Y. Tan, J. Wu, and Z. Ren. Lipid droplets: a cellular organelle vital in cancer cells. *Cell Death Discovery*, 9:254, 2023. doi: 10.1038/s41420-023-01493-z.

[121] A. L. S. Cruz, E. de A. Barreto, N. P. B. Fazolini, J. P. B. Viola, and

P. T. Bozza. Lipid droplets: platforms with multiple functions in cancer hallmarks. *Cell Death & Disease*, 11:105, 2020. doi: 10.1038/s41419-020-2297-3.

[122] C. Jin and P. Yuan. Implications of lipid droplets in lung cancer: Associations with drug resistance. *Oncology Letters*, 20:2091–2104, 2020. doi: 10.3892/ol.2020.11769.

[123] A. Polita, R. Žvirblis, J. Dodonova-Vaitkūnienė, A. P. Shivabalan, K. Maleckaitė, and G. Valinčius. Bimodal effects on lipid droplets induced in cancer and non-cancer cells by chemotherapy drugs as revealed with a green-emitting bodipy fluorescent probe. *Journal of Materials Chemistry B*, 12:3022–3030, 2024. doi: 10.1039/D3TB02979D.

[124] S. I. Suarez, C. C. Warner, H. Brown-Harding, A. M. Thooft, B. VanVeller, and J. C. Lukesh III. Highly selective staining and quantification of intracellular lipid droplets with a compact push–pull fluorophore based on benzothiadiazole. *Organic & Biomolecular Chemistry*, 18:495–499, 2020. doi: 10.1039/C9OB02486G.

[125] A. R. Thiam and M. Beller. The why, when and how of lipid droplet diversity. *Journal of Cell Science*, 130:315–324, 2017. doi: 10.1242/jcs.192021.

[126] T. C. Walther, J. Chung, and R. V. Farese Jr. Lipid droplet biogenesis. *Annual Review of Cell and Developmental Biology*, 33:491–510, 2017. doi: 10.1146/annurev-cellbio-100616-060608.

[127] R. Bagdonaitė, R. Žvirblis, J. Dodonova-Vaitkūnienė, and A. Polita. Cancer cell identification via lysosomal membrane microviscosities using a green-emitting bodipy molecular rotor. *JACS Au*, 5: 2004–2014, 2025. doi: 10.1021/jacsau.5c00253.

[128] G. Repetto, A. del Peso, and J. L. Zurita. Neutral red uptake assay for the estimation of cell viability/cytotoxicity. *Nature Protocols*, 3: 1125–1131, 2008. doi: 10.1038/nprot.2008.75.

[129] T. Kurz, J. W. Eaton, and U. T. Brunk. Redox activity within the lysosomal compartment: implications for aging and apoptosis. *Antioxidants & Redox Signaling*, 13:511–523, 2010. doi: 10.1089/ars.2009.3005.

[130] E. Rysman, K. Brusselmans, K. Scheys, L. Timmermans, R. Derua, S. Munck, P. P. Van Veldhoven, D. Waltregny, V. W. Daniëls, J. Machiels, F. Vanderhoydonc, K. Smans, E. Waelkens, G. Verhoeven, and J. V. Swinnen. De novo lipogenesis protects cancer cells from free radicals and chemotherapeutics by promoting membrane lipid saturation. *Cancer Research*, 70:8117–8126, 2010. doi: 10.1158/0008-5472.CAN-09-3871.

[131] T. J. Sargeant, B. Lloyd-Lewis, H. K. Resemann, A. Ramos-Montoya, J. Skepper, and C. J. Watson. Stat3 controls cell death

during mammary gland involution by regulating uptake of milk fat globules and lysosomal membrane permeabilization. *Nature Cell Biology*, 16:1057–1068, 2014. doi: 10.1038/ncb3043.

[132] A. Vyšniauskas, M. Qurashi, and M. K. Kuimova. A molecular rotor that measures dynamic changes of lipid bilayer viscosity caused by oxidative stress. *Chemistry – A European Journal*, 22: 13210–13217, 2016. doi: 10.1002/chem.201601925.

[133] T. Iulianna, N. Kuldeep, and F. Eric. The achilles' heel of cancer: targeting tumors via lysosome-induced immunogenic cell death. *Cell Death & Disease*, 13:509, 2022. doi: 10.1038/s41419-022-04912-8.

[134] Marie Stampe Ostenfeld, Nicole Fehrenbacher, Maria Høyer-Hansen, Christian Thomsen, Thomas Farkas, and Marja Jäättelä. Effective tumor cell death by σ-2 receptor ligand siramesine involves lysosomal leakage and oxidative stress. *Cancer Research*, 65: 8975–8983, 2005. doi: 10.1158/0008-5472.CAN-05-0269.

[135] A. Anand, B. Liu, J. D. Giacobini, K. Maeda, M. Rohde, and M. Jäättelä. Targeting lysosomes in human disease: from basic research to clinical applications. *Molecular Cancer Therapeutics*, 18:1602–1614, 2019. doi: 10.1158/1535-7163.MCT-18-1406.

[136] L. Groth-Pedersen and M. Jäättelä. Combating apoptosis and multidrug resistant cancers by targeting lysosomes. *Cancer Letters*, 332:265–274, 2013. doi: 10.1016/j.canlet.2010.05.021.

[137] S. Aits, M. Jäättelä, and J. Nylandsted. Methods for the quantification of lysosomal membrane permeabilization: A hallmark of lysosomal cell death. *Methods in Cell Biology*, 126:261–285, 2015. doi: 10.1016/bs.mcb.2014.10.032.

[138] I. H. Mir and C. Thirunavukkarasu. The relevance of acid sphingomyelinase as a potential target for therapeutic intervention in hepatic disorders: current scenario and anticipated trends. *Archives of Toxicology*, 97:2069–2087, 2023. doi: 10.1007/s00204-023-03529-w.

[139] H. Lee, A. Horbath, L. Kondiparthi, J. K. Meena, G. Lei, S. Dasgupta, X. Liu, L. Zhuang, P. Koppula, M. Li, I. Mahmud, B. Wei, P. L. Lorenzi, K. Keyomarsi, M. V. Poyurovsky, K. Olszewski, and B. Gan. Cell cycle arrest induces lipid droplet formation and confers ferroptosis resistance. *Nature Communications*, 15:79, 2024. doi: 10.1038/s41467-023-44412-7.

[140] Z. Lin, J. Liu, R. Kang, M. Yang, and D. Tang. Lipid metabolism in ferroptosis. *Advanced Biology*, 5:2100396, 2021. doi: 10.1002/adbi.202100396.

[141] D. Liang, A. M. Minikes, and X. Jiang. Ferroptosis at the intersection of lipid metabolism and cellular signaling. *Molecular Cell*, 82:

2215–2227, 2022. doi: 10.1016/j.molcel.2022.03.022.

[142] S. J. Dixon and J. A. Olzmann. The cell biology of ferroptosis. *Nature Reviews Molecular Cell Biology*, 25:424–442, 2024. doi: 10.1038/s41580-024-00703-5.

[143] K. Maleckaitė, J. Dodonova, S. Toliautas, R. Žilėnaitė, D. Jurgutis, V. Karabanovas, S. Tumkevičius, and A. Vyšniauskas. Designing a red-emitting viscosity-sensitive bodipy fluorophore for intracellular viscosity imaging. *Chemistry – A European Journal*, 27: 16768–16775, 2021. doi: 10.1002/chem.202102743.

[144] A. Cui, X. Peng, J. Fan, X. Chen, Y. Wu, and B. Guo. Synthesis, spectral properties and photostability of novel boron–dipyrromethene dyes. *Journal of Photochemistry and Photobiology A: Chemistry*, 186: 997–1003, 2007. doi: 10.1016/j.jphotochem.2006.07.015.

[145] K. Wang, S. Ma, Y. Ma, Z. Zhao, M. Xing, L. Zhou, D. Cao, and W. Lin. Aurone derivative revealing the metabolism of lipid droplets and monitoring oxidative stress in living cells. *Analytical Chemistry*, 92:6631–6636, 2020. doi: 10.1021/acs.analchem.0c00456.

[146] J. Wong-ekkabut, Z. Xu, W. Triampo, I.-M. Tang, D. P. Tieleman, and L. Monticelli. Effect of lipid peroxidation on the properties of lipid bilayers: A molecular dynamics study. *Biophysical Journal*, 93:4225–4236, 2007. doi: 10.1529/biophysj.107.112565.

[147] G. M'Baye, Y. Mély, G. Duportail, and A. S. Klymchenko. Liquid ordered and gel phases of lipid bilayers: Fluorescent probes reveal close fluidity but different hydration. *Biophysical Journal*, 95:1217–1225, 2008. doi: 10.1529/biophysj.107.127480.

[148] J. Mahamid, D. Tegunov, A. Maiser, J. Arnold, H. Leonhardt, J. M. Plitzko, and W. Baumeister. Liquid ordered and gel phases of lipid bilayers: Fluorescent probes reveal close fluidity but different hydration. *Proceedings of the National Academy of Sciences USA*, 116: 16866–16871, 2019. doi: 10.1073/pnas.1903642116.

Santrauka (Summary in Lithuanian)

Šiame darbe pristatomas fluorescencijos gyvavimo trukme pagrįstų molekulinių jutiklių kūrimas ir taikymas kiekybiniam fizikinių savybių vaizdinimui gyvų ląstelių lipidinėse struktūrose. Darbo metu, *BODIPY* architektūros pagrindu buvo sukurti mikroklampos jutikliai, pasižymintys specifiškumu plazminei membranai, lizosomoms bei lipidiniams lašeliams. Šie jutikliai pasižymėjo stipria fluorescencijos gyvavimo trukmės priklausomybe nuo aplinkos klampos ir minimaliu jautrumu terpės poliškumui.

Šie mikroklampos jutikliai buvo pritaikyti membranų mikroklampos tyrimams vėžinėse bei nevėžinėse ląstelėse mikroklampos pokyčiams įvertinti ląstelinių perturbacijų metu. Tyrimų metu nustatyti reikšmingi mikroklampos skirtumai tarp vėžinių ir nevėžinių ląstelių lizosomų bei lipidinių lašelių. Taip pat pademonstruoti skirtingi mikroklampos atsakai į chemoterapeutinius vaistus, demonstruojantys, kad lipidinių struktūrų mikroklampa yra jautrus ląstelinės būsenos indikatorius. Organelėms specifiški jutikliai papildomai atskleidė mikroklampos heterogeniškumą lipidiniuose lašeliuose.

Šio darbo apimtis buvo išplėsta sukuriant poliškumui jautrų BODIPY jutiklį lipidiniams lašeliams, leidžiantį kiekybiškai įvertinti poliškumo pokyčius nepriklausomai nuo lipidinių struktūrų mikroklampos. Naudojant šį jutiklį buvo parodyta, kad lipidinių lašelių poliškumas ankstyvos feroptozės metu didėja dėl lipidų peroksidacijos ir mažėja vystantis atsparumui.

Apibendrinant, šiame darbe atlikti fluorescencijos gyvavimo trukme pagrįsti mikroklampos ir poliškumo matavimai parodė, kad skirtingi ląstelių fenotipai bei patologiniai procesai gali būti identifikuojamos pagal lipidų struktūros pokyčius bei aplinkai jautrių jutiklių pritaikomumą

tiriant biofizikinius procesus.

Tikslas

Šio darbo tikslas – sukurti fluorescencijos gyvavimo trukme pagrįstus molekulinius jutiklius, skirtus ląstelinių lipidinių struktūrų fizikinių savybių kiekybiniam vaizdinimui bei pritaikyti šiuos jutiklius tiriant mikroklampos ir poliškumo pokyčius gyvose ląstelėse fiziologinėmis bei streso sąlygomis.

Uždaviniai

- Sukurti dideliu jautrumu bei minimaliais fotofizikiniais artefaktais pasižyminčius fluorescencijos gyvavimo trukme pagrįstus molekulinius rotorius bei poliškumo jutiklius, skirtus gyvų ląstelių vaizdinimui.
- Ištirti jutiklių fotofizikines savybes tirpaluose ir modelinėse lipidinėse sistemose, įskaitant jų jautrumą klampai bei poliškumui, taikant nuostovius ir nuo laiko priklausomus fluorescencijos matavimus bei nustatyti kiekybinius sąryšius tarp fluorescencijos gyvavimo trukmės ir aplinkos parametrų.
- Parodyti jutiklių pritaikomumą vaizdinant modelines lipidines sistemas bei gyvas ląsteles.
- Pagrįsti aplinkos matavimų biologinę reikšmę tiriant, kaip mikroklampos ir poliškumo pokyčiai atspindi ląstelinę būseną bei su ligomis susijusius procesus.

Darbo aktualumas

Dinaminės ląstelių lipidinių struktūrų biofizikinės savybės, tokios kaip mikroklampa ir poliškumas, atlieka esminį vaidmenį biologinių membranų organizacijoje. Tačiau kiekybiniai mikroklampos bei poliškumo matavimai gyvose ląstelėse išlieka sudėtingi dėl tinkamų jutiklių, pasižyminčių aukštu jautrumu, specifiškumu bei aiškiais optiniais signalais, trūkumo.

Šiame darbe šie apribojimai sprendžiami kuriant ir taikant fluorescencijos gyvavimo trukme pagrįstus molekulinius rotorius bei poliškumo jutiklius, pritaikytus matavimams gyvose ląstelėse. Ypatingas dėmesys skirtas įprastų fotofizikinių artefaktų, pavyzdžiui, kryžminio jautrio poliškumui ir klampai, minimizavimui bei patikimų duomenų gavimui heterogeniškose lipidinėse aplinkose.

Nors organelėms specifinių jutiklių kūrimas pats savaime nėra nauja sritis, šioje disertacijoje pateikiama keletas esminių jutiklių dizaino ir jų taikymo patobulinimų. Darbo metu buvo sukurtas fluorescencijos gyvavimo trukme pagrįstas poliškumo jutiklis, pasižymintis raudona emisijos juosta bei leidžiantis kiekybiškai vaizdinti lipidinių lašelių poliškumą. Be to, parodyta, kad jutiklių nukreipimą į lipidinius lašelius lemia ne tik jutiklio hidrofobiškumas, bet ir jutiklio molekulinė geometrija: neplokštuminės, nepolinės struktūros pasižymi didesniu afinitetu izotropinėms lipidinėms aplinkoms.

Šiame darbe sukurti jutikliai buvo pritaikyti biologiškai reikšmingiems procesams tirti gyvose ląstelėse. Tai apima lipidinių lašelių mikroklampos pokyčius veikiant ląsteles chemoterapiniais vaistais, lizosomų membranų mikroklampos pokyčius veikiant ląsteles katijoniniais amfifiliniais vaistais bei poliškumo pokyčius, susijusius su lipidų peroksidacija feroptozės metu ir išsivystant atsparumui šiam procesui.

Apibendrinant, šis darbas parodo, kad fluorescencijos gyvavimo trukme pagrįsti mikroklampos ir poliškumo matavimai suteikia kiekybinę informaciją apie ląstelinę būseną bei su ligomis susijusius procesus. Integruojant jutiklių kūrimą, fotofizikinę charakterizaciją bei ląstelinį vaizdinimą, šioje disertacijoje parodoma, kad lipidinių struktūrų fizikinių savybių matavimai gali aprašyti ląstelinę būseną.

Ginamieji teiginiai

- Mikroklampos pokyčiai ląstelinėse organelėse atspindi fiziologines ir patologines ląstelių būsenas, įgalindami nustatyti su ligomis susijusius pokyčius bei vaistų sukeltą poveikį.
- Neplokštuminė molekulių geometrija skatina fluorescencinių jutiklių įsiterpimą į izotropines lipidines aplinkas.
- Fluorescencija pagrįstas poliškumo vaizdinimas leidžia kiekybiškai įvertinti lipidų peroksidaciją.

Pagrindiniai rezultatai

Žaliai fluorescuojančio, klampai jautraus BODIPY jutiklio kūrimas plazminės membranos mikroklampos vaizdinimui

Šio darbo tikslas – sukurti klampumui jautrų BODIPY fluorescencinį jutiklį, skirtą kiekybiniam plazminių membranų mikroklampos vaizdinimui. Siekiant įveikti įprastų fluorescencinių jutiklių trūkumus, BODIPY architektūros pagrindu sukonstruotas tirpus vandenyje, selektyvus plazminėms membranoms bei nejautrus poliškumo efektams molekulinis rotorius *(BODIPY-PM)*.

Jutiklio fotofizikinės savybės ištirtos skirtingos klampos bei poliškumo tirpaluose, nustatant stiprią fluorescencijos gyvavimo trukmės priklausomybę nuo klampos ir mažą jautrumą tirpiklio poliškumui. Fluorescencijos gyvavimo trukmės vaizdinimo mikroskopija (FLIM) pritaikyta jutiklio įvertinimui modelinėse bei gyvų ląstelių membranose.

Jutiklis efektyviai įsiskverbė tiek į modelines membranas, tiek į plazmines membranas ir tolygiai pasiskirstė tiek tvarkiosiose, tiek netvarkiosiose lipidinėse fazėse, leisdamas patikimai vizualizuoti membranos heterogeniškumą.

Chemoterapinių vaistų sukeliamas bimodalinis poveikis lipidiniams lašeliams vėžinėse ir nevėžinėse ląstelėse, nustatytas naudojant žaliai fluorescuojantį BODIPY jutiklį

Darbe siekta sukurti į lipidinius lašelius nukreiptą BODIPY jutiklį kiekybiniams mikroklampos tyrimams gyvose ląstelėse. Sukonstruotas žaliai fluorescuojantis molekulinis rotorius *(BODIPY-LD)*, pasižymintis stipriu fluorescencijos gyvavimo trukmės jautrumu klampai ir mažu jautrumu tirpiklio poliškumui.

Naudojant FLIM, parodyta, kad jutiklis selektyviai žymi lipidinius lašelius gyvose ląstelėse. Tyrimai modelinėse lipidinėse sistemose patvirtino gebėjimą atskirti skirtingas lipidų fazes. Eksperimentai su gyvomis ląstelėmis atskleidė, kad vėžinės A549 ląstelės pasižymi didesniu lipidinių lašelių skaičiumi ir platesniu jų mikroklampos pasiskirstymu nei nevėžinės HEK 293T ląstelės, parodydami, kad lipidinių lašelių mikroklampa suteikia papildomos informacijos, kurios neatskleidžia vien organelių gausa.

Be to, kiekybiškai įvertintas chemoterapinių vaistų doksorubicino ir etopozido poveikis lipidinių lašelių mikroklampai. Šie vaistai sukėlė specifinius, nuo ląstelių linijos priklausančius pokyčius, ypač chemoterapijai atspariose ląstelėse. Rezultatai rodo, kad lipidų lašelių mikroklampa yra dinamiškai reguliuojama ir gali būti taikoma kaip jautrus ląstelinės būsenos bei atsako į vaistus indikatorius.

Vėžinių ląstelių atpažinimas pagal lizosomų membranų mikroklampą naudojant žaliai fluorescuojantį BODIPY molekulinį rotorių

Šiuo darbu siekta sukurti į lizosomų membranas nukreiptą molekulinį rotorių ir įvertinti lizosomų membranas kaip galimą ląstelinės būsenos žymenį. Sukurtas BODIPY jutiklis *(BODIPY-Lys)*, kurio fluorescencijos gyvavimo trukmė stipriai priklauso nuo tirpiklio klampos, tačiau beveik nepriklauso nuo tirpiklio poliškumo ir aplinkos temperatūros.

FLIM tyrimai parodė, kad jutiklis selektyviai kaupiasi gyvų ląstelių lizosomų membranose. Modelinėse lipidinėse sistemose patvirtintas jutiklio gebėjimas atpažinti cholesterolio sukeltus membranų tvarkos pokyčius.

Nustatyta, kad vėžinių ląstelių lizosomų membranų mikroklampa yra reikšmingai didesnė nei nevėžinių ląstelių, todėl šis parametras gali būti naudojamas piktybinių ir nepiktybinių ląstelių atskyrimui pagal membranų organizaciją. Kationiniai amfifiliniai vaistai sukėlė priešingus lizosomų membranų mikroklampos pokyčius, nors abu indukavo lizosomų membranų pralaidumo padidėjimą, rodydami, kad lizosomų membranų pažaida gali būti pasiekiama skirtingais mechanizmais. Šis tyrimas parodo, kad lizosomų mikroklampa gali būti funkcinis biožymuo vėžinėms ląstelėms identifikuoti.

Kiekybinis lipidinių lašelių poliškumo FLIM vaizdinimas BODIPY jutikliu atskleidžia atsparumo feroptozei biofizikinius požymius

Darbe siekta sukurti poliškumui jautrų jutiklį lipidinių lašelių vaizdinimui gyvose ląstelėse. Sukonstruotas raudonai fluorescuojantis BODIPY jutiklis *(BP-Ph-LD)*, kurio fluorescencijos gyvavimo trukmė stipriai priklauso nuo aplinkos poliškumo, bet pasižymi minimaliu jautrumu

klampos ar temperatūros pokyčiams. Tyrime pademonstruota, kad poliškumo parametras gali būti naudojamas kiekybiškai įvertinti lipidų peroksidų koncentraciją lipidinėse sistemose. Taip pat nustatyta, kad neplokščia jutiklio molekulinė struktūra, kartu su jo hidrofobiškumu, yra svarbus veiksnys, lemiantis dažų nukreipimą į izotropines aplinkas (lipidinius lašelius). Tai rodo, kad jutiklio stereochemija yra nepakankamai įvertintas, tačiau svarbus veiksnys, lemiantis selektyvų lipidinių lašelių žymėjimą.

Naudojant FLIM, jutiklis leido kiekybiškai išmatuoti lipidinių lašelių poliškumą gyvose ląstelėse. Krūties vėžio ląstelėse (MDA-MB-231), paveiktose feroptozę skatinančiu junginiu erastinu, pastebėti dinamiški poliškumo pokyčiai ankstyvosiose ir vėlyvosiose feroptozės stadijose.

Feroptozei atsparios ląstelės pasižymėjo sumažėjusiu lipidinių lašelių poliškumu, pakitusia jų morfologija ir skirtingų poliškumo populiacijų erdviniu atsiskyrimu, todėl šie požymiai gali būti laikomi biofizikiniais atsparumo feroptozei žymenimis. Tyrimas parodė, kad lipidinių lašelių poliškumas gali būti naudojamas kaip biofizikinis parametras, leidžiantis atskirti feroptozei atsparias ląsteles.

Išvados

Šiame darbe pristatomas fluorescencijos gyvavimo trukme pagrįstų molekulinių jutiklių kūrimas ir taikymas kiekybiniam lipidinių mikroaplinkų apibūdinimui gyvose ląstelėse. Buvo sukurta BODIPY pagrindu veikiančių molekulinių rotorių serija, leidžianti atlikti organelėms specifinius mikroklampos matavimus plazminėse membranose, lipidiniuose lašeliuose ir lizosomose, taip pademonstruojant FLIM kaip kiekybinį metodą lokalioms membranų savybėms tirti sudėtingose biologinėse sistemose.

Šie jutikliai buvo pritaikyti tirti, kaip membranų mikroklampa kinta priklausomai nuo ląstelės būsenos ir reaguojant į cheminius poveikius. Nustatyta, kad vėžinių ląstelių lizosomų membranos pasižymi didesne mikroklampa nei nevėžinių ląstelių, o lipidinių lašelių mikroklampa suteikia papildomos informacijos apie ląstelių fenotipą, kurios neatskleidžia vien lipidinių lašelių gausa.

Šio metodo taikymo galimybės buvo išplėstos sukuriant poliškumui jautrų jutiklį lipidiniams lašeliams, leidžiantį kiekybiškai tirti poliškumą nepriklausomai nuo membranos mikroklampos. Nustatyta, kad

lipidinių lašelių poliškumas didėja feroptozės metu dėl lipidų peroksidacijos ir mažėja vystantis atsparumui feroptozei, kartu atsirandant būdingiems lipidinių lašelių morfologijos ir erdvinio pasiskirstymo pokyčiams.

Be to, šiame darbe pateikiamos įžvalgos apie jutiklių dizainą, parodant, kad jutiklių nukreipimui į lipidinius lašelius daro įtaką ne tik jutiklio hidrofobiškumas, bet ir molekulinė geometrija – neplokščios struktūros linkusios selektyviai pasiskirstyti izotropinėse lipidinėse aplinkose.

Apibendrinant, šiame darbe fluorescencijos gyvavimo trukme pagrįsti mikroklampos ir poliškumo matavimai pademonstruoja fluorescencinių aplinkai jautrių jutiklių pritaikomumą tiriant ląstelines būsenas, patologinius procesus bei ląstelinės adaptacijos mechanizmus.

Curriculum Vitae

Artūras Polita graduated from Vilnius University with a Master's degree in Chemistry. During his bachelor's studies, he became involved in research focused on the development and photophysical characterization of fluorescent probes, particularly BODIPY-based compounds. This research direction continued throughout his master's and doctoral studies, where his work focused on the design and application of fluorescent probes for investigating lipid microenvironments using fluorescence lifetime imaging methods.

During his doctoral studies, Artūras was awarded several competitive scholarships, including the *Vilnius University Life Sciences Center Named Scholarship* (2023, 2024), the *Linea Libera Scholarship* (2024), and the *Research Council of Lithuania Scholarship for Academic Performance* (2025). He has published more than nine scientific articles in peer-reviewed international journals and presented his work at multiple national and international scientific conferences. His research interests include fluorescent probe design, the photophysics of molecular rotors, and fluorescence lifetime imaging microscopy.

Acknowledgements

I am grateful to my supervisor, Dr. Gintaras Valinčius, for his guidance, continuous support, and insightful discussions throughout the course of this research. His encouragement has been fundamental to my development and to the completion of this thesis.

I am grateful to Dr. Jelena Dodonova-Vaitkūnienė and Rokas Žvirblis for the synthesis of the BODIPY probes used throughout this work. Their expertise in organic synthesis was essential for enabling the experimental studies presented in this thesis.

I would also like to acknowledge Dr. M. K. Kuimova (Imperial College London) and Dr. A. S. Klymchenko (French National Centre for Scientific Research) for their influential contributions to the field and personal correspondences, which have significantly inspired the design and conceptual development of the probes explored in this work.

I am very grateful to the Center for Physical Sciences and Technology, Department of Molecular Compound Physics, for providing access to TCSPC equipment and pulsed excitation sources, which were essential for the fluorescence lifetime measurements performed in this work.

Finally, I thank my close colleagues at the Vilnius University for their support, discussions, and collaborative environment during the course of this research (Dr. Rimgailė Tamulytė, Evelina Jankaitytė, Modestas Mažerimas, Rūta Bagdonaitė, Zeynep Ozlem Cinar).

Artūras Polita
Vilnius
3rd August 2026

Conference Presentations

Oral Presentations

- A. Polita, Mapping viscosities of lipid bilayers in live cells and model membranes through FLIM, *The Coins*, Vilnius (Lithuania), 2023.
- A. Polita, Mapping viscosities of lipid bilayers in live cells and model membranes through FLIM, *Open Readings*, Vilnius (Lithuania), 2023.
- A. Polita, Development of fluorescent viscosity probes for disease identification, *Bioateitis*, Vilnius (Lithuania), 2024.
- A. Polita, Fluorescent viscosity probes as diagnostic tools for cancer detection, *The Coins*, Vilnius (Lithuania), 2024.
- A. Polita, Development of fluorescent viscosity probes for disease identification, *FizTeCh*, Vilnius (Lithuania), 2024.
- A. Polita, Fluorescent viscosity probes as diagnostic tools for cancer detection, *Open Readings*, Vilnius (Lithuania), 2024.

Poster Presentations

- A. Polita, Revealing lipid order differences between cancerous and non-cancerous cells using fluorescent viscosity probes, *Baltic Biophysics Conference*, Kaunas (Lithuania), 2024.
- A. Polita, Revealing lipid order differences between cancerous and non-cancerous cells using fluorescent viscosity probes, *Spanish & Portuguese Advanced Optical Microscopy Meeting*, Toledo (Spain), 2024.

- A. Polita, Revealing lipid order differences between cancerous and non-cancerous cells using fluorescent viscosity probes, *15th European Biophysical Societies' Association Congress*, Rome (Italy), 2025.

Other Publications

- **A. Polita**, R. Bagdonaitė, A. P. Shivabalan, and G. Valinčius, Influence of Simvastatin and Pravastatin on the Biophysical Properties of Model Lipid Bilayers and Plasma Membranes of Live Cells, *ACS Biomaterials Science & Engineering*, 2024, 10, 5714–5722. DOI: 10.1021/acsbiomaterials.4c00911.

- T. Sabirovas, M. Talaikis, R. Tamulytė, **A. Polita**, V. Pudžaitis, G. Niaura, D. J. Vanderah, and G. Valinčius, Molecular engineering of tethered bilayer lipid membranes for impedimetric detection of pore-forming toxins, *Electrochimica Acta*, 2024, 508, 145226. DOI: 10.1016/j.electacta.2024.145226.

- I. Gabriūnaitė, T. Sabirovas, F. Ambrulevičius, L. Labanauskas, R. Lapinskaitė, **A. Polita**, D. J. Vanderah, G. Valinčius, and A. Valiūnienė, Sensitivity of lipid bilayer sensing of pore-forming toxins relies on electrical properties of nanoscale-thick submembrane reservoir separating solid support and phospholipid membrane, *Electrochimica Acta*, 2025, 526, 146189.
DOI: 10.1016/j.electacta.2025.146189.

- E. Jankaitytė, **A. Polita**, A. Sakalauskas, R. Tamulytė, V. Smirnovas, and R. Budvytytė, Impact of Lipid Composition and Synergistic Effect on Aβ42 Oligomers-Induced Changes in Membrane Conductance and Microviscosity, *ACS Chemical Neuroscience*, 2026, x, xxxx-xxxx.

- S. Arun Prabha, M. Talaikis, **A. Polita**, V. Pudžaitis, M. Noreikienė, R. Budvytytė, and G. Valinčius, Formation of Tethered Bilayer Lipid Membranes (tBLMs) using Plasma Membrane Blebs of Human Lung Cancer Cells, *ACS Omega*, 2026, x, xxxx-xxxx.

Publications by the Author

1st publication

Designing a green-emitting viscosity-sensitive 4, 4-difluoro-4-bora-3a, 4a-diaza-s-indacene (BODIPY) probe for plasma membrane viscosity imaging

A. Polita, M. Stancikaitė, R. Žvirblis, K. Maleckaitė, J. Dodonova-Vaitkūnienė, S. Tumkevičius, A. P. Shivabalan, and G. Valinčius

RSC Advances, 2023, 13, 19257–19264.

DOI: 10.1039/D3RA04126C

Author Contributions: Photophysical characterization of *BODIPY-PM* in solvents of varying viscosity and polarity; preparation of model membrane systems; fluorescence lifetime imaging experiments; analysis and interpretation of spectroscopic and imaging data; preparation of figures; and writing of the original manuscript draft.

RSC Advances

PAPER

View Article Online
View Journal | View Issue

Cite this: *RSC Adv.*, 2023, **13**, 19257

Designing a green-emitting viscosity-sensitive 4,4-difluoro-4-bora-3a,4a-diaza-*s*-indacene (BODIPY) probe for plasma membrane viscosity imaging†

Artūras Polita,*[a] Milda Stancikaitė,[b] Rokas Žvirblis,[c] Karolina Maleckaitė,[b] Jelena Dodonova-Vaitkūnienė,[d] Sigitas Tumkevičius,[d] Arun Prabha Shivabalan[a] and Gintaras Valinčius[a]

Received 19th June 2023
Accepted 20th June 2023

DOI: 10.1039/d3ra04126c

rsc.li/rsc-advances

Viscosity is a key characteristic of lipid membranes – it governs the passive diffusion of solutes and affects the lipid raft formation and membrane fluidity. Precise determination of viscosity values in biological systems is of great interest and viscosity-sensitive fluorescent probes offer a convenient solution for this task. In this work we present a novel membrane-targeting and water-soluble viscosity probe BODIPY-PM, which is based on one of the most frequently used probes BODIPY-C_{10}. Despite its regular use, BODIPY-C_{10} suffers from poor integration into liquid-ordered lipid phases and lack of water solubility. Here, we investigate the photophysical characteristics of BODIPY-PM and demonstrate that solvent polarity only slightly affects the viscosity-sensing qualities of BODIPY-PM. In addition, with fluorescence lifetime imaging microscopy (FLIM), we imaged microviscosity in complex biological systems – large unilamellar vesicles (LUVs), tethered bilayer membranes (tBLMs) and live lung cancer cells. Our study showcases that BODIPY-PM preferentially stains the plasma membranes of live cells, equally well partitions into both liquid-ordered and liquid-disordered phases and reliably distinguishes lipid phase separation in tBLMs and LUVs.

Introduction

Viscosity is the essential physical characteristic of cell membranes – it controls diffusion coefficients of lipids and macromolecules and influences the passive transport of solutes across the plasma membrane.[1] Furthermore, cell membranes are microscopically heterogeneous and are able to separate into liquid-ordered (Lo) and liquid-disordered (Ld) phases that possess distinct viscosities.[2–5] Viscous Lo phases are of particular biological importance – ordered microdomains of lipids and proteins, so called lipid rafts, play a key role in immune signaling,[6,7] host–pathogen interactions,[8,9] cardiovascular diseases,[10] and cancer.[11–13] Thus, the ability to distinguish Lo and Ld phases in live cells would benefit studies of membrane dynamics and biochemical processes associated with lipid raft formation. Fortunately, lipids in the Lo phase are packed tightly, and the Lo phase is much more viscous compared to the Ld phase, thus the two phases can be distinguished on the basis of viscosity.[14,15] Precise determination of viscosity values in Lo and Ld phases would allow comparison of lipid packaging efficiencies and molecular order changes in the plasma membrane.

Accurate mechanical viscosity measurements in micron-scale objects are inherently difficult. Additionally, biological specimens are highly heterogeneous and viscosity values in protein-rich Lo domains will differ from Ld domains or the cytoplasm.[16] Precise and quantitative viscosity measurements on the small scale can be made utilizing fluorescent class of compounds called molecular rotors.[17–19] Molecular rotors, when paired with fluorescence lifetime imaging microscopy (FLIM), are able to produce spatial microviscosity maps.[20–22] The term microviscosity here refers to the lipid packaging and molecular mobility of the probe's local environment.[23]

In the excited state, molecular rotors undergo intramolecular rotation, which results in a molecular rotor leaving the fluorescent state.[24] As the rate of intramolecular rotation is directly influenced by microviscosity, molecular rotors display great fluorescence lifetime and fluorescence intensity sensitivity to local viscosity values.[25] In high viscosity environments, intramolecular motion of molecular rotors is restricted and radiative decay dominates, leading to increased fluorescence lifetime values and high quantum yields.[25] Conversely, in low

[a]*Institute of Biochemistry, Life Sciences Center, Vilnius University, Saulėtekio Av. 7, Vilnius, LT-10257, Lithuania. E-mail: arturas.polita@gmc.vu.lt*
[b]*Center of Physical Sciences and Technology, Saulėtekio Av. 3, Vilnius, LT-10257, Lithuania*
[c]*Life Sciences Center, Institute of Biotechnology, Vilnius University, Saulėtekio Av. 7, Vilnius, LT-10257, Lithuania*
[d]*Institute of Chemistry, Faculty of Chemistry and Geosciences, Vilnius University, Naugarduko St. 24, Vilnius, LT-03225, Lithuania*

† Electronic supplementary information (ESI) available. See DOI: https://doi.org/10.1039/d3ra04126c

viscosity environments, non-radiative decay dominates, causing the decrease in fluorescence lifetime and quantum yield. Since the fluorescence intensity is dependent on the local concentration of a fluorophore, it is particularly advantageous to evaluate viscosity values from the fluorescence lifetime, which is independent of the fluorophore concentration, and is largely unaffected by optical properties of the medium or the excitation setup. Fluorescence lifetimes have been used to quantify microviscosities of model lipid bilayer systems, as well as live eukaryotic and prokaryotic cells through FLIM.[26–31]

Currently, BODIPY-$C_{10/12}$ (Fig. 1A) is one of the most extensively used molecular rotors for viscosity sensing.[32,33] Previously, BODIPY-$C_{10/12}$ and its derivatives were used to quantify viscosity in polymers,[34] model lipid membranes,[35] live cells,[36,37] plasma membrane,[38] mitochondria,[39] and lysosomes.[40] Although BODIPY-C_{10} has a monoexponential fluorescence decay,[41] which greatly simplifies data analysis, this rotor lacks affinity for the higher ordered lipid phases,[42] which decreases its ability to sense the Lo phase. Due to poor partitioning of BODIPY-C_{10} into Lo phases, small Lo domains (*e.g.* lipid rafts) are easily missed in biological samples, and especially in live cells.[35]

Moreover, BODIPY-C_{10} suffers from unclear localisation of the probe in higher ordered lipid bilayers[42,43] – around 10–15% of BODIPY molecules are localised in such a way that viscosity changes in a bilayer do not alter their intramolecular rotation.[35] Ultimately, this lowers the average lifetime values and reduces the probe's sensitivity to viscosity changes.

In this work, we present a novel BODIPY derivative probe, BODIPY-PM, which carries a long hydrophobic plasma membrane (PM) targeting group ($C_{12}H_{25}$) together with a polar sulfonate group SO_3^-. The combination of a charged sulfonate group with a hydrophobic tail and the non-polar BODIPY-core, mimics natural phospholipid structures and enables firm positioning of BODIPY-PM into the lipid bilayer (Fig. 1B). We explore the photophysics of BODIPY-PM and its ability to distinguish Lo and Ld membrane phases in large unilamellar vesicles (LUVs), tethered bilayer lipid membranes (tBLMs) and live cancer cells. LUVs and tBLMs represent one of the most frequently used model lipid bilayer systems and are often employed to study and mimic cell membranes.[44] Specifically, by comparing fluorescence lifetimes of BODIPY-PM in solvents of different polarities and viscosities, we show that BODIPY-PM is affected mainly by the viscosity of the solvent. By performing time-resolved fluorescence measurements in LUVs with Lo and Ld lipid compositions, we demonstrate that BODIPY-PM successfully distinguishes lipid order and displays vastly different fluorescence lifetimes in Lo and Ld LUVs. Furthermore, with the help of FLIM, we investigate the potential of BODIPY-PM to distinguish separate Lo domains in tBLMs and LUVs. Finally, by carrying out FLIM measurements on live lung cancer cells, we show that BODIPY-PM preferentially localises in the plasma membrane and is efficient at recognising viscous Lo phases in the lipid bilayer. To our knowledge, among comparable viscosity probes, BODIPY-PM achieves the largest fluorescence lifetime contrast between the Lo and Ld phases. The narrow emission spectrum of BODIPY-PM allows for the multiple dye usage in biological samples and offers a convenient alternative to Kuimova's thiophene[27,45] or Klymchenko's solvatochromic dyes.[46]

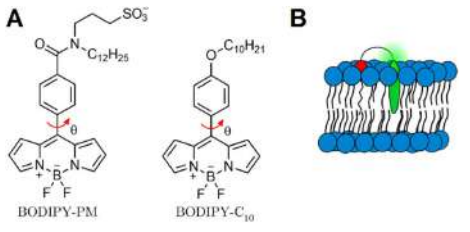

Fig. 1 (A) Structure of one of the most widely used molecular rotor – BODIPY-C_{10}, and its improved variant BODIPY-PM. Red arrow indicates intramolecular rotation which causes BODIPY to display viscosity sensitivity. (B) Supposed positioning of BODIPY-PM in the lipid bilayer.

Results and discussion

Probe design

Our BODIPY-PM design was based on one of the most applicable and successful rotors up to date – BODIPY-C_{10}. Our intent was to retain the same mechanism of viscosity sensitivity of BODIPY-C_{10}, thus we decided to keep the rotation of the phenyl group *versus* the BODIPY unhindered and modified the *para*-position of the phenyl group. Our aim was to enable the firm positioning of the probe inside highly ordered lipid phases, increase the water solubility of the probe and decrease the possibility of dye aggregation in water. Consequently, we elongated the hydrophobic tail ($C_{12}H_{25}$) and introduced a sulfonate group – this combination of substituents mimics the structure of lipids, with polar sulfonate group emerging from the bilayer and hydrophobic tail serving as a membrane anchor. In addition to conferring increased water solubility, the sulfonate group also disrupts dye–dye interactions and confers resistance to probe aggregation. Finally, the $C_{12}H_{25}$ side chain grants the dye high affinity for ordered lipid bilayer phases and cell membranes. The synthesis of BODIPY-PM is described in the ESI.†

Absorption, steady-state and time-resolved fluorescence

In order to investigate the spectroscopic properties of BODIPY-PM, we carried out absorption, steady-state, and time-resolved fluorescence experiments in different polarity solvents from non-polar [chloroform and dichloromethane (DCM)], to very polar [dimethyl sulfoxide (DMSO) and water] (Fig. 2). The absorption spectra of BODIPY-PM consist of a low intensity band at 300–400 nm and the main band in the 450–550 nm region with maximum positioned at 503 nm (Fig. 2A). The fluorescence spectra of BODIPY-PM feature a small bathochromic shift with the fluorescence peak at 523 nm and a Stokes shift of 760 cm^{-1} (Fig. 2A). Additionally, BODIPY-PM displays almost no fluorescence solvatochromism, resulting in a blue shift of only 3 nm when going from the least polar chloroform to the most polar water solvent (Fig. 2A). We have

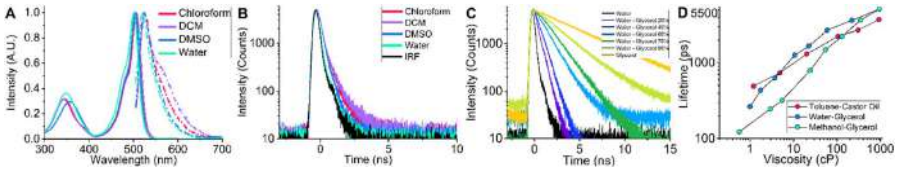

Fig. 2 (A) Fluorescence (dot-dashed lines) and absorption (solid lines) spectra of BODIPY-PM obtained in chloroform, DCM, DMSO and water. (B) Time-resolved fluorescence decays of BODIPY-PM in chloroform, DCM, DMSO, and water. (C) Time-resolved fluorescence decays of BODIPY-PM obtained in water–glycerol mixtures of varying viscosities. (D) Fluorescence lifetimes of BODIPY-PM in toluene–castor oil (red dots), water–glycerol (blue dots) and methanol–glycerol (green dots) mixtures.

also observed that in very non-polar solvents, such as toluene and cyclohexane, BODIPY-PM does not completely dissolve and tends to aggregate, producing characteristic red bands in the fluorescence spectra and increased fluorescence lifetimes (Fig. S1†). In addition, we performed time-resolved fluorescence measurements in chloroform, DCM, DMSO, and water (Fig. 2B). In the high polarity solvents, the fluorescence decays of BODIPY-PM are monoexponential with fluorescence lifetimes close to 200 ps, while in the low-polarity solvents (cyclohexane, toluene, chloroform, and DCM) BODIPY-PM displays biexponential fluorescence decays with an insignificant long lifetime component (0.5–10%) (Fig. 2B and S1†). These data clearly show that the fluorescence lifetimes of BODIPY-PM are minimally influenced by the polarity of the solvent. To explore the viscosity sensitivity of BODIPY-PM, we measured the steady-state and time-resolved fluorescence responses in water–glycerol mixtures with varying water–glycerol compositions that cover a viscosity range from 1–930 cP, (Fig. 2C and S4†). The fluorescence decays were monoexponential in compositions from pure water to 40% water–60% glycerol. At higher glycerol concentrations, the decays become biexponential with low amplitude short-lifetime component. We note that BODIPY-PM displays very strong viscosity sensitivity, with fluorescence lifetimes ranging from 264 ps in pure water to 5127 ps in pure glycerol. Additionally, we quantified the fluorescence lifetime of BODIPY-PM in non-polar toluene–castor oil and methanol–glycerol calibration mixtures (Fig. 2D, S2 and S6†). In contrast to BODIPY-C_{10}, which possessed fluorescence lifetimes ranging from 300 to 800 ps in the solvents of 0.5 cP viscosity,[38] BODIPY-PM exhibits very similar fluorescence lifetimes in mixtures of different polarity and is mostly influenced by the viscosity of the mixture itself (Fig. 2D). The insensitivity of BODIPY-PM to solvent polarity is particularly important since biological systems, and especially cells, are highly heterogeneous and accurate viscosity measurements are only possible if the lifetimes are not affected by general solvent effects.[47] Because of small fluorescence lifetime values in the non-viscous solvents, BODIPY-PM features greatly expanded dynamic viscosity range, which can be calculated from the lifetime ratio at high and low viscosities, compared to BODIPY-C_{10}. In the methanol–glycerol mixtures, the dynamic range of BODIPY-PM is 30.0 compared to 11.2 of BODIPY-C_{10} in the same mixture.[41]

To conclude, BODIPY-PM shows almost no sensitivity to solvent polarity and its fluorescence lifetime is mainly affected by the local microviscosity.

Determination of lipid order in LUVs and tBLMs

Next, we explored the viscosity sensitivity of BODIPY-PM in Lo and Ld lipid phases. We prepared LUVs with two distinct lipid packaging compositions – pure DOPC and pure POPC for Ld phases, and DOPC : BSM : Chol and DOPC : DPPC : Chol (5 : 5 : 1) LUVs for Lo phases.[48] The steady-state fluorescence spectra of BODIPY-PM in the Lo and Ld phases display no solvatochromism, with maxima located at 521 nm (Fig. 3A). We note that BODIPY-PM successfully integrates into both Lo and Ld LUVs without any observable aggregation. Most importantly, the time-resolved fluorescence decays in the Lo phases are remarkably longer compared to the Ld phases (Fig. 3B), with biexponential intensity-weighted fluorescence lifetimes being 877 and 1607 ps for DOPC and POPC LUVs, respectively. In contrast, the biexponential fluorescence lifetimes of BODIPY-PM in DOPC : DPPC : Chol and DOPC : BSM : Chol LUVs were 3321 ps and 2167 ps, respectively. Although the biexponential nature of fluorescence decays likely reflects different positioning of the dye in the bilayer and complicates data analysis, the ability to determine lipid order and discern Lo and Ld phases is especially important for determination of biologically relevant Lo phases, and lipid rafts, *via* FLIM, particularly in heterogeneous lipid systems and live cells.

In addition, we tested BODIPY-PM in gel-phase DMPC and DPPC LUVs. Even though the lipid packaging density in the gel-phase is significantly higher than in Lo phase, the time-resolved fluorescence decays of BODIPY-PM were slightly shorter in DMPC and DPPC LUVs compared to Lo LUVs (Fig. S8†). It is likely that the BODIPY core is sterically too large and is unable to integrate deeply into densely-packed gel-phase bilayers. To test this hypothesis, we carried out time-resolved fluorescence measurements of gel-phase LUVs in the presence of the quencher NaI (Fig. 3C and S9†). The fluorescence lifetimes of DMPC LUVs sharply dropped from 2674 ps in NaI-free solution, to 1405 ps in solutions containing NaI (1 M). In contrast, the time-resolved fluorescence decays of Ld POPC LUVs remained almost unaffected by the presence of 1 M NaI (Fig. 3C), with fluorescence lifetimes decreasing from 1607 ps in NaI-free solution, to 1458 ps in the presence of NaI (1 M). This result indicates that the fluorescent core of BODIPY-PM is exposed to solvent in gel-phase LUVs and only the hydrophobic $C_{12}H_{25}$ side chain integrates into the bilayer. On the other hand, the minimal quenching of BODIPY-PM in Ld LUVs confirms that BODIPY-PM core is indeed deeply buried inside the bilayer.

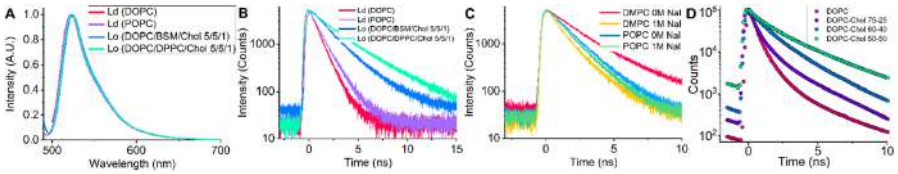

Fig. 3 (A) Fluorescence spectra of BODIPY-PM in Ld and Lo LUVs. (B) Time-resolved fluorescence decays of BODIPY-PM in Ld and Lo LUVs. (C) Time-resolved fluorescence decays of BODIPY-PM in LUVs quenched with NaI. (D) FLIM decays of BODIPY-PM in DOPC : Chol tBLMs with varying cholesterol levels.

Next, we explored how cholesterol in tBLMs (see Experimental section for tBLM composition) affects the lifetimes of BODIPY-PM, using FLIM. Cholesterol is one the most important lipids in eukaryotic cells and is particularly known for its ordering and condensing effects on lipid bilayers.[49] For the preparation of tBLMs we chose pure DOPC (Ld), DOPC : Chol 72 : 25, DOPC : Chol 60 : 40, and DOPC : Chol 50 : 50 compositions. The time-resolved fluorescence decays of BODIPY-PM in tBLMs become significantly longer with increase in cholesterol concentration, resulting in the intensity weighted biexponential fluorescence lifetimes of 500 and 1900 ps for pure DOPC and DOPC : Chol 50 : 50 tBLMs, respectively (Fig. 3D).

Importantly, not only is BODIPY-PM capable of distinguishing between the Lo and Ld lipid compositions, it also gives valuable insights into the general lipid packaging efficiency and order of the lipids in the bilayer. The ability of BODIPY-PM to assess the degree of lipid order may be particularly useful in studying lipid rearrangement in membranes, the fusion of membranes, and in monitoring the biophysical changes in the bilayer upon binding of proteins. Moreover, the minimal quenching displayed by BODIPY-PM in liquid membranes is a very convenient property for live cell imaging, since the probe, buried deeply in the bilayer, is shielded from extracellular proteins, which may interfere with the viscosity measurements of the plasma membrane.

Imaging of Lo domains in LUVs, tBLMs and live cells

We used FLIM to test BODIPY-PM on LUVs and tBLMs in which Lo and Ld phase separation occurs (Fig. 4). For this purpose, we chose DOPC : DPPC : Chol 1 : 1 : 1 LUVs, DOPC : DPPC : Chol 2 : 2 : 1 and DOPC : BSM : Chol 1 : 1 : 1 tBLMs, since large, micron-scale, Lo domains are easily formed in these compositions.[50] The Lo domains in the tBLMs formed with characteristic geometrical features, analogous to the Lo domains observed with atomic force microscopy in supported lipid bilayers of similar compositions.[51] We observed successful staining of both Lo and Ld phases with BODIPY-PM in both tBLMs and LUVs. The BODIPY-PM showed particularly high affinity for the Lo phase, with fluorescence intensities in the Lo phase being similar (or even 2-times higher in the DPPC case) compared to the Ld phase (Fig. 4 top panel). Despite the fact that the fluorescence decays in both LUVs and tBLMs were biexponential, the fluorescence lifetimes of BODIPY-PM in Lo and Ld phases are vastly different, allowing easy determination of lipid phases *via* FLIM (Fig. 4 middle panel). Curiously, the fluorescence lifetimes in DOPC : DPPC : Chol 1 : 1 : 1 LUVs were notably higher in both Lo and Ld phases compared to the fluorescence lifetimes in the corresponding phases of the DOPC : DPPC : Chol 2 : 2 : 1 tBLMs (Fig. 4A and B). We suppose that the increase in cholesterol concentration not only orders Ld phase, but also induces order in Lo domains, consequently making them more viscous. Similarly, tBLMs with high cholesterol content, such as DOPC : BSM : Chol 1 : 1 : 1, possessed increased fluorescence lifetimes in the Ld phases (Fig. 4C).

Finally, we used FLIM to image BODIPY-PM in A549 live lung cancer cells (Fig. 4D). BODIPY-PM stained the cells in less than 5 minutes directly from the aqueous solution at 1 μM concentration. Notably, no signs of cell toxicity or BODIPY-PM induced morphology changes were observed after staining (Fig. S10†). We also note that BODIPY-PM preferentially partitions into the plasma membranes of the cells, although slow internalisation of the dye is also occurring. In addition, we observed slight clustering of highly ordered lipid domains in the plasma membranes of lung cancer cells. The ability to directly observe the heterogeneities of cell membranes, in combination with lipid order determination, could prove to be a powerful tool in studying and developing anticancer drugs that modulate the properties of the plasma membrane.[52] The slow internalisation of BODIPY-PM allows for simultaneous plasma membrane and cytoplasm viscosity measurements. The large dynamic range of BODIPY-PM viscosity sensitivity is particularly convenient in detecting small viscosity changes in cell membranes.

In the case of human lung cancer cells, the intensity-weighted fluorescence lifetime of BODIPY-PM in the plasma membrane regions, where the clustering of Lo domains is not occurring, was about 3250 ps, which corresponds to the viscosity value of 300 cP in methanol–glycerol calibration mixtures. In comparison, similar plasma membrane viscosity values of 290 and 326 cP were obtained by Shimolina *et al.* in the colorectal cancer CT26 cells and cervical HeLa cells, respectively.[53] In contrast, the fluorescence lifetime of BODIPY-PM in the more ordered plasma membrane regions of the lung cancer cells was about 3700 ps, corresponding to a viscosity value of about 400 cP. The intensity-weighted fluorescence lifetime of BODIPY-PM in the cytoplasm ranged from 3250 to 3700 ps, corresponding to the viscosity values of 130 and 180 cP, respectively. Similar cytoplasmic viscosity values were reported

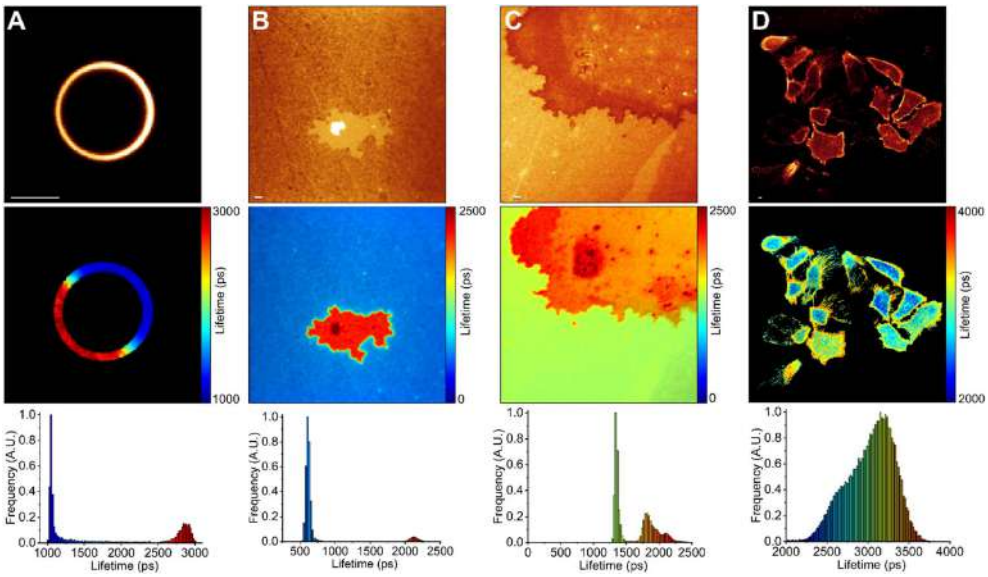

Fig. 4 FLIM of BODIPY-PM in DOPC/DPPC/Chol 1 : 1 : 1 LUVs (A), DOPC/DPPC/Chol 2 : 2 : 1 tBLMs (B), DOPC/BSM/Chol 1 : 1 : 1 tBLMs (C), live lung cancer cells (D). The top panel shows images of fluorescence intensity. FLIM images are shown in the middle panel; the lifetime scale is in picoseconds. The corresponding lifetime histograms are shown in the bottom panel. The lifetime of BODIPY-PM shows a clear increase in Lo (red colour) phases. Scale bars are 1 μm.

in ovarian cancer cells (SK-OV-3) by Kuimova *et al.*, with an average intracellular viscosity of 140 cP.[54]

Conclusions

In conclusion, we have synthesised and explored the capabilities of a new BODIPY-based molecular rotor – BODIPY-PM (A, Fig. 1). We found that addition of a hydrophobic dodecyl group ($-C_{12}H_{25}$) allows the dye to position deeply in liquid-ordered and liquid-disordered phases of a lipid bilayer. Additionally, a polar sulfonate group ($-SO_3^-$) provides good water solubility and enables the easy, non-toxic, staining of the cells from aqueous solutions. We show that fluorescence decays of BODIPY-PM display minimal sensitivity to solvent polarity, but are sensitive to viscosity over a large range, from 0.5 to 1000 cP. Most importantly, FLIM measurements on tBLMs and LUVs, demonstrate that BODIPY-PM possesses vastly different fluorescence lifetimes in lipid-ordered and lipid-disordered environments, allowing this probe to successfully distinguish membrane phase heterogeneities. Additionally, the extent of lipid packaging in bilayers can be estimated based on the dynamic range of viscosity sensing of BODIPY-PM. We have also discovered that BODIPY-PM is localised deeply in non-gel phase bilayers and is not susceptible to external quenching effects. BODIPY-PM preferentially stains the plasma membranes of eukaryotic cells without causing any changes to the cell morphology.

Overall, our results demonstrate that BODIPY-PM is capable of probing viscosities in physically distinct membranes, making the dye widely applicable in studying lipid packaging and membrane dynamics in live cells or artificial membranes.

Experimental section

Dyes, reagents, and solvents

The synthetic details of BODIPY-PM, with mass and NMR spectra, are presented in the ESI.† NMR spectra were recorded on a Bruker Ascend 400 spectrometer (400 MHz for ^{1}H, 100 MHz for ^{13}C, 128.4 MHz for ^{11}B, 376.5 MHz for ^{19}F). NMR spectra were referenced to residual solvent peaks. HRMS spectra were recorded on a quadrupole, time-of-flight mass spectrometer (microTOF-Q II, Bruker Daltonik GmbH, Germany). Column chromatography was performed using silica gel 60 (0.040–0.063 mm) (Merck). Thin layer chromatography (TLC) was performed using TLC-aluminium sheets with silica gel (Merck 60 F254). Visualisation was accomplished by UV light. Melting points were determined in open capillaries with a digital melting point IA9100 series apparatus (Thermo Fisher Scientific) and were not corrected. Reagents and solvents for the organic synthesis of the BODIPY compounds were purchased directly from commercial suppliers; solvents were purified by known procedures. Stock solutions of 2 mM BODIPY-PM were prepared in methanol or water and diluted for further experiments in solvents or their mixtures. All solvents used were spectroscopic grade obtained from Sigma-Aldrich. DOPC, DPPC, brain sphingomyelin, cholesterol were obtained from Avanti Polar Lipids (Alabaster, USA). Solvent mixtures were made by mixing reagents at different ratios.

Formation of tBLMs and LUVs

Stock solutions of lipids were mixed in appropriate ratios and placed under gentle gaseous nitrogen stream for at least 2 hours to evaporate the chloroform. After complete evaporation, PBS buffer was added on top of lipid film and the mixture was slowly re-suspended until the characteristic milk colour appeared, indicating vesicle formation. The total concentration of lipids in the PBS solution was 1 mM. Afterwards, vesicle mixtures were poured on top of the 100 nm thick gold surface of mica and membranes were allow to form for 2 hours. 20-Tetradecyloxy-3,6,9,12,15,18,22 heptaoxahexatriacontane-1-thiol (WC14) was used as an anchoring compound in combination with β-mercaptoethanol in 3 : 7 molar ratios. For DOPC/DPPC/Chol and DOPC/BSM/Chol bilayer compositions, the lipids were re-suspended in hot PBS buffer (60 °C) and the membranes were formed in an oven, with slow decrease in temperature from 60 to 20 °C over the course of 2 h, after which, the membranes were gently washed in PBS buffer and an aqueous solution of BODIPY-PM (1 μM) was added. The membranes were stained (3 min), followed by removal of non-incorporated dye with a PBS wash.

LUVs were formed by mixing lipids in appropriate ratios, evaporating the chloroform under nitrogen stream for at least 2 hours. After evaporation, PBS buffer was added on top of the film. In the case of gel-phase or mixed-phase LUVs, PBS buffer was heated to 60 °C. After resuspension, mixtures were placed in an ultrasonic bath (1 h) and extruded through 100 nm or 1000 nm polycarbonate membranes with a syringe extruder (Avanti Polar Lipids Inc., USA). Extrusions were performed above the melting temperature of the lipids.

Absorption, steady-state, and time-resolved fluorescence

Absorption spectra were measured using a Jasco V-670 spectrophotometer. Fluorescence spectra were recorded with Edinburgh-F900 (Edinburgh Instruments) fluorimeter using Fianium white laser, together with bandpass filters (Thorlabs), emitting at 488 nm as an excitation source. Fluorescence decays were measured using time-correlated single-photon counting (TCSPC). Fluorescence decays had 5000 counts at the peak of the decay with 20 ns time window being used with 4096 channels in time domain. 10 mm quartz cuvettes were used for absorption and fluorescence measurements with BODIPY-PM concentration being up to 1 μM. Fluorescence decays of BODIPY-PM in solvent mixtures and pure solvents were taken at 20 °C.

Imaging of live cells

Cell imaging experiments were done using the A549 human lung cancer cell line (ATCC). The cells were cultured in Dulbecco's Modified Eagle's Medium (DMEM) supplemented with 10% foetal bovine serum (FBS), 100 IU mL^{-1} penicillin and 100 μg mL^{-1} streptomycin (Thermo Fisher). The cells were incubated at 37 °C with 5% CO_2. Before imaging, cells were seeded into Ibidi μ-Dish (Ibidi) at seeding density of 10 000 cells per mL and allowed to grow for 24 hours. For cell imaging, cells were kept in the 1 μM solution of BODIPY-PM in PBS for 1 min at 37 °C and then washed with PBS. FLIM imaging was done using Leica SP8 with 63× objective (HC PL APO oil immersion, N.A. – 1.4, Leica).

Fluorescence lifetime imaging microscopy (FLIM)

FLIM was done with a Leica SP8 microscope using 63× objective (HC PL APO oil immersion, N.A. – 1.4, Leica). The fluorescence decay signal was measured over 505–550 nm range using 488 nm white light laser excitation line. The FLIM images were produced in 256 × 256 pixel resolution with 256 channels in time domain, pixels were binned in order to have at least 1000 counts at the peak of the decay curve for reliable biexponential fitting. The instrument response function (IRF) was measured by recording the laser reflection signal off a glass coverslip.

Data analysis

FLIM images were analysed with FLIMFIT software (v4.6.1, Imperial College London).[55] The biexponential fluorescence decay model with intensity-weighted mean lifetimes was applied for both FLIM and fluorimeter time-correlated single photon counting (TCSPC) measurements:

$$\tilde{\tau} = \frac{\sum_i a_i \tau_i^2}{\sum_i a_i \tau_i}$$

where a_i and τ_i are the amplitudes of the individual components. The goodness-of-fit parameter (χ^2) was 1.3 or less for both FLIM images and fluorimeter TCSPC decays. Fluorimeter TCSPC decays of BODIPY-PM were fitted using Edinburgh-F900 software package F900.

Conflicts of interest

The authors declare no conflict of interest.

Acknowledgements

The authors thank David J. Vanderah (Institute for Bioscience and Biotechnology Research at University of Maryland, Rockville MD, USA) for providing samples of anchor compound WC14 and critical reading of the manuscript.

Notes and references

1 M. S. Gh, *Mol. Pharmaceutics*, 2021, **18**, 2122–2141.
2 D. Lingwood and K. Simons, *Science*, 2010, **327**, 46–50.
3 H.-J. Kaiser, D. Lingwood, I. Levental, J. L. Sampaio, L. Kalvodova, L. Rajendran and K. Simons, *Proc. Natl. Acad. Sci. U. S. A.*, 2009, **106**, 16645–16650.
4 A. T. Hammond, P. Sengupta, S. T. Hess, D. A. Holowka, B. A. Baird and W. W. Webb, *Proc. Natl. Acad. Sci. U. S. A.*, 2007, **104**, 3165–3170.
5 C. Eggeling, C. Ringemann, R. Medda, G. Schwarzmann, K. Sandhoff, S. Polyakova, V. N. Belov, B. Hein,

C. v. Middendorff, A. Schönle and S. W. Hell, *Nature*, 2009, **457**, 1159–1162.
6 K. A. Field, D. Holowka and B. Baird, *Proc. Natl. Acad. Sci. U. S. A.*, 1995, **92**, 9201–9205.
7 P. Varshney, V. Yadav and N. Saini, *Immunology*, 2016, **149**, 13–24.
8 K. Iwabuchi, *Front. Biosci.*, 2015, **20**, 325–334.
9 E. Teissier and E. Pecheur, *Eur. Biophys. J.*, 2007, **36**, 887–899.
10 F. J. O. Rios, M. Ferracini, M. Pecenin, M. M. Koga, Y. Wang, D. F. J. Ketelhuth and S. Jancar, *PLoS One*, 2013, **8**, e76893.
11 J. B. Larsen, M. B. Jensen, V. K. Bhatia, S. L. Pedersen, T. Bjørnholm, L. Iversen, M. Uline, I. Szleifer, K. J. Jensen, N. S. Hatzakis and D. Stamou, *Nat. Chem. Biol.*, 2015, **11**, 192–194.
12 C. Gajate and F. Mollinedo, *Blood*, 2007, **109**, 711–719.
13 Á. Cuesta-Marbán, J. Botet, O. Czyz, L. M. Cacharro, C. Gajate, V. Hornillos, J. Delgado, H. Zhang, F. Amat-Guerri, A. U. Acuña, C. R. McMaster, J. L. Revuelta, V. Zaremberg and F. Mollinedo, *Nat. Chem. Biol.*, 2015, **11**, 192–194.
14 C. Dietrich, L. A. Bagatolli, Z. N. Volovyk, N. L. Thompson, M. Levi, K. Jacobson and E. Gratton, *Biophys. J.*, 2001, **80**, 1417–1428.
15 R. Žvirblis, K. Maleckaitė, J. Dodonova-Vaitkūnienė, D. Jurgutis, R. Žilėnaitė, V. Karabanovas, S. Tumkevičius and A. Vyšniauskas, *J. Mater. Chem. B*, 2023, **11**, 3919–3928.
16 A. S. Klymchenko, *Acc. Chem. Res.*, 2017, **50**, 366–375.
17 A. Vyšniauskas and M. K. Kuimova, *Int. Rev. Phys. Chem.*, 2018, **37**, 259–285.
18 M. A. Haidekker and E. A. Theodorakis, *Org. Biomol. Chem.*, 2007, **5**, 1669–1678.
19 M. A. Haidekker and E. A. Theodorakis, *J. Biol. Eng.*, 2010, **4**, 11.
20 L. E. Shimolina, A. A. Gulin, M. Paez-Perez, I. López-Duarte, I. N. Druzhkova, M. M. Lukina, M. V. Gubina, N. J. Brooks, E. V. Zagaynova, M. K. Kuimova and M. V. Shirmanova, *J. Biomed. Opt.*, 2020, **25**, 1–16.
21 L. Shimolina, M. Lukina, V. Shcheslavskiy, V. Elagin, V. Dudenkova, N. Ignatova, M. K. Kuimova and M. Shirmanova, *J. Visualized Exp.*, 2021, **173**, e62708.
22 A. Vyšniauskas, M. Qurashi and M. K. Kuimova, *Chem. –Eur. J.*, 2016, **22**, 13210–13217.
23 M. R. Bittermann, M. Grzelka, S. Woutersen, A. M. Brouwer and D. Bonn, *J. Phys. Chem. Lett.*, 2021, **12**, 3182–3186.
24 M. K. Kuimova, *Phys. Chem. Chem. Phys.*, 2012, **14**, 12671–12686.
25 S.-C. Lee, J. Heo, H. C. Woo, J.-A. Lee, Y. H. Seo, C.-L. Lee, S. Kim and O.-P. Kwon, *Chem. –Eur. J.*, 2018, **24**, 13706–13718.
26 A. Vyšniauskas, M. Qurashi and M. K. Kuimova, *Chem. –Eur. J.*, 2016, **22**, 13210–13217.
27 M. R. Dent, I. López-Duarte, C. J. Dickson, P. Chairatana, H. L. Anderson, I. R. Gould, D. Wylie, A. Vyšniauskas, N. J. Brooks and M. K. Kuimova, *Chem. Commun.*, 2016, **52**, 13269–13272.
28 M. Kubánková, I. López-Duarte, D. Kiryushko and M. K. Kuimova, *Soft Matter*, 2018, **14**, 9466–9474.
29 A. Vyšniauskas, I. López-Duarte, N. Duchemin, T.-T. Vu, Y. Wu, E. M. Budynina, Y. A. Volkova, E. P. Cabrera, D. E. Ramírez-Ornelas and M. K. Kuimova, *Phys. Chem. Chem. Phys.*, 2017, **19**, 25252–25259.
30 Z. Yang, Y. He, J. H. Lee, W.-S. Chae, W. X. Ren, J. H. Lee, C. Kang and J. S. Kim, *Chem. Commun.*, 2014, **50**, 11672–11675.
31 S.-C. Lee, J. Heo, J.-W. Ryu, C.-L. Lee, S. Kim, J.-S. Tae, B.-O. Rhee, S.-W. Kima and O.-P. Kwon, *Chem. Commun.*, 2016, **52**, 13695–13698.
32 Y. Shi, P. A. Summers, M. K. Kuimova and H. S. Azevedo, *Nano Lett.*, 2020, **20**, 7375–7381.
33 R. Clark, M. A. Nawawi, A. Dobre, D. Pugh, Q. Liu, A. P. Ivanov, A. J. P. White, J. B. Edel, M. K. Kuimova, A. J. S. McIntosh and T. Welton, *Chem. Sci.*, 2020, **11**, 6121–6133.
34 H. Doan, S. L. Raut, D. Yale, M. Balaz, S. V. Dzyuba and Z. Gryczynski, *Chem. Commun.*, 2016, **52**, 9510–9513.
35 M. R. Dent, I. Lopez Duarte, C. J. Dickson, N. D. Geoghegan, J. M. Cooper, I. R. Gould, R. Krams, J. A. Bull, N. J. Brooks and M. K. Kuimova, *Phys. Chem. Chem. Phys.*, 2015, **17**, 18393–18402.
36 E. Gatzogiannis, Z. Chen, L. Wei, R. Wombacher, Y.-T. Kao, G. Yefremov, V. W. Cornish and W. Min, *Chem. Commun.*, 2012, **48**, 8694–8696.
37 M. K. Kuimova, S. W. Botchway, A. W. Parker, M. Balaz, H. A. Collins, H. L. Anderson, K. Suhling and P. R. Ogilby, *Nat. Chem.*, 2009, **1**, 69–73.
38 I. López-Duarte, T. T. Vu, M. A. Izquierdo, J. A. Bull and M. K. Kuimova, *Chem. Commun.*, 2014, **50**, 5282–5284.
39 Z. Yang, Y. He, J.-H. Lee, N. Park, M. Suh, W.-S. Chae, J. Cao, X. Peng, H. Jung, C. Kang and J. S. Kim, *J. Am. Chem. Soc.*, 2013, **135**, 9181–9185.
40 L. Wang, Y. Xiao, W. Tian and L. Deng, *J. Am. Chem. Soc.*, 2013, **135**, 2903–2906.
41 A. Polita, S. Toliautas, R. Žvirblis and A. Vyšniauskas, *Phys. Chem. Chem. Phys.*, 2020, **22**, 8296–8303.
42 Y. Wu, M. Štefl, A. Olzyńska, M. Hof, G. Yahioglu, P. Yip, D. R. Casey, O. Ces, J. Humpolíčková and M. K. Kuimova, *Phys. Chem. Chem. Phys.*, 2013, **15**, 14986–14993.
43 M. Olšinová, P. Jurkiewicz, M. Pozník, R. Šachl, T. Prausová, M. Hof, V. Kozmík, F. Teplý, J. Svobodab and M. Cebecauer, *Phys. Chem. Chem. Phys.*, 2014, **16**, 10688–10697.
44 S. Rebaud, O. Maniti and A. P. Girard-Egrot, *Biochimie*, 2014, **107**, 135–142.
45 M. Páez-Pérez, I. López-Duarte, A. Vyšniauskas, N. J. Brooks and M. K. Kuimova, *Chem. Sci.*, 2021, **12**, 2604–2613.
46 Y. Niko and A. S. Klymchenko, *J. Biochem.*, 2021, **170**, 163–174.
47 E. Sezgin, T. Gutmann, T. Buhl, R. Dirkx, M. Grzybek, Ü. Coskun, M. Solimena, K. Simons, I. Levental and P. Schwille, *PLoS One*, 2015, **10**, e0123930.
48 G. W. Feigenson, *Biochim. Biophys. Acta, Biomembr.*, 2009, **1788**, 47–52.
49 T. Róg, M. Pasenkiewicz-Gierula, I. Vattulainen and M. Karttunen, *Biochim. Biophys. Acta, Biomembr.*, 2009, **1788**, 97–121.

50 S. L. Veatch and S. L. Keller, *Biophys. J.*, 2003, **85**, 3074–3083.
51 S. D. Connell and D. A. Smith, *Mol. Membr. Biol.*, 2006, **23**, 17–28.
52 G. Preta, *Front. Cell Dev. Biol.*, 2020, **8**, 571237.
53 L. E Shimolina, A. A. Gulin, M. Paez-Perez, I. López-Duarte, I. N. Druzhkova, M. M. Lukina, M. V. Gubina, N. J. Brooks, E. V. Zagaynova, M. K. Kuimova and M. V. Shirmanova, *J. Biomed. Opt.*, 2020, **25**, 126004.
54 M. K. Kuimova, G. Yahioglu, J. A. Levitt and K. Suhling, *J. Am. Chem. Soc.*, 2008, **130**, 6672–6673.
55 L. S. C. Warren, A. Margineanu, D. Alibhai, D. J. Kelly, C. Talbot, Y. Alexandrov, I. Munro, M. Katan, C. Dunsby and P. M. W. French, *PLoS One*, 2013, **8**, e70687.

2nd publication

Bimodal effects on lipid droplets induced in cancer and non-cancer cells by chemotherapy drugs as revealed with a green-emitting BODIPY fluorescent probe

A. Polita, R. Žvirblis, J. Dodonova-Vaitkūnienė, A. P. Shivabalan, K. Maleckaitė, and G. Valinčius

Journal of Materials Chemistry B, 2024, 12, 3022–3030.

DOI: 10.1039/D3TB02979D

Author Contributions: Photophysical characterization of *BODIPY-LD* in solvents of varying viscosity and polarity; preparation of model membrane systems; fluorescence lifetime imaging experiments; analysis and interpretation of spectroscopic and imaging data; preparation of figures; and writing of the original manuscript draft.

Volume 12
Number 12
28 March 2024
Pages 2909–3164

Journal of Materials Chemistry B

Materials for biology and medicine

rsc.li/materials-b

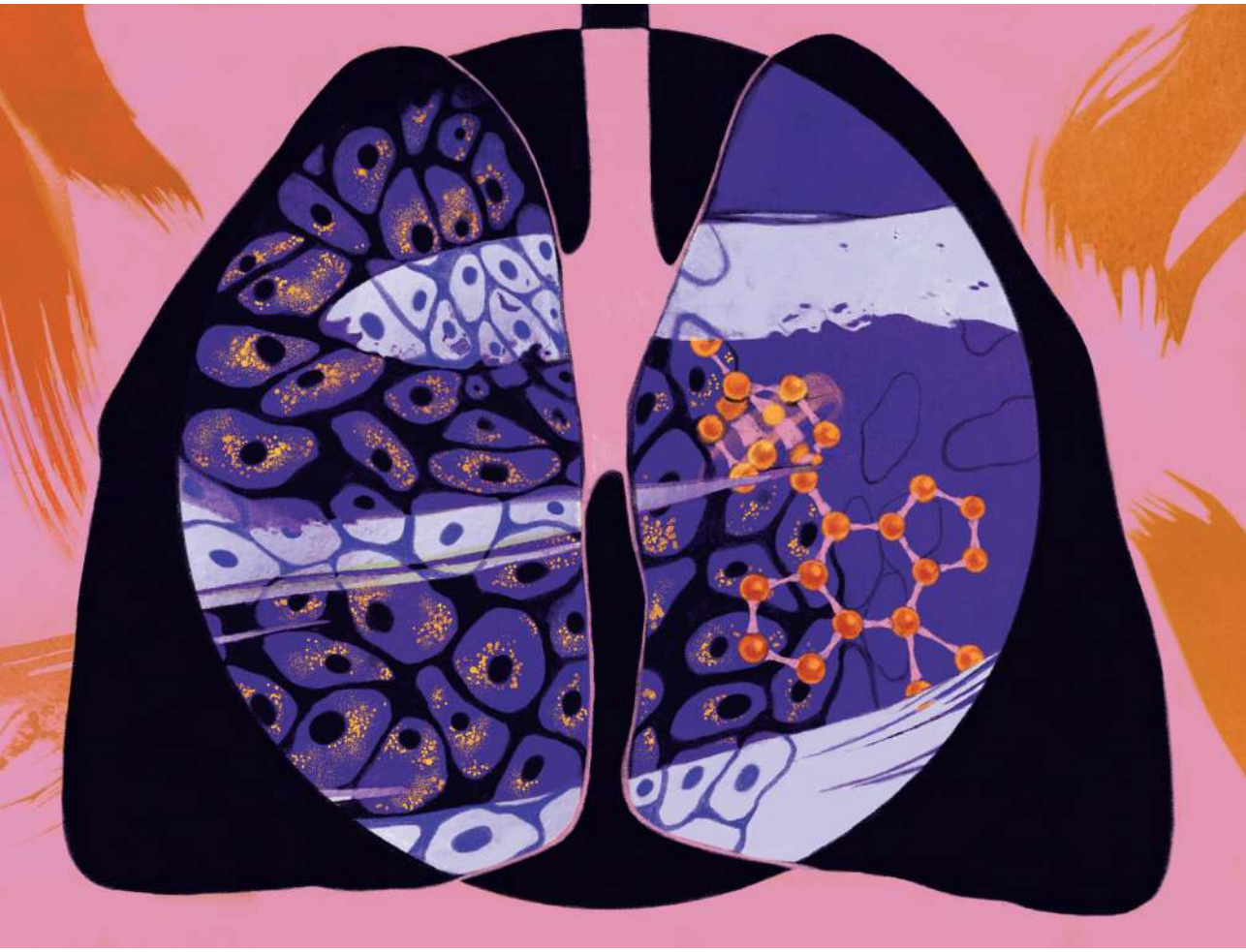

ISSN 2050-750X

ROYAL SOCIETY OF CHEMISTRY

PAPER

Artūras Polita *et al.*

Bimodal effects on lipid droplets induced in cancer and non-cancer cells by chemotherapy drugs as revealed with a green-emitting BODIPY fluorescent probe

Journal of Materials Chemistry B

ROYAL SOCIETY OF CHEMISTRY

PAPER

View Article Online
View Journal | View Issue

Cite this: J. Mater. Chem. B, 2024, 12, 3022

Bimodal effects on lipid droplets induced in cancer and non-cancer cells by chemotherapy drugs as revealed with a green-emitting BODIPY fluorescent probe†

Artūras Polita,[a]* Rokas Žvirblis,[b] Jelena Dodonova-Vaitkūnienė,[c] Arun Prabha Shivabalan,[a] Karolina Maleckaitė[d] and Gintaras Valinčius[a]

Received 18th December 2023,
Accepted 18th February 2024

DOI: 10.1039/d3tb02979d

rsc.li/materials-b

Lipid droplets (LDs) are cytoplasmic lipid-rich organelles with important roles in lipid storage and metabolism, cell signaling and membrane biosynthesis. Additionally, multiple diseases, such as obesity, fatty liver, cardiovascular diseases and cancer, are related to the metabolic disorders of LDs. In various cancer cells, LD accumulation is associated with resistance to cell death, reduced effectiveness of chemotherapeutic drugs, and increased proliferation and aggressiveness. In this work, we present a new viscosity-sensitive, green-emitting BODIPY probe capable of distinguishing between ordered and disordered lipid phases and selectively internalising into LDs of live cells. Through the use of fluorescence lifetime imaging microscopy (FLIM), we demonstrate that LDs in live cancer (A549) and non-cancer (HEK 293T) cells have vastly different microviscosities. Additionally, we quantify the microviscosity changes in LDs under the influence of DNA-damaging chemotherapy drugs doxorubicin and etoposide. Finally, we show that doxorubicin and etoposide have different effects on the microviscosities of LDs in chemotherapy-resistant A549 cancer cells.

Introduction

Lipid droplets (LDs) are dynamic lipid-rich organelles[1] composed of a neutral lipid hydrophobic core surrounded by a single layer of phospholipids decorated with various proteins (Fig. 1A).[2] Importantly, the composition of LDs and their size, localization and number change rapidly in response to cellular states and nutrient availability.[3,4] Not only do LDs function as lipid storage compartments,[5] but also play important roles in cell signalling and inflammation,[6,7] lipid metabolism[8] and membrane biosynthesis.[9] The metabolic disorders of LDs are related to multiple diseases, such as obesity,[10] fatty liver,[11] cardiovascular diseases,[12] and cancer.[13] Accumulation of LDs has been observed in cancer cells and cancerous tissues such as breast, prostate, and colorectal cancers, as well as hepatocellular and renal carcinomas.[14] In addition, LD accumulation also affects anti-cancer drug efficiency, alters their cellular distribution, and impairs drug-induced apoptosis and immunogenic cell death, causing chemotherapy resistance.[14,15] Moreover, LDs have been identified in all the processes involved in cancer development, including proliferation, evading growth suppressors, activating invasion and metastasis, evasion of immune destruction and resisting death.[1,15] On top of this, increased storage of lipids in LDs is also beneficial for cancer cell survival,[16,17] as additional lipids serve as energy sources to meet the metabolic needs of proliferating cancer cells. Conventional chemotherapeutic drugs have been shown to alter the fatty acid distribution in LDs, producing highly saturated LDs and unsaturated plasma membrane lipids.[18] Changes in the fatty acid distribution increase the amount of LDs and decrease the fluidity of the plasma membrane, potentially triggering the invasion and metastasis of cancer cells.[19] Importantly, LDs themselves may be appropriate targets for cancer chemotherapy,[1,20] and the elevated levels of LDs are used as a diagnostic biomarker for cancer.[14,21] Consequently, the ability to image the compositional changes of LDs may be particularly useful for the development of cancer diagnostic tools and studying the effects of chemotherapeutic agents on LDs.

Viscosity measurements provide a convenient way to observe the compositional changes that take place in LDs. The efficiency of lipid packaging and the order of lipids have a great

[a] Institute of Biochemistry, Life Sciences Center, Vilnius University, Saulėtekio av. 7, Vilnius, LT-10257, Lithuania. E-mail: arturas.polita@gmc.vu.lt
[b] Life Sciences Center, Institute of Biotechnology, Vilnius University, Saulėtekio av. 7, Vilnius, LT-10257, Lithuania
[c] Institute of Chemistry, Faculty of Chemistry and Geosciences, Vilnius University, Naugarduko st. 24, Vilnius, LT-03225, Lithuania
[d] Center of Physical Sciences and Technology, Saulėtekio av. 3, VilniusLT-10257, Lithuania

† Electronic supplementary information (ESI) available. See DOI: https://doi.org/10.1039/d3tb02979d

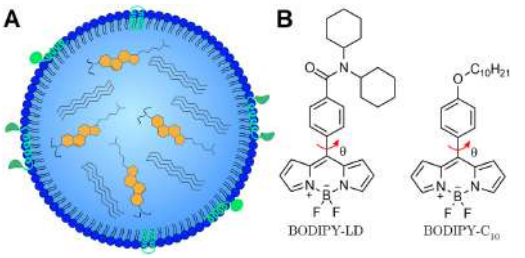

Fig. 1 (A) Simplified structure of the LD. (B) Structure of one of the most widely used molecular rotors – BODIPY-C10, and its variant for the detection of LDs – BODIPY-LD. The red arrows indicate the intramolecular rotation which causes BODIPY to display viscosity sensitivity.

influence on the viscosity values of lipid structures.[22] For example, cholesterol-rich lipid systems form highly viscous liquid-ordered (Lo) phases, whereas highly unsaturated lipids produce non-viscous liquid disordered (Ld) phases.[23] Moreover, the viscosity of the Ld phase is directly affected by the amount of cholesterol present in the bilayer.[24] The viscosity differences arising due to lipid packaging in the Lo and Ld phases allow for lipid order determination using fluorescent viscosity-sensitive probes.[25–27] LDs, depending on the cellular state, undergoing phase transitions from an ordered state to a disordered state have varying levels of cholesteryl esters and occasionally may feature ordered nanodomains in the centre.[28]

Viscosity-sensitive dyes, called molecular rotors, can be used to quantitatively image the microviscosity changes in LDs.[29,30] The term microviscosity here refers to the lipid packaging and molecular mobility of the probe's local environment.[31] In the excited state, molecular rotors undergo intramolecular rotation, which results in the molecular rotor entering the dark state.[32] In low viscosity or non-crowded environments, the intramolecular rotation is not restricted, and the non-radiative decay dominates, leading to a decrease in the fluorescence quantum yield and lifetime.[33] Using the fluorescence lifetime to quantify the microviscosity is particularly advantageous, since the lifetime is independent of the probe's concentration, excitation setup, and optical properties of the medium or the microscope. Molecular rotors can be combined with fluorescence lifetime imaging microscopy (FLIM) to create spatial microviscosity maps of different lipid structures in live cells.[34–36] Currently, BODIPY-C_{10} (Fig. 1B) is one of the most widely used molecular rotors for viscosity measurements.[37,38] Previously, BODIPY-C_{10} and its derivatives were used to quantify viscosity in model lipid bilayers,[39] plasma membranes,[40,41] mitochondria,[42] and lysosomes.[43] Due to its lack of specificity, BODIPY-C_{10} internalizes into various cellular membranes and the cytoplasm,[44] making LDs less detectable and data analysis more difficult.

Although fluorescence lifetime-based viscosity probes for LDs do exist (TPE-Cy and NLV-1),[45,46] to our knowledge, both these probes considerably stain the cytoplasm (and membrane-bound organelles in the case of TPE-Cy),[45] thus making LDs harder to identify. Despite the fact that both TPE-Cy and NLV-1 feature multiple rotating groups for increased viscosity sensitivity, their fluorescence lifetimes do not rise rapidly with increasing solvent viscosity, resulting in more challenging detection of minor microviscosity changes in live specimens.[45,46] The aim of this research is to explore the possibility of discriminating cancer and non-cancer cells based on the microviscosity of LDs. In this work, we introduce BODIPY-LD, a BODIPY-C_{10} derivative probe with high specificity for LDs and fluorescence lifetime-based ability to measure the microviscosity (Fig. 1B). By comparing fluorescence lifetimes of BODIPY-LD in solvents of different polarities and viscosities, we show that BODIPY-LD is affected mainly by the viscosity of the solvent. We explore the ability of BODIPY-LD to distinguish Lo and Ld phases in large unilamellar vesicles (LUVs) – one of the most frequently used model lipid systems. Furthermore, by using BODIPY-LD in combination with FLIM, we image LDs in human lung cancer cells (A549) and immortalised human embryonic kidney cells (HEK 293T). In addition, we investigate how DNA-damaging chemotherapeutic agents[47,48] – etoposide (ETP) and doxorubicin (DOX) – affect the microviscosities of LDs. Although both DOX and ETP cause DNA damage by poisoning enzyme topoisomerase II and converting it into a DNA-damaging agent,[47,48] DOX is additionally known for its ability to intercalate into DNA and generate free radicals, which can damage cellular membranes, DNA and proteins.[48] Numerous anticancer drugs have been reported to be sequestered in the hydrophobic cores of LDs.[1,16] However, studies investigating the physical changes that occur in LDs during chemotherapeutic treatment are still lacking. Our results demonstrate that the microviscosities of LDs in human lung cancer cells (A549) vary significantly between different cells in the same culture, but are similar within individual cells. In contrast, the microviscosities of LDs in human immortalised kidney cells (HEK 293T) are similar between different cells. We found that both DOX and ETP induce an increased number of LDs in both A549 and HEK 293T cells. Furthermore, DOX and ETP treatments of A549 cells induce the formation of both highly viscous and highly non-viscous LD populations within individual cells. In contrast, DOX treatment of HEK 293T cells produces LDs with varying microviscosities in individual cells, whereas ETP treatment induces the formation of LDs with uniform microviscosities within each cell. Finally, we show that highly viscous LDs are absent in DOX- and ETP-resistant A549 cells.

Results and discussion

Probe design

The BODIPY-LD design was based on one of the most applicable and successful rotors to date – BODIPY-C_{10}. In order to retain the same mechanism of the viscosity sensitivity of BODIPY-C_{10}, we decided to keep the rotation of the phenyl group *versus* the BODIPY unhindered and modified the *para*-position of the phenyl group. Our goal was to create a probe with high specificity for LDs with minimal cytoplasm staining. As a result, we introduced two cyclohexyl rings to increase the size and hydrophobicity of the probe, making the probe too

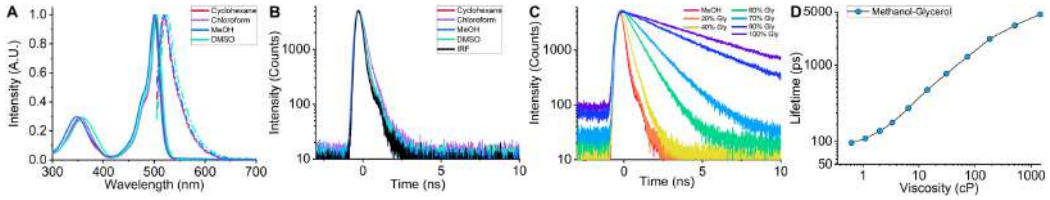

Fig. 2 (A) Fluorescence (dotted-dashed lines) and absorption (solid lines) spectra of BODIPY-LD obtained in cyclohexane, chloroform, methanol and DMSO. (B) Time-resolved fluorescence decay curves of BODIPY-LD in cyclohexane, chloroform, methanol and DMSO. (C) Time-resolved fluorescence decay curves of BODIPY-LD obtained in methanol–glycerol mixtures of varying viscosities. (D) Fluorescence lifetimes of BODIPY-LD in methanol–glycerol mixtures.

hydrophobic for cytoplasm staining (Fig. 1B). The non-charged nature of the probe should also favour its accumulation in neutral, lipid-rich environments. The synthesis of BODIPY-LD is described in the ESI.†

Absorption, steady-state and time-resolved fluorescence spectroscopies

In order to investigate the spectroscopic properties of BODIPY-LD, we performed absorption, steady-state, and time-resolved fluorescence experiments in solvents of varying polarity, from non-polar [cyclohexane] to very polar [DMSO] (Fig. 2). Similar to BODIPY-C_{10},[37] BODIPY-LD's absorption spectra include a low intensity band at 300–400 nm and the main band in the 450–525 nm region with maximum positioned at 500–505 nm (Fig. 2A). The fluorescence spectra of BODIPY-LD feature a slight red shift as the polarity of the solvent increases, from the fluorescence peak maximum at 518 nm in cyclohexane to 524 nm in DMSO (Fig. 2A). Importantly, no aggregation of the dye was observed in polar solvents such as methanol and DMSO. To explore the effects of solvent polarity on the fluorescence lifetimes of BODIPY-LD, we performed time-resolved fluorescence measurements in cyclohexane, toluene, chloroform, dichloromethane, DMSO and methanol (Fig. 2B and Fig. S1, ESI†). In all solvents tested, the fluorescence decay curves of BODIPY-LD were monoexponential, with fluorescence lifetimes ranging from 226 ps in chloroform to 153 ps in DMSO. In contrast, the fluorescence lifetimes of BODIPY-C_{10} range from 300 to 800 ps in the solvents of 0.5 cP viscosity.[40] We found no correlation between the polarity of the solvent and the fluorescence lifetimes of BODIPY-LD since the fluorescence decay curves differ marginally (Fig. 2B).

Next, we measured time-resolved and steady-state fluorescence of BODIPY-LD in methanol–glycerol mixtures that cover a viscosity range from 0.6 to 1457 cP to evaluate the probe's viscosity sensitivity and construct a fluorescence lifetime-viscosity calibration curve (Fig. 2C and Fig. S2, ESI†). The calibration curve can be utilized to convert the fluorescence lifetimes of BODIPY-LD in LDs into microviscosity values. The fluorescence lifetimes of BODIPY-LD range from 92 ps in methanol to 4639 ps in pure glycerol (Fig. 2D). The fluorescence decays were monoexponential for compositions ranging from methanol to 40% methanol-60% glycerol. At higher glycerol concentrations, the fluorescence decays become biexponential with low amplitude short lifetime components (Fig. S2, ESI†). Due to low fluorescence lifetime values in non-viscous solvents, BODIPY-LD has a significantly expanded dynamic viscosity range, which can be calculated from the lifetime ratio at high and low viscosities, compared to BODIPY-C_{10}. The dynamic range of BODIPY-LD in methanol–glycerol mixtures is 50.4, as determined from the ratio of fluorescence lifetimes in glycerol (4639 ps) and methanol (92 ps), compared to 11.2 for BODIPY-C_{10} in the same mixture.[37] These results demonstrate that the fluorescence lifetimes of BODIPY-LD are mainly affected by solvent viscosity and are minimally influenced by polarity.

Given that LDs contain varying amounts of cholesteryl esters and occasionally may feature ordered nanodomains,[28] we aimed to explore the ability of BODIPY-LD to integrate into highly viscous Lo phases, as well as probe's sensitivity to cholesterol and capability to distinguish Lo and Ld lipid phases. We carried out steady-state and time resolved fluorescence measurements on LUVs with Lo (DOPC:DPPC:Chol 1 : 5 : 5) and Ld (DOPC, POPC, DOPC:Chol) lipid phases (Fig. 3). While BODIPY-LD does not exhibit solvatochromism in the Ld phases, the steady-state fluorescence spectra display a slight red shift in the Lo phases, with peak maximum shifting from 521 (Ld) to 526 nm (Lo). (Fig. 3A). Notably, BODIPY-LD successfully integrates into both Lo and Ld LUVs and displays similar fluorescence intensity values in both phases (Fig. S3, ESI†). The ability of BODIPY-LD to partition into highly ordered lipid phases is highly important because LDs occasionally feature highly ordered lipid nanodomains[28] and undergo phase transitions from amorphous to the liquid crystalline lipid

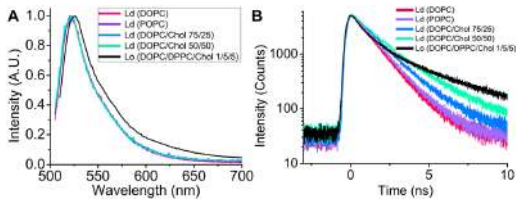

Fig. 3 (A) Steady-state fluorescence spectra of BODIPY-LD in Ld and Lo LUVs. (B) Time-resolved fluorescence spectra of BODIPY-LD in Ld and Lo LUVs.

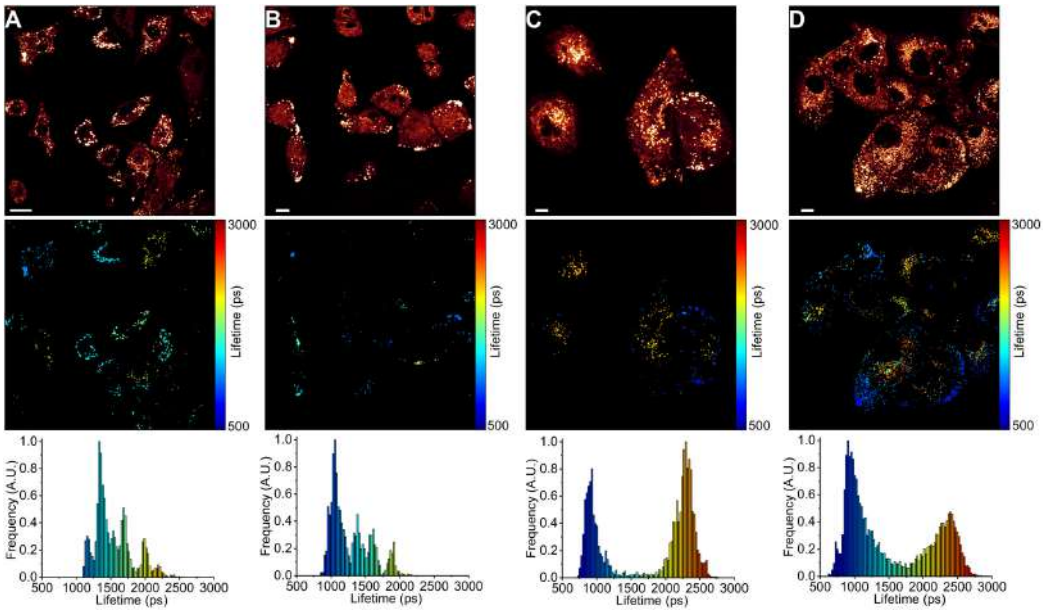

Fig. 4 FLIM images of BODIPY-LD in LDs of A549 cells. (A) A549 cells treated with DOX for 6 h. (B) A549 cells treated with DOX for 24 h. (C) A549 cells treated with DOX for 48 h. (D) The top panel shows images of fluorescence intensity. FLIM images are shown in the middle panel. The corresponding lifetime histograms are shown in the bottom panel. Scale bars are 10 μm.

phases.[49] The time-resolved fluorescence decays of BODIPY-LD in Lo LUVs are remarkably longer compared to the Ld LUVs (Fig. 3B), with biexponential intensity-weighted fluorescence lifetimes being 1.24, 1.3 and 3.6 ns for DOPC, POPC and DOPC:DPPC:Chol LUVs, respectively. We also examined how the cholesterol concentration in Ld LUVs affects the fluorescence lifetimes of BODIPY-LD. Cholesterol is especially known for its ability to induce order and condense Ld lipid bilayers.[50] Addition of cholesterol to DOPC LUVs (Ld) resulted in significantly longer fluorescence decays, with intensity weighted fluorescence lifetimes increasing from 1.24 ns for pure DOPC LUVs to 1.63 and 2.13 ns for DOPC/Chol 75/25 and DOPC/Chol 50/50 LUVs, respectively (Fig. 3B). We hypothesize that the biexponential nature of fluorescence decays in LUVs is likely caused by the different positions that the dye can occupy in the lipid bilayer. Most importantly, the ability to determine the lipid order and distinguish Lo and Ld phases based on the fluorescence lifetime of BODIPY-LD may be particularly useful for estimating the cholesterol levels in LDs, studying the biophysical changes induced in LDs upon binding of proteins, imaging ordering and disordering effects induced by small molecules, detecting the lipid phase transitions and observing the lipid exchange processes between LDs and organelles.

FLIM of LDs in human epithelial lung cancer (A549) and immortalised embryonic kidney (HEK 293T) cells

Next, we used FLIM to image LDs in human lung cancer (A549) and immortalised embryonic kidney (HEK 293T) cells (Fig. 4 and 5). BODIPY-LD very effectively stained both highly viscous and non-viscous LDs (1 μM concentration, 5 min), with negligible cytoplasm staining. Fluorescence intensities in the LDs were about 10^2 times higher than those in the cytoplasm. Curiously, BODIPY-LD did not stain the plasma membrane, allowing for an easy identification of peripheral LDs (Fig. 4 and 5). We hypothesize that poor plasma membrane staining is due to the highly lipophilic nature of the dye and a preference for the neutral lipid environments. The plasma membrane, on the other hand, features highly polar lipid headgroups, which give rise to higher dielectric constants in the lipid bilayer.[51] Notably, we did not observe any dye-induced morphology changes in the cells even when the concentration of BODIPY-LD was increased to 5 μM (Fig. S4, ESI†). Furthermore, we have confirmed that the spherical, slowly moving in the cytoplasm, vesicles (Fig. S5, ESI†) were indeed LDs by co-staining the cells with Nile Red – a well-known marker of LDs (Fig. S6, ESI†).[52] Additionally, we recorded the fluorescence spectra of LDs stained with BODIPY-LD to ensure that no aggregation of the dye occurs in the LDs and the fluorescence lifetimes are measured accurately (Fig. S7, ESI†).

Interestingly, in lung cancer cells (A549), we observed that the microviscosities of LDs vary significantly between individual cells within the same culture, with the intensity-weighted fluorescence lifetimes of BODIPY-LD ranging from 1100 to 2500 ps, corresponding to the viscosities of 60 to 270 cP in methanol–glycerol calibration mixtures (Fig. 4A and Fig. S8A, ESI†). Furthermore, the microviscosities of LDs in individual A549 cells were very similar (Fig. 4A and Fig. S8A, ESI†). In

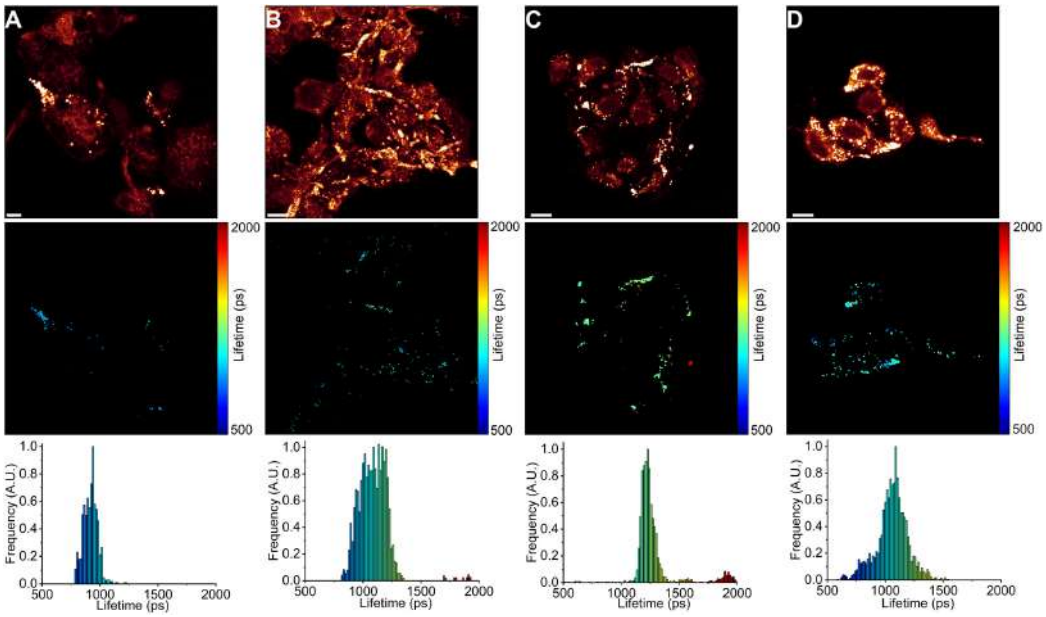

Fig. 5 FLIM images of BODIPY-LD in LDs of HEK 293T cells. (A) HEK 293T cells treated with DOX for 6 h. (B) HEK 293T cells treated with DOX for 24 h. (C) HEK 293T cells treated with DOX for 48 h. (D) The top panel shows images of fluorescence intensity. FLIM images are shown in the middle panel. The corresponding lifetime histograms are shown in the bottom panel. Scale bars are 10 μm.

contrast, LDs in human embryonic kidney cells (HEK 293T) possessed similar microviscosities in different cells, with the intensity-weighted fluorescence lifetimes of BODIPY-LD ranging from 700 to 1000 ps, corresponding to the viscosities of 25 and 50 cP in methanol–glycerol calibration mixtures (Fig. 5A and Fig. S9A, ESI†). In addition, the number of LDs in A549 cells far surpasses the number of LDs in HEK 293T (Fig. 4A and 5A). Most importantly, the large differences in fluorescence lifetimes between the cancerous and non-cancerous cells can be used for the detection of malignant cells. We hypothesize that the fluorescence lifetime differences, arising due to different viscosities of LDs, are representative of different cellular or metabolic states[3,53] in malignant cells and fluorescent environmental probes for LDs may be useful for the studies of cancer progression.

Next, we treated A549 and HEK 293T cells with half maximal inhibitory concentrations (IC_{50}) of anti-cancerous DNA-damaging drugs DOX (18 nM for A549 and 20 μM for HEK 293T)[54,55] and ETP (107 μM for A549 and 22 μM for HEK 293T).[55,56] The IC_{50} value represents the concentration of a drug capable of causing 50% cell death. We imaged LDs after 6, 24 and 48 hours of drug treatment. In both A549 and HEK 293T cells, DOX treatment gradually increased the number of LDs (Fig. 4 and 5). Similarly, ETP treatment of A549 and HEK 293T cells also resulted in a gradual increase in the number of LDs (Fig. S8 and S9, ESI†). Furthermore, after 24 and 48 h, DOX treatment of A549 cells slowly induced the formation of highly viscous and highly non-viscous LD populations within individual cells, with fluorescence lifetimes of BODIPY-LD ranging from 750 to 2600 ps, corresponding to the microviscosities of 30 and 300 cP (Fig. 4C and D). In addition, LDs with viscosities of about 90 cP (corresponding to BODIPY-LD fluorescence lifetimes of about 1500 ps) almost completely disappeared after 24 h of DOX treatment (Fig. 4C and D). Correspondingly, treatment of A549 cells with ETP also resulted in the disappearance of LDs with 90 cP viscosities after 24 h (Fig. S8, ESI†). Instead, highly viscous and highly non-viscous LD populations were formed, with viscosities ranging from 30 to 300 cP (Fig. S8, ESI†).

In contrast, the microviscosities of LDs in DOX-treated HEK 293T cells increased after 6 h from 25–50 cP to 25–70 cP (Fig. 5B) and a further 24 h treatment with DOX resulted in the formation of LDs with 60–70 cP viscosities (Fig. 5C). Additionally, some LDs had viscosities of 100 and 160 cP, corresponding to the fluorescence lifetimes of BODIPY-LD of 1500 ps and 2000 ps (Fig. 5C). Unlike in A549 cells, 48 h of DOX treatment in HEK 293T cells did not further increase the microviscosities of LDs; instead, heterogenous LD populations were present in all cells, with viscosities ranging from 25 to 70 cP (Fig. 5D). Finally, treatment of HEK 293T cells with ETP resulted in the formation of LDs with viscosities of 45–70 cP after 6 h (Fig. S9B, ESI†). Further 24 and 48 h treatment of HEK 293T cells with ETP produced LDs with viscosities ranging from 50 to 160 cP (Fig. S9C and D, ESI†). Curiously, after 24 h of ETP treatment, LDs in individual cells had more or less the same viscosities (Fig. S9C, ESI†).

We hypothesize that the increase in the number of LDs in cells undergoing DOX or ETP treatment is a result of cellular

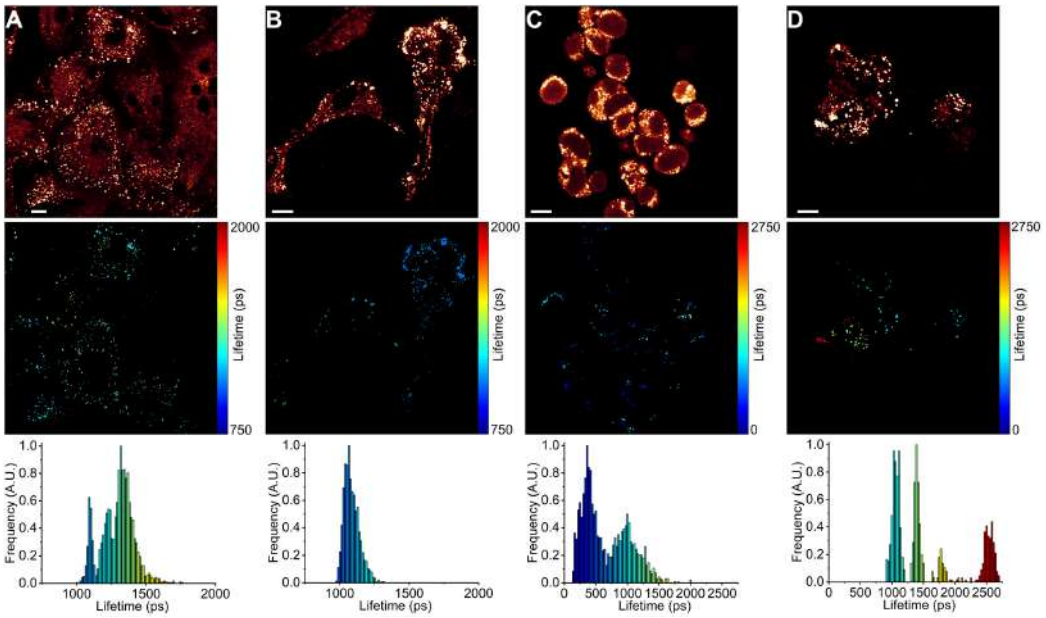

Fig. 6 FLIM images of BODIPY-LD in LDs of A549 cells treated with DOX ($2IC_{50}$) for 48 h. (A) A549 cells treated with ETP ($2IC_{50}$) for 48 h. (B) HEK 293T cells treated with DOX ($2IC_{50}$) for 48 h. (C) HEK 293T cells treated with ETP ($2IC_{50}$) for 48 h. (D) The top panel shows images of fluorescence intensity. FLIM images are shown in the middle panel. The corresponding lifetime histograms are shown in the bottom panel. Scale bars are 10 μm.

stress response.[17,57] Furthermore, cellular stress can induce the formation of highly hydrophobic LDs, which are likely enriched with cholesterol esters.[57] The increase in LD viscosity in A549 and HEK 293T cells upon DOX and ETP treatment may be due to the increased amount of cholesterol esters.[57] DOX and 5-fluorouracil have also been reported to alter the fatty acid distribution in LDs and induce the formation of highly saturated LDs in hepatocellular carcinoma and colorectal cancer cells.[18] We suspect that the presence of saturated fatty acids, as well as cholesteryl esters, promote the formation of highly ordered lipid phases[58] and account for the formation of viscous LDs after DOX and ETP treatments in A549 cells. However, we also observed non-viscous LDs in A549 cells upon DOX and ETP treatments. In addition, while DOX and ETP exerted similar effects on LDs in A549 cells, ETP treatment in HEK 293T cells produced moderately and highly viscous LDs, with the absence of non-viscous LDs, while DOX produced non-viscous and moderately viscous LDs.

FLIM of A549 and HEK 293T cells that are resistant to DOX and ETP treatment

Finally, we have quantified the microviscosities of LDs in A549 and HEK 293T cells that are resistant to chemotherapeutic drug treatment (Fig. 6). To perform this, we treated A549 and HEK 293T cells for 48 h with twice the IC_{50} concentrations of DOX (36 nM for A549 and 40 μM for HEK 293T) and ETP (214 μM for A549 and 44 μM for HEK 293T). Surprisingly, we found that DOX and ETP-resistant A549 and HEK 293T cells have LDs with very dissimilar microviscosities over their respective 48 h drug treatment (Fig. 6). With $2IC_{50}$ treatment of A549 cells with DOX, we no longer observed LDs with microviscosities of 30 and 300 cP; instead, LDs ranging from 60 to 100 cP were present (Fig. 6A). The $2IC_{50}$ treatment of A549 cells with ETP also resulted in the absence of LDs with microviscosities of 30 and 300 cP, but a very homogeneous population of LDs with microviscosities of about 50–65 cP was formed in each cell (Fig. 6B). In contrast, the $2IC_{50}$ treatment of HEK 293T cells with DOX induced the formation of LDs with moderate viscosities (25–90 cP), similar to IC_{50} DOX treatment (Fig. 6C). Of note, some LDs in HEK 293T cells treated with $2IC_{50}$ DOX concentrations displayed very low viscosities of about 10 cP (corresponding to the 300 ps fluorescence lifetime of BODIPY-LD). Similar to the IC_{50} treatment of HEK 293T cells with ETP, the $2IC_{50}$ treatment of HEK 293T cells with ETP resulted in the formation of LDs with homogeneous microviscosities in individual cells, with some cells having LD populations of 50, 90, 160 and 300 cP (Fig. 6D).

To summarize, DOX and ETP-resistant A549 cells possessed completely different LD populations compared to their corresponding IC_{50} treatments. The IC_{50} treatments of A549 cells with DOX and ETP resulted in very similar LD populations with high and low microviscosities in each cell. In contrast, DOX- and ETP-resistant A549 cells did not exhibit similar microviscosities of LDs. Instead, DOX-resistant cells possessed LDs with

heterogenous (60–100 cP) microviscosities, whereas ETP-resistant cells featured homogeneous LDs of 50–65 cP. On the other hand, DOX- and ETP-resistant HEK 293T cells possessed LDs with microviscosities similar to their respective 48 h IC_{50} treatments. However, while ETP-resistant A549 cells had LDs with homogeneous microviscosities, LDs in ETP-resistant HEK 293T cells showed highly variable microviscosities. Importantly, it appears that the microviscosities of LDs, and their lipid compositions in chemotherapy-resistant cells differ depending on drug treatment and cell type.

Conclusions

In conclusion, we have synthesised and explored the photophysical properties of a new BODIPY-based molecular rotor – BODIPY-LD. We showed that fluorescence decays of BODIPY-LD are sensitive to viscosity over a large range, from 0.5 to 1457 cP, and are minimally influenced by solvent polarity. Importantly, time-resolved fluorescence measurements on LUVs with Lo and Ld lipid phases demonstrate that BODIPY-LD possesses vastly different fluorescence lifetimes in lipid-ordered and lipid-disordered environments, allowing this probe to successfully distinguish lipid phase transitions and estimate the cholesterol concentrations in Ld phases. We found that BODIPY-LD preferentially partitions into the LDs of live cells without staining the cytoplasm or plasma membrane. Our results demonstrate that LDs in cancerous A549 and non-cancerous HEK 293T cells highly differ in their microviscosity, making the dye applicable as a diagnostic biomarker for cancer. Furthermore, the chemotherapeutic drugs DOX and ETP induce different microviscosity changes in LDs in cancerous and non-cancerous cells. Finally, we demonstrate that microviscosities of LDs in chemotherapy-resistant cells differ depending on the drug treatment and cell type.

Experimental section

Dyes, reagents, and solvents

The synthetic details of BODIPY-LD, with mass and NMR spectra, are presented in the ESI.† NMR spectra were recorded on a Bruker Ascend 400 spectrometer (400 MHz for ^{1}H, 100 MHz for ^{13}C, 128.4 MHz for ^{11}B, 376.5 MHz for ^{19}F). NMR spectra were referenced to residual solvent peaks. HRMS spectra were recorded on a quadrupole, time-of-flight mass spectrometer (microTOF-Q II, Bruker Daltonik GmbH, Germany). Column chromatography was performed using silica gel 60 (0.040–0.063 mm) (Merck). Thin layer chromatography (TLC) was performed using TLC-aluminium sheets with silica gel (Merck 60 F254). Visualisation was accomplished by UV light. Melting points were determined in open capillaries with a digital melting point IA9100 series apparatus (Thermo Fisher) and were not corrected. Reagents and solvents for the organic synthesis of the BODIPY compounds were purchased directly from commercial suppliers; solvents were purified by known procedures. Stock solutions of 1 mM BODIPY-LD were prepared in methanol or DMSO and diluted for further experiments in solvents or their mixtures. All solvents used were spectroscopic grade obtained from Sigma Aldrich. DOPC, POPC, DPPC, and cholesterol were obtained from Avanti Polar Lipids. DOX and ETP were obtained from Sigma Aldrich, and 10 mM stock solutions of DOX and ETP were prepared in DMSO and diluted for subsequent experiments.

Formation of LUVs

LUVs were prepared by mixing lipids in appropriate ratios; afterwards, BODIPY-LD was added to the mixture with a dye to lipid ratio of 1 : 800, and chloroform was evaporated under a nitrogen stream for at least 2 hours. After evaporation, PBS buffer was added on top of the film. The total concentration of lipids in the PBS solution was 1 mM. In the case of DOPC/DPPC/Chol (1/5/5) LUVs, PBS buffer was heated to 60 °C. After resuspension, mixtures were placed in an ultrasonic bath (1 h) and extruded through 100 nm polycarbonate membranes with a syringe extruder (Avanti Polar Lipids). Extrusions were performed above the melting temperature of the lipids.

Absorption, steady-state, and time-resolved fluorescence spectroscopies

Absorption spectra were measured using a Jasco V-670 spectrophotometer. Fluorescence spectra were recorded with an Edinburgh-F900 (Edinburgh Instruments) fluorimeter using an Fianum white laser, together with bandpass filters (Thorlabs), emitting at 488 nm as an excitation source. Fluorescence decays were measured using time-correlated single-photon counting (TCSPC). Fluorescence decays had 5000 counts at the peak of the decay with 20 ns time window being used with 4096 channels in the time domain. 10 mm quartz cuvettes were used for absorption and fluorescence measurements with a BODIPY-LD concentration up to 2 μM. Fluorescence decays of BODIPY-LD in solvent mixtures and pure solvents were taken at 20 °C.

Imaging of live cells

Cell imaging experiments were performed using the human lung cancer A549 and immortalized human embryonic kidney HEK 293T cell lines (ATCC). The cells were cultured in Dulbecco's modified Eagle's medium (DMEM) supplemented with 10% foetal bovine serum (FBS), 100 IU mL^{-1} penicillin and 100 μg mL^{-1} streptomycin (Thermo Fisher). The cells were incubated at 37 °C with 5% CO_2. Before imaging, cells were seeded into Ibidi μ-Dish (Ibidi) at a seeding density of 10 000 cells mL^{-1} and allowed to grow for 24 hours. For cell imaging, 1 μM of BODIPY-LD solution (in DMSO) was added to the culture medium for 5 min at 37 °C. FLIM imaging was performed using a Leica SP8 microscope with a 63× objective (HC PL APO oil immersion, N.A. – 1.4, Leica).

Fluorescence lifetime imaging microscopy (FLIM)

FLIM was performed with a Leica SP8 microscope using a 63× objective (HC PL APO oil immersion, N.A. – 1.4, Leica). The fluorescence decay signal was measured over the 505–550 nm range using a 488 nm filter-supported white light laser excitation line. The FLIM images were produced in a

512 × 512 pixel resolution with 128 channels in the time domain, and pixels were binned to have at least 1000 counts at the peak of the decay curve for reliable biexponential fitting. Only lipid droplet-containing pixels in FLIM images were fitted. Lipid droplets were identified based on their 100-fold greater fluorescence counts per pixel relative to the cytoplasm. The instrument response function (IRF) was measured by recording the laser reflection signal off a glass coverslip.

Data analysis

FLIM images were analysed with FLIMFIT software (v4.6.1, Imperial College London).[59] The biexponential fluorescence decay model with intensity-weighted mean lifetimes was applied for both FLIM and fluorimeter time-correlated single photon counting (TCSPC) measurements:

$$\tilde{\tau} = \frac{\sum_i a_i \tau_i^2}{\sum_i a_i \tau_i}$$

where a_i and τ_i are the amplitudes of the individual components. The goodness-of-fit parameter (χ^2) was 1.3 or less for both FLIM images and fluorimeter TCSPC decays. Fluorimeter TCSPC decays of BODIPY-LD were fitted using the Edinburgh-F900 software package F900.

Conflicts of interest

The authors declare no conflicts of interest.

Notes and references

1 A. L. S. Cruz, E. D. A. Barreto, N. P. B. Fazolini, J. P. B. Viola and P. T. Bozza, *Cell Death Dis.*, 2020, **11**, 105.
2 J. A. Olzmann and P. Carvalho, *Nat. Rev. Mol. Cell Biol.*, 2019, **20**, 137–155.
3 A. R. Thiam and M. Beller, *J. Cell Sci.*, 2017, **130**, 315–324.
4 A. Herms, M. Bosch, B. J. N. Reddy, N. L. Schieber, A. Fajardo, C. Ruperez, A. Fernandez-Vidal, C. Ferguson, C. Rentero, F. Tebar, C. Enrich, R. G. Parton, S. P. Gross and A. Pol, *Nat. Commun.*, 2015, **6**, 7176.
5 C.-W. Wang, *Biochim. Biophys. Acta*, 2016, **1861**, 793–805.
6 C. Cheng, F. Geng, X. Cheng and D. Guo, *Cancer Commun.*, 2018, **38**, 1–14.
7 J. E. Norman, H. H. Aung, D. W. Wilson and J. C. Rutledge, *Food Funct.*, 2018, **9**, 6245–6256.
8 T. C. Walther and R. V. Farese, *Annu. Rev. Biochem.*, 2012, **81**, 687–714.
9 C. F. Kurat, H. Wolinski, J. Petschnigg, S. Kaluarachchi, B. Andrews, K. Natter and S. Kohlwein, *Mol. Cell*, 2009, **33**, 53–63.
10 S. Xu, X. Zhang and P. Liu, *Biochim. Biophys. Acta - Mol. Basis Dis.*, 2018, **1864**, 1968–1983.
11 N. L. Gluchowski, M. Becuwe, T. C. Walther and R. V. Farese, *Nat. Rev. Gastroenterol. Hepatol.*, 2017, **14**, 343–355.
12 H. Wang, M. Lei, R.-C. Hsia and C. Sztalryd, *Methods Cell Biol.*, 2013, **116**, 129–149.
13 H. Abramczyk, J. Surmacki, M. Kopeć, A. K. Olejnik, K. Lubecka-Pietruszewska and K. Fabianowska-Majewska, *Analyst*, 2015, **140**, 2224–2235.
14 Z. Li, H. Liu and X. Luo, *Am. J. Cancer Res.*, 2020, **10**, 4112–4122.
15 C. Jin and P. Yuan, *Oncol. Lett.*, 2020, **20**, 2091–2104.
16 Y. Jin, Y. Tan, J. Wu and Z. Ren, *Cell Death Discovery*, 2023, **9**, 254.
17 A. Zadoorian, X. Du and H. Yang, *Nat. Rev. Endocrinol.*, 2023, **19**, 443–459.
18 A. Mehdizadeh, M. Bonyadi, M. Darabi, R. Rahbarghazi, S. Montazersaheb, K. Velaei, M. Shaaker and M.-H. Somi, *Bioimpacts*, 2017, **7**, 31–39.
19 V. Ajdzanovic, M. Mojic, D. Maksimovic-Ivanic, M. Bulatovic, S. Mijatovic, V. Milosevic and I. Spasojevic, *J. Membr. Biol.*, 2013, **246**, 307–314.
20 Y. Wang, H. Pan, D. Chen, D. Guo and X. Wang, *J. Funct. Foods*, 2021, **83**, 104570.
21 F. Geng and D. Guo, *Int. Med. Rev.*, 2017, **3**, 10.
22 Y. Wu, M. Štefl, A. Olzyńska, M. Hof, G. Yahioglu, P. Yip, D. R. Casey, O. Ces, J. Humpolíčková and M. K. Kuimova, *Phys. Chem. Chem. Phys.*, 2013, **15**, 14986–14993.
23 J. Zidar, F. Merzel, M. Hodošček, K. Rebolj, K. Sepčić, P. Maček and D. Janežič, *J. Phys. Chem. B*, 2009, **113**, 15795–15802.
24 O. G. Mouritsen and M. J. Zuckermann, *Lipids*, 2004, **39**, 1101–1113.
25 M. R. Dent, I. López-Duarte, C. J. Dickson, N. D. Geoghegan, J. M. Cooper, I. R. Gould, R. Krams, J. A. Bull, N. J. Brooks and M. K. Kuimova, *Phys. Chem. Chem. Phys.*, 2015, **17**, 18393–18402.
26 M. R. Dent, I. López-Duarte, C. J. Dickson, P. Chairatana, H. L. Anderson, I. R. Gould, D. Wylie, A. Vyšniauskas, N. J. Brooks and M. K. Kuimova, *Chem. Commun.*, 2016, **52**, 13269–13272.
27 M. Páez-Pérez, I. López-Duarte, A. Vyšniauskas, N. J. Brooks and M. K. Kuimova, *Chem. Sci.*, 2021, **12**, 2604–2613.
28 J. Mahamid, D. Tegunov, A. Maiser, J. Arnold, H. Leonhardt, J. M. Plitzko and W. Baumeister, *Proc. Natl. Acad. Sci. U. S. A.*, 2019, **116**, 16866–16871.
29 H. Chen, J. Zhao, J. Lin, B. Dong, H. Li, B. Geng and M. Yan, *RSC Adv.*, 2021, **11**, 8250–8254.
30 C. W. Song, U. Tamima, Y. J. Reo, M. Dai, S. Sarkar and K. H. Ahn, *Dyes Pigm.*, 2019, **171**, 107718.
31 M. R. Bittermann, M. Grzelka, S. Woutersen, A. M. Brouwer and D. Bonn, *J. Phys. Chem. Lett.*, 2021, **12**, 3182–3186.
32 M. K. Kuimova, *Phys. Chem. Chem. Phys.*, 2012, **14**, 12671–12686.
33 S.-C. Lee, J. Heo, H. C. Woo, J.-A. Lee, Y. H. Seo, C.-L. Lee, S. Kim and O.-P. Kwon, *Chem. – Eur. J.*, 2018, **24**, 13706–13718.
34 M. Kubánková, I. López-Duarte, D. Kiryushko and M. K. Kuimova, *Soft Matter*, 2018, **14**, 9466–9474.

35 P. S. Sherin, I. López-Duarte, M. R. Dent, M. Kubánková, A. Vyšniauskas, J. A. Bull, E. S. Reshetnikova, A. S. Klymchenko, Y. P. Tsentalovich and M. K. Kuimova, *Chem. Sci.*, 2017, **8**, 3523–3528.
36 T. Mukherjee, R. J. Martinez-Sanchez, K. T. Fam, S. Bou, L. Richert, D. Garnier, Y. Mély, S. Kanvah, A. S. Klymchenko and M. Collot, *Mater. Chem. Front.*, 2021, **5**, 2459–2469.
37 A. Polita, S. Toliautas, R. Žvirblis and A. Vyšniauskas, *Phys. Chem. Chem. Phys.*, 2020, **22**, 8296–8303.
38 A. Vyšniauskas, M. Qurashi, N. Gallop, M. Balaz, H. L. Anderson and M. K. Kuimova, *Chem. Sci.*, 2015, **6**, 5773–5778.
39 A. Polita, M. Stancikaitė, R. Žvirblis, K. Maleckaitė, J. Dodonova-Vaitkūnienė, S. Tumkevičius, A. P. Shivabalana and G. Valinčius, *RSC Adv.*, 2023, **13**, 19257–19264.
40 I. López-Duarte, T. T. Vu, M. A. Izquierdo, J. A. Bull and M. K. Kuimova, *Chem. Commun.*, 2014, **50**, 5282–5284.
41 J. T. Mika, A. J. Thompson, M. R. Dent, N. J. Brooks, J. Michiels, J. Hofkens and M. K. Kuimova, *Biophys. J.*, 2016, **111**, 1528–1540.
42 Z. Yang, Y. He, J.-H. Lee, N. Park, M. Suh, W.-S. Chae, J. Cao, X. Peng, H. Jung, C. Kang and J. S. Kim, *J. Am. Chem. Soc.*, 2013, **135**, 9181–9185.
43 L. Wang, Y. Xiao, W. Tian and L. Deng, *J. Am. Chem. Soc.*, 2013, **135**, 2903–2906.
44 J. A. Levitt, M. K. Kuimova, G. Yahioglu, P.-H. Chung, K. Suhling and D. Phillips, *J. Phys. Chem. C*, 2009, **113**, 11634–11642.
45 S. Chen, Y. Hong, Y. Zeng, Q. Sun, Y. Liu, E. Zhao, G. Bai, J. Qu, J. Hao and B. Z. Tang, *Chem. – Eur. J.*, 2015, **21**, 4315–4320.
46 R. Guo, J. Yin, Y. Ma, G. Li, Q. Wang and W. Lin, *Sens. Actuators, B*, 2018, **271**, 321–328.
47 V. Singh, P. Johansson, E. Ekedahl, Y.-L. Lin, O. Hammarsten and F. Westerlund, *Biochem. Biophys. Res. Commun.*, 2022, **594**, 57–62.
48 C. F. Thorn, C. Oshiro, S. Marsh, T. Hernandez-Boussard, H. McLeod, T. E. Klein and R. B. Altmana, *Pharmacogenet. Genomics*, 2011, **21**, 440–446.
49 I. A. Windham and S. Cohen, *J. Cell Biol.*, 2022, **221**, e202210008.
50 T. Róg, M. Pasenkiewicz-Gierula, I. Vattulainen and M. Karttunen, *Biochim. Biophys. Acta, Biomembr.*, 2009, **1788**, 97–121.
51 G. Gramse, A. Dols-Perez, M. A. Edwards, L. Fumagalli and G. Gomila, *Biophys. J.*, 2013, **104**, 1257–1262.
52 S. I. Suarez, C. C. Warner, H. Brown-Harding, A. M. Thooft, B. VanVeller and J. C. Lukesh III, *Org. Biomol. Chem.*, 2020, **18**, 495–499.
53 T. C. Walther, J. Chung and R. V. Farese, *Annu. Rev. Cell Dev. Biol.*, 2017, **33**, 491–510.
54 R. Punia, K. Raina, R. Agarwal and R. P. Singh, *PLoS One*, 2017, **12**, e0182870.
55 V. Chaudhary, S. Das, A. Nayak, S. K. Guchhait and C. N. Kundu, *RSC Adv.*, 2015, **5**, 26051–26060.
56 F. M. Siswanto, A. Tamura, R. Sakuma and S. Imaoka, *Mol. Pharmacol.*, 2022, **101**, 257–273.
57 A. E. Ventura, S. Pokorna, N. Huhn, T. C. B. Santos, M. Prieto, A. H. Futerman and L. C. Silva, *Biochim. Biophys. Acta, Mol. Cell Biol. Lipids*, 2023, **1868**, 159347.
58 L. J. Pike, *J. Lipid Res.*, 2003, **44**, 655–667.
59 L. S. C. Warren, A. Margineanu, D. Alibhai, D. J. Kelly, C. Talbot, Y. Alexandrov, I. Munro, M. Katan, C. Dunsby and P. M. W. French, *PLoS One*, 2013, **8**, e70687.

3rd publication

Cancer cell identification via lysosomal membrane microviscosities using a green-emitting BODIPY molecular rotor

R. Bagdonaitė, R. Žvirblis, J. Dodonova-Vaitkūnienė, and **A. Polita**

JACS Au, 2024, 5, 2004–2014.

DOI: 10.1021/jacsau.5c00253

Author Contributions: Photophysical characterization of *BODIPY-Lys* in solvents of varying viscosity and polarity; fluorescence lifetime imaging experiments; analysis and interpretation of spectroscopic and imaging data; preparation of figures; and writing of the original manuscript draft.

JACS Au
AN OPEN ACCESS JOURNAL OF THE AMERICAN CHEMICAL SOCIETY

pubs.acs.org/jacsau
Article

Cancer Cell Identification via Lysosomal Membrane Microviscosities Using a Green-Emitting BODIPY Molecular Rotor

Rūta Bagdonaitė, Rokas Žvirblis, Jelena Dodonova-Vaitkūnienė, and Artūras Polita*

Cite This: JACS Au 2025, 5, 2004−2014

ABSTRACT: Lysosomes are dynamic, membrane-bound organelles that play key roles in cellular waste disposal, macromolecule recycling, and signaling. Disruptions in lysosomal function and lipid composition are implicated in a wide range of diseases including lysosomal storage disorders, fatty liver disease, atherosclerosis, and cancer. Imaging of the lysosomal lipid composition has the potential to not only enhance the understanding of lysosome-related diseases and their progression but also help identify them. In this work, we present a novel viscosity-sensitive, green-emitting BODIPY probe that can distinguish between ordered and disordered lipid phases and selectively internalize into the lysosomal membranes of live cells. Through the use of fluorescence lifetime imaging microscopy, we demonstrate that lysosomal membranes in multiple cancer cells exhibit significantly higher microviscosities compared to noncancer cells. The differences in lysosomal microviscosities provide an effective approach for identifying cancer cells and indicate that malignant cells may possess more oxidized and saturated lysosomal lipid membranes. Furthermore, we demonstrate the utility of viscosity-sensitive probes in quantifying the compositional changes in lysosomal membranes by investigating the effects of lysosome-permeabilizing cationic amphiphilic drugs (CADs), sertraline, and astemizole. Our results reveal that despite their functional similarities, these CADs exert opposite effects on lysosomal microviscosities in both cancerous and noncancerous cells, suggesting that different mechanisms may contribute to the CAD-induced lysosomal damage and leakage.

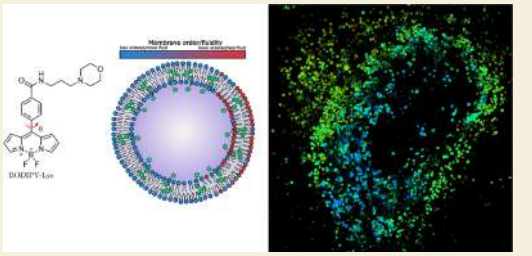

KEYWORDS: *lysosomes, microviscosity, lipids, BODIPY, FLIM, cancer*

1. INTRODUCTION

Since their discovery, lysosomes have been predominantly associated with the waste disposal and recycling of macromolecules.[1] Today, however, lysosomes are recognized as versatile signaling organelles with a variety of cellular functions that are required not only for normal cell survival[1] but also for malignant transformation and cancer progression.[2,3] Lysosomes not only provide cancer cells with energy and building blocks but also directly contribute to several common cancer traits, such as growth signaling, metastasis, angiogenesis, cell division, and drug resistance.[4] To meet the altered metabolic and survival requirements brought about by malignant transformation, lysosomes undergo morphological and compositional changes during cancer progression.[5,6] Most aggressive cancers feature enlarged lysosomal volume and more peripheral localization of the lysosomes.[6,7] Furthermore, malignant transformations compromise the stability of lysosomal membranes due to various metabolic and signaling abnormalities that increase the production of ROS, which in turn oxidize and destabilize lysosomal membrane lipids.[8] Since oxidized lipids feature a greater number of hydrogen bonds in the hydrophobic core of the bilayer, such lipid bilayers are more tightly packed and hence more ordered.[9−11] Additionally, malignant cells typically contain elevated quantities of saturated lipids,[12,13] which often increase the lipid order of biological membranes.[14] In addition to cancer, changes in lysosomal lipid composition and the accumulation of cholesterol within lysosomes are also observed in conditions like atherosclerosis,[15] lysosomal storage diseases,[16] and fatty liver disease.[17] Consequently, the ability to assess lysosomal membrane lipid order could not only aid in identifying cancer cells and provide insights into tumor aggressiveness but also offer valuable information for research into atherosclerosis, lysosomal storage diseases, and fatty liver disease. Additionally, emerging evidence suggests that cancer cells frequently acquire mutations that allow them to evade therapy-induced apoptosis while becoming vulnerable to lysosome-dependent cell death,

Received: March 5, 2025
Revised: April 2, 2025
Accepted: April 3, 2025
Published: April 14, 2025

https://doi.org/10.1021/jacsau.5c00253
JACS Au 2025, 5, 2004−2014

which proceeds upon permeabilization of lysosomal membranes.[6] Notably, lysosome-dependent cell death operates independently of caspase activation and may be particularly effective in treating apoptosis-resistant cancers.[6] A number of clinically approved cationic amphiphilic drugs (CADs), commonly used to treat neurological disorders, have been shown to induce lysosomal membrane permeabilization and trigger lysosomal-dependent cell death.[18] Lysosomal membrane permeabilization here refers to the release of lumenal contents into the cytosol, potentially leading to lysosome-dependent cell death.[19] CADs typically contain one or more amine groups that can be protonated at physiological pH, causing them to accumulate within lysosomes.[20] This accumulation disrupts the cancer-promoting and cancer-supporting roles of lysosomes[21,22] and destabilizes lysosomal membranes,[18,21,22] opening promising possibilities for treating chemotherapy-resistant cancers. While numerous studies have explored the inhibitory effects of CADs on various enzymes involved in lysosomal membrane permeabilization,[18,20,21] the precise impact of CADs on the lipid order of lysosomal membranes, which likely affects membrane permeabilization, remains unclear. Furthermore, although structurally different CADs demonstrate similar effects on lysosomal permeabilization and protein inhibition,[23] it is still unknown whether different CADs have comparable or distinct effects on the lipid packaging characteristics of lysosomal membranes.

Microviscosity measurements provide one of the most convenient ways to track compositional changes in lysosomal membranes as the microviscosity values are highly influenced by lipid packing efficiency and lipid order.[10,24,25] For instance, cholesterol-rich bilayers form highly viscous, liquid-ordered lipid phases, while highly unsaturated lipids produce non-viscous and liquid-disordered lipid phases.[26,27] The term microviscosity here refers to the lipid packaging and molecular mobility of the probe in the local environment. Viscosity-sensitive dyes, known as molecular rotors, can quantify microviscosity changes produced by cholesterol variations or lipid phase separations, making them valuable for studying compositional changes in lipid systems.[28−30] In the excited state, molecular rotors can undergo intramolecular rotation, resulting in a molecular rotor entering the dark state.[30,31] Thus, in low-viscosity environments or disordered lipid bilayers, the intramolecular rotation of the rotor is not hindered, and nonradiative decay dominates, resulting in a decrease in the fluorescence quantum yield and lifetime.[32] In contrast, in high-viscosity environments or ordered lipid bilayers, the intramolecular rotation is inhibited, leading to increased fluorescence lifetimes.[32] When paired with fluorescence lifetime imaging microscopy (FLIM), molecular rotors can produce spatial microviscosity maps of lipid structures, revealing dynamic changes in the lipid bilayer composition.[33−36] Many successful BODIPY-based lysosome-targeting viscosity probes, such as Lyso-V[37] and Lyso-B,[38] incorporate an electron-rich morpholine group near the BODIPY core. This design causes fluorescence quenching via photoinduced electron transfer (PET) at neutral or basic pH levels. While PET effectively ensures that the probe is fluorescent only in acidic lysosomes, it limits the detection of lysosomes in pathological conditions, where elevated pH levels are common.[39,40] Moreover, the morpholine's proximity to the BODIPY core in probes such as Lyso-V interferes with the molecular rotor's viscosity-sensing mechanism, reducing its sensitivity to viscosity changes.[37]

The aim of this research is to explore the potential for identifying cancer and noncancer cells based on lysosomal membrane microviscosity and to demonstrate the broad applicability of microviscosity measurements in evaluating the effects of lysosome-targeting chemotherapeutic drugs. To the best of our knowledge, no studies to date have investigated the possibility of using lysosomal membrane fluidity as a biomarker for cancer detection. In this work, we introduce BODIPY-Lys, a BODIPY-C_{10} derivative with high specificity for lysosomes and a fluorescence lifetime-based ability to measure the microviscosity of lysosomal membranes. We explore the photophysical properties of BODIPY-Lys and demonstrate that the fluorescence lifetime of BODIPY-Lys is mainly affected by the viscosity and not the polarity or temperature of the environment. Using BODIPY-Lys in combination with FLIM, we image lysosomal microviscosities in four distinct human cancerous and noncancerous cell lines. Our results reveal that lysosomal membrane microviscosities in cancerous cells are about three times higher compared to noncancerous cells, indicating that the biophysical properties of lysosomal membranes could serve as a biomarker for malignancy detection. Finally, we assess the effects of two commonly used CADs, sertraline (Ser) and astemizole (Ast), on lysosomal membrane microviscosities in both cancerous and noncancerous cell lines. Although Ser and Ast share similar mechanisms for inducing lysosomal membrane permeabilization, microviscosity measurements show that both CADs have opposite effects on lipid bilayer fluidity in cancerous cell lines.

2. RESULTS AND DISCUSSION

2.1. Probe Design

The design of BODIPY-Lys is based on one of the most widely used and successful molecular rotors to date, BODIPY-C_{10}. To retain the viscosity-sensitive mechanism of BODIPY-C_{10}, we preserved the rotation of the phenyl group relative to the BODIPY core unhindered and modified the para-position of the phenyl group by introducing a morpholine group (Figure 1A). The morpholine group provides BODIPY-Lys with reasonable water solubility and becomes protonated only in the acidic environment of the lysosomes, leading to the gradual accumulation of BODIPY-Lys in these organelles. The distant placement of the morpholine group from the BODIPY core prevents PET from occurring and enables the detection of

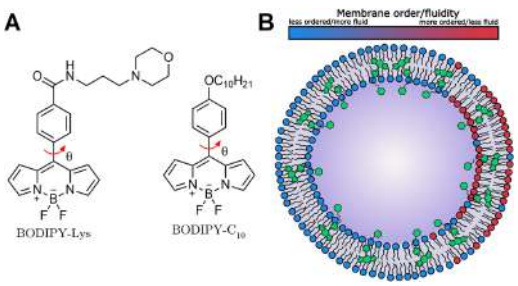

Figure 1. (A) Structures of one of the most widely used molecular rotors, BODIPY-C10, and its variant for lysosomes, BODIPY-Lys. Red arrows indicate intramolecular rotation, which causes BODIPY to display viscosity sensitivity. (B) Supposed positioning of BODIPY-Lys in the lysosomal membrane.

https://doi.org/10.1021/jacsau.5c00253
JACS Au 2025, 5, 2004−2014

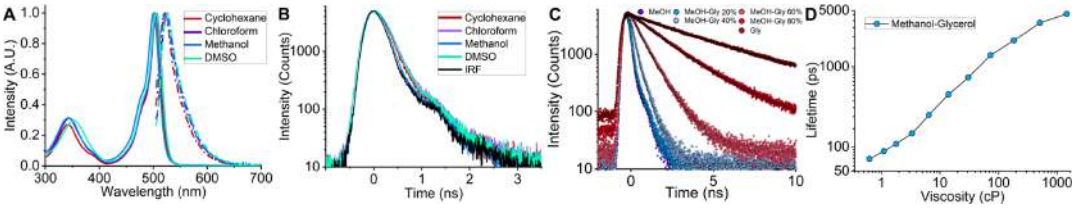

Figure 2. Photophysical characterization of BODIPY-Lys. (A) Fluorescence (dotted-dashed lines) and absorption (solid lines) spectra of BODIPY-Lys obtained in cyclohexane, chloroform, DMSO, and methanol. (B) Time-resolved fluorescence decays of BODIPY-Lys in cyclohexane, chloroform, DMSO, and methanol. (C) Time-resolved fluorescence decays of BODIPY-Lys obtained in methanol−glycerol mixtures of varying viscosities. (D) Fluorescence lifetimes of BODIPY-Lys in methanol−glycerol mixtures.

lysosomes with elevated pH levels. The hydrophobic core of BODIPY, along with the phenyl ring, likely integrates into the lysosomal lipid membrane, while the protonated morpholine group keeps the probe anchored to the inner leaflet of the lipid bilayer (Figure 1B). The synthesis of BODIPY-Lys is described in the electronic Supporting Information.

2.2. Absorption, Steady-State, and Time-Resolved Fluorescence

To investigate the photophysical characteristics of BODIPY-Lys, we performed absorption, steady-state, and time-resolved fluorescence measurements in solvents with varying polarities, from nonpolar cyclohexane to polar DMSO (Figure 2). Since lysosomal membranes contain substantial amounts of proteins and carbohydrates,[41] a lipid order probe must remain insensitive to environmental polarity to accurately measure the microviscosity of the protein-rich lipid bilayer. Similar to BODIPY-C_{10},[31] BODIPY-Lys exhibits two absorption bands: a low-intensity band in the 300−400 nm region and a main band in the 450−525 nm region (Figure 2A). The fluorescence spectra of BODIPY-Lys display a minor red shift as the solvent polarity increases, with the fluorescence peak maximum shifting from 522 nm in cyclohexane to 525 nm in DMSO (Figure 2A). The absence of red-shifted bands in the fluorescence spectra demonstrates that BODIPY-Lys does not form aggregates or dimers in either polar or nonpolar solvents, unlike many other BODIPY dyes.[42]

To assess how solvent polarity influences the fluorescence lifetimes of BODIPY-Lys, we performed time-resolved fluorescence measurements in cyclohexane, toluene, chloroform, dichloromethane, methanol, and DMSO (Figures 2B and S1). BODIPY-Lys exhibited monoexponential fluorescence decays in all solvents, with lifetimes ranging from 126 ps in cyclohexane to 138 ps in DMSO. The correlation between the solvent polarity and fluorescence lifetimes was marginal, with only slight variations across solvents. For instance, BODIPY-Lys displayed lifetimes of 71 ps in methanol (0.63 cP), 116 ps in dichloromethane (0.43 cP), and 151 ps in chloroform (0.56 cP), indicating minimal dependence on solvent polarity (Figure S1). In contrast, the fluorescence lifetimes of BODIPY-C_{10} range from 300 to 800 ps in low-viscosity solvents of varying polarities.[31]

To evaluate the viscosity sensitivity of BODIPY-Lys and construct a fluorescence lifetime-viscosity calibration curve, we performed time-resolved and steady-state fluorescence measurements of BODIPY-Lys in methanol−glycerol mixtures spanning a viscosity range from 0.6 to 1457 cP (Figures 2C and S2). This calibration curve enables the conversion of BODIPY-Lys fluorescence lifetimes in lysosomal membranes into universal viscosity values, facilitating comparisons to other microviscosity measurements in various organelles. BODIPY-Lys displays excellent viscosity sensitivity, with fluorescence lifetimes ranging from 71 ps in methanol (0.6 cP) to 4545 ps in pure glycerol (1457 cP) (Figure 2C,D). The fluorescence decays of BODIPY-Lys were monoexponential in methanol/glycerol mixtures up to 50% glycerol. Beyond 60% glycerol, BODIPY-Lys exhibited biexponential decays with a low-amplitude, short-lifetime component (Figure S2). Furthermore, BODIPY-Lys displays a broader dynamic viscosity range than BODIPY-C10, owing to its lower fluorescence lifetime values in nonviscous solvents. The dynamic viscosity range, which can be calculated from the fluorescence lifetime ratio at high and low viscosities, is 64.0 for BODIPY-Lys in methanol−glycerol mixtures, compared to 11.2 for BODIPY-C10 in the same mixture.[31]

To assess whether the protonation of the morpholine group affects the photophysical properties of BODIPY-Lys—an important factor at the acidic pH of lysosomes—we conducted steady-state and time-resolved fluorescence measurements in methanol, ethanol, and isopropyl alcohol with added sulfuric acid (Figure S3). The protonation of morpholine did not significantly affect the fluorescence lifetimes or intensities, with changes in fluorescence lifetimes limited to only a few picoseconds following the addition of sulfuric acid (Figure S3).

Finally, since BODIPY dyes occasionally display temperature sensitivity,[43] which could interfere with their use at physiological temperatures, we quantitatively assessed BODIPY-Lys's temperature sensitivity by conducting temperature-dependent fluorescence decay measurements in DMSO (Figure S4). The temperature sensitivity was evaluated using the relative sensitivity parameter S over a temperature range of 20−70 °C (eq 1).[44]

$$S = -\frac{|\delta\tau/\delta T|}{\tau} \times 100\% \quad (1)$$

The expression for S represents the percentage change in lifetime per degree of temperature change, where τ is the fluorescence lifetime and δT is the temperature change in degrees Celsius (°C). The fluorescence lifetimes of BODIPY-Lys showed minimal temperature dependence with a relative sensitivity S value of just 0.15%/°C (Figure S4). In summary, our findings confirm that the fluorescence lifetimes of BODIPY-Lys are mainly influenced by solvent viscosity, with only negligible effects from solvent polarity and temperature. This makes BODIPY-Lys a reliable probe for microviscosity measurements in biological, protein-rich environments, even at physiological temperatures.

https://doi.org/10.1021/jacsau.5c00253
JACS Au 2025, 5, 2004−2014

Given that cholesterol is distributed heterogeneously in biological membranes and lipid bilayers contain ordered nanodomains,[45] it is essential for a membrane probe to partition into both liquid-ordered (Lo) and liquid-disordered (Ld) lipid phases while accurately assessing their microviscosity. In this context, we aimed to evaluate BODIPY-Lys's ability to differentiate between Lo and Ld phases based on their microviscosity and to examine the probe's response to varying cholesterol concentrations in the Ld phase. To achieve this, we performed FLIM on BODIPY-Lys in giant unilamellar vesicles (GUVs) composed of Ld (DOPC), Lo (DOPC/DPPC/Chol), and intermediate Ld-Lo (DOPC/Chol) lipid phases.

BODIPY-Lys successfully stained both Lo and Ld lipid phases at a dye-to-lipid ratio of 1:800, displaying intensity-weighted fluorescence lifetimes of approximately 1160 ps in the Ld (DOPC) phase and 3610 ps in the Lo (DOPC/DPPC/Chol) phase (Figures 3 and S5). These fluorescence lifetimes

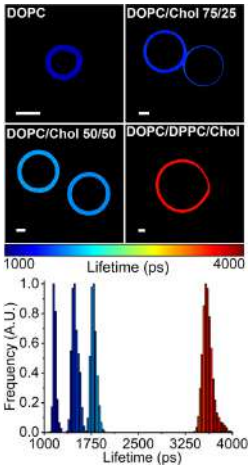

Figure 3. FLIM of BODIPY-Lys in DOPC, DOPC/Chol (75/25), DOPC/Chol (50/50), and DOPC/DPPC/Chol (1:5:5) GUVs. The corresponding BODIPY-Lys fluorescence lifetime histogram is shown in the bottom panel. Scale bars are 2 μm.

correspond to viscosities of 55 cP for DOPC and 520 cP for DOPC/DPPC/Chol and are in good agreement with both theoretically and experimentally determined values of approximately 50 cP for DOPC[46,47] and experimentally measured values of 413 ± 128 cP for the Lo phase of DOPC/DPPC/Chol.[48] By integrating into highly ordered lipid phases and displaying significant fluorescence lifetime differences between Lo and Ld phases, BODIPY-Lys can distinguish lipid phases based on their microviscosity. This capability is particularly valuable for detecting highly ordered lipid domains in lysosomal membranes.[49]

The addition of cholesterol to Ld (DOPC) GUVs led to a significant increase in the intensity-weighted fluorescence lifetimes of BODIPY-Lys, rising from 1160 ps in pure DOPC GUVs to 1490 ps (80 cP) in DOPC/Chol (75/25) GUVs and 1790 ps (130 cP) in DOPC/Chol (50/50) GUVs (Figure 3). This result is consistent with cholesterol's role in organizing and condensing Ld lipid bilayers.[50] The biexponential nature of BODIPY-Lys fluorescence decays in GUVs likely arises from the probe adopting multiple orientations within the lipid bilayer. Similarly, the transition from monoexponential decays in solvents to multiexponential decays in lipid membranes has been attributed to the adoption of multiple orientations in other BODIPY derivatives.[51,52]

Importantly, BODIPY-Lys's ability to distinguish between Lo and Ld lipid phases and accurately reflect cholesterol-induced changes in lipid order can be used to estimate cholesterol and unsaturated lipid concentrations in lysosomes as well as to study biophysical changes in lysosomal membranes upon protein binding and to image the ordering and disordering effects of small molecules.

2.3. FLIM of BODIPY-Lys in Live Human Cancerous and Noncancerous Cells

Next, we performed FLIM of BODIPY-Lys in four different human cancer lines: lung cancer (A549), glioblastoma (U-87), breast cancer (MCF-7), and liver cancer (HepG2). In all cases, BODIPY-Lys was added to the cell medium at 0.5 μM concentrations without washing, yielding excellent fluorescence intensities in the lysosomes, which were about 100 times higher compared to the cytoplasm (Figure 4). To verify the lysosomal localization of BODIPY-Lys, we performed fluorescence colocalization in HepG2 cells with fluorescent dye neutral red, a known lysosomal marker (Figure S6).[53] BODIPY-Lys displayed excellent colocalization with neutral red and effectively labeled lysosomal membranes across a broad range of lipid orders, including both highly ordered and disordered lysosomes (Figures 4 and 5). Of note, no morphological changes were observed in live cells following BODIPY-Lys staining (Figure S7), indicating low probe toxicity, consistent with the generally low toxicity of BODIPY dyes.[54] To ensure that the microviscosity measurements are accurate, we recorded the steady-state fluorescence spectra of BODIPY-Lys in lysosomes and confirmed the absence of red-shifted fluorescence bands, indicating that BODIPY-Lys does not aggregate in the lysosomal membranes and exhibits properties similar to those observed in organic solvents (Figure S8). FLIM analysis revealed that the fluorescence decays of BODIPY-Lys in lysosomal membranes were biexponential, suggesting that the probe adopts multiple orientations within the lipid bilayer, similar to its behavior in GUVs (Figures S8 and S9).

Interestingly, all investigated cancer cell lines contained moderately viscous and ordered lysosomes, with mean BODIPY-Lys intensity-weighted fluorescence lifetimes of 2730 ps (325 cP) in A549, 2150 ps (200 cP) in U-87, and 2400 ps (250 cP) in both MCF-7 and HepG2 cells (Figure 4). Notably, the number of lysosomes per cell varied significantly, with HepG2 cells having fewer but larger lysosomes compared to other cell lines. To compare lysosomal membrane microviscosities between cancerous and noncancerous cells, we performed FLIM of BODIPY-Lys in four noncancerous human cell lines: human mammary fibroblasts (HMFs), prostate myofibroblasts (WPMY-1), retinal pigment epithelium (RPE-1), and human embryonic kidney (HEK 293T) cells (Figure 5). BODIPY-Lys exhibited mean intensity-weighted fluorescence lifetimes of about 920 ps (40 cP) in HMF, 1460 ps (85 cP) in WPMY-1, 1500 ps (90 cP) in RPE-1, and 1800 ps (135 cP) in HEK 293T cells. In contrast to cancer cell lines, where lysosomal membrane microviscosities ranged from 200 to 325 cP, noncancerous cells exhibited

https://doi.org/10.1021/jacsau.5c00253
JACS Au 2025, 5, 2004−2014

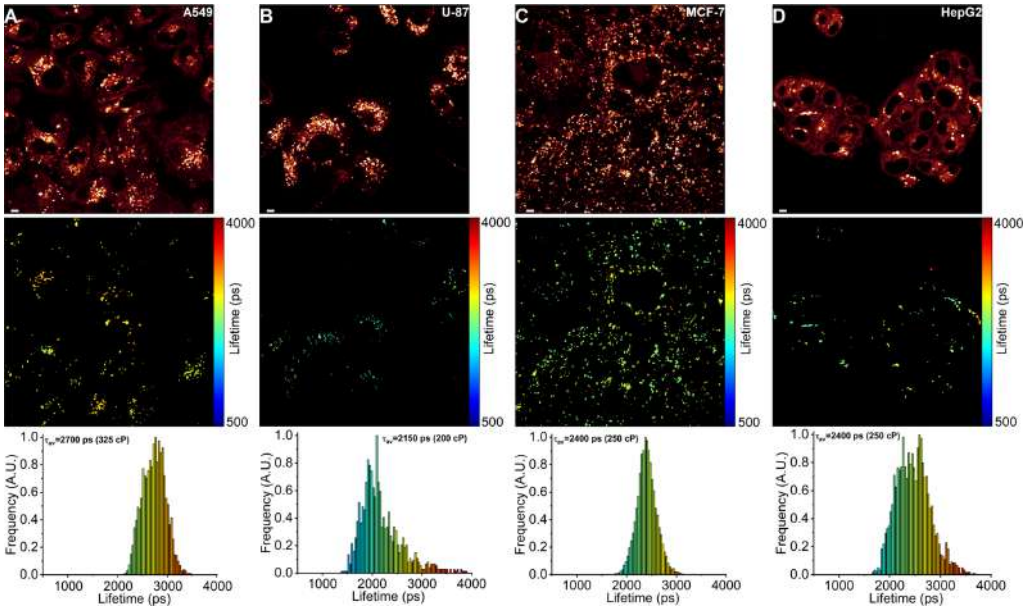

Figure 4. FLIM of BODIPY-Lys in human cancerous cell lines. (A) Human lung cancer A549. (B) Human glioblastoma U-87. (C) Human breast cancer MCF-7. (D) Human liver cancer HepG2. The top panel shows images of the fluorescence intensity. FLIM images are shown in the middle panel. The corresponding lifetime histograms with mean fluorescence lifetimes τ_{av} and corresponding viscosities in the methanol−glycerol calibration mixtures are shown in the bottom panel. Scale bars are 5 μm.

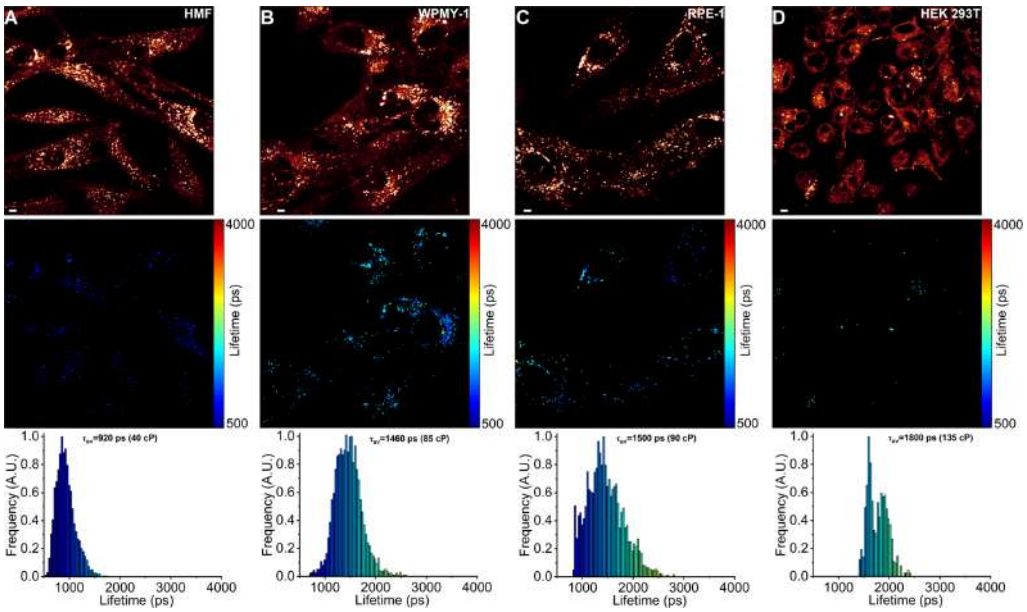

Figure 5. FLIM of BODIPY-Lys in human noncancerous cell lines. (A) HMFs. (B) Human prostate myofibroblasts WPMY-1. (C) Human retinal pigment epithelium cells RPE-1. (D) Human embryonic kidney cells HEK 293T. The top panel shows images of the fluorescence intensity. FLIM images are shown in the middle panel. The corresponding lifetime histograms with mean fluorescence lifetimes τ_{av} and corresponding viscosities in the methanol−glycerol calibration mixtures are shown in the bottom panel. Scale bars are 5 μm.

https://doi.org/10.1021/jacsau.5c00253
JACS Au 2025, 5, 2004−2014

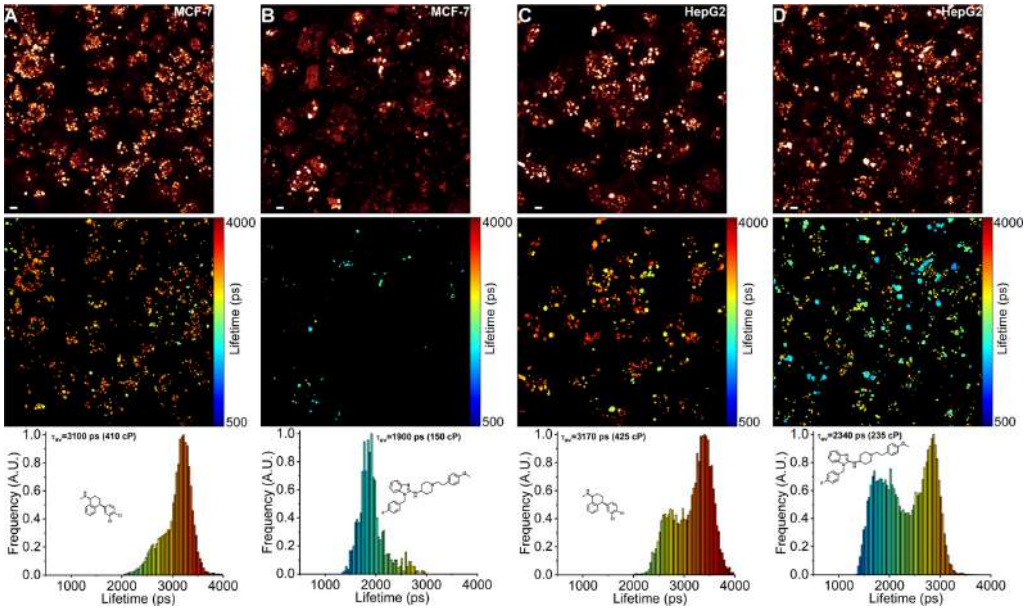

Figure 6. FLIM of BODIPY-Lys in human cancerous cell lines treated with CADs Ser and Ast. (A) MCF-7 cells treated with Ser for 24 h. (B) MCF-7 cells treated with Ast for 24 h. (C) HepG2 cells treated with Ser for 24 h. (D) HepG2 cells treated with Ast for 24 h. The top panel shows images of fluorescence intensity. FLIM images are shown in the middle panel. The corresponding lifetime histograms with CAD structures, mean fluorescence lifetimes τ_{av}, and corresponding viscosities in the methanol−glycerol calibration mixtures are shown in the bottom panel. Scale bars are 5 μm.

significantly lower lysosomal microviscosities, ranging from 40 to 135 cP. The distinct differences in BODIPY-Lys fluorescence lifetimes between cancerous and noncancerous cells indicate that lysosomal membranes in cancer cells have a much higher lipid packing efficiency and are more ordered. Additionally, the lysosomal membranes in cancerous cells, particularly in U-87 and HepG2 (Figure 4B,D), exhibited significant heterogeneity in microviscosity, both between and within individual cells, indicating that the lipid composition of each lysosome varies significantly in cancer. In contrast, lysosomes in noncancerous cells displayed a lower degree of heterogeneity (Figure 5). Given that the fluorescence lifetime response of BODIPY-Lys to viscosity is nonlinear, differences between 1000 and 2000 ps, as seen in noncancerous RPE-1 cells, result in relatively modest changes in microviscosity, from 45 to 165 cP (Figure 5C). Meanwhile, even in a relatively homogeneous cancer cell line like MCF-7, BODIPY-Lys lifetime variations from 2000 to 3000 ps correspond to much greater differences in microviscosity, ranging from 165 to 390 cP (Figure 4C).

We hypothesize that lysosomal membranes in malignant cells likely contain a higher amount of saturated lipids, which often form highly viscous Lo lipid phases. In support of this hypothesis, various studies have shown that cancer cells overexpress fatty acid synthase, which increases the production of saturated fatty acids and leads to a more saturated lipidome.[12,13] Additionally, cancer-specific signaling and metabolic abnormalities result in an increased reactive oxygen species (ROS) generation,[8] which can oxidize membrane lipids, further increasing microviscosities due to enhanced hydrogen bonding in the lipid bilayer's hydrophobic core. To confirm the presence of elevated ROS levels in our selected cell lines, we performed fluorescence intensity imaging using the commercially available ROS detection probe DCFH-DA.[55] The fluorescence intensities of DCF, the ROS-oxidation product of DCFH-DA, were approximately 5−6 times higher in the cancerous cell lines HepG2 and U-87 compared to the noncancerous HMF and WPMY-1 cells, indicating significantly elevated ROS levels in malignant cells (Figure S10). Moreover, DCF fluorescence intensities were markedly uneven in cancerous cells, whereas noncancerous cell lines exhibited more uniform fluorescence intensities. This pattern closely resembled the highly heterogeneous lysosomal microviscosities observed in cancerous HepG2 and U-87 cells, further supporting the link between ROS generation and membrane microviscosity alterations. Thus, both the greater generation of ROS and the higher saturated lipid levels likely contribute to the elevated lysosomal membrane microviscosities observed in cancerous cells. The high degree of lipid order displayed in cancerous lysosomal membranes may also be biologically significant, as changes in lipid order can affect cell signaling and alter the function of membrane proteins, such as ion channels and transporters.[56] Furthermore, highly ordered membranes may limit the passive diffusion of chemotherapeutic drugs into the lysosomes as passive diffusion is largely dependent on membrane viscosity. Crucially, the significant differences in BODIPY-Lys fluorescence lifetimes, corresponding to the large differences in microviscosities between cancerous and noncancerous lysosomes, offer potential for detecting malignant phenotypes or assessing cancer-associated cellular abnormalities.

https://doi.org/10.1021/jacsau.5c00253
JACS Au 2025, 5, 2004−2014

2.4. Imaging the Effects of CADs on Lysosomal Microviscosities

Next, we treated MCF-7, HepG2, and RPE-1 cells for 24 h with half-maximum inhibitory concentrations (IC_{50}) of two commonly used CADs, Ser (27.5 μM for MCF-7, 21 μM for HepG2, and 21.5 μM for RPE) and Ast (12.6 μM for MCF-7, 11.3 μM for HepG2, and 9 μM for RPE). The IC_{50} value represents the drug concentration required to induce 50% cell death. The IC_{50} concentrations of Ser and Ast in all investigated cell lines were determined by an MTT assay (Figure S11). Ser and Ast belong to the same class of CADs that inhibit the lysosomal enzyme sphingomyelin phosphodiesterase 1 (SMPD1),[57] responsible for the breakdown of sphingomyelin into ceramide and phosphorylcholine.[57] The inhibition of SMPD1 reduces the hydrolysis of sphingomyelin, leading to its accumulation in the lysosomes[58] and a decreased efflux of cholesterol from the lysosomes.[59] Both Ser and Ast are hypothesized to induce lysosomal membrane permeabilization, leakage, and distortion through sphingomyelin accumulation and the detergent-like effects of CADs.[60] Therefore, we expected Ser and Ast to increase lysosomal membrane microviscosities due to their ability to increase the concentrations of cholesterol and sphingomyelin, as both lipids are known for their ability to form viscous and ordered lipid phases.[14,50]

By performing FLIM of BODIPY-Lys, we observed that Ser-treated MCF-7 and HepG2 cells displayed increased lysosomal microviscosities, with mean intensity-weighted fluorescence lifetimes of BODIPY-Lys increasing from 2400 ps (250 cP) in untreated cells to 3100 ps (410 cP) and 3170 ps (425 cP) in MCF-7 and HepG2 cell lines, respectively (Figure 6A,C). Surprisingly, Ast-treated MCF-7 and HepG2 cells exhibited decreased lysosomal microviscosities, with mean intensity-weighted fluorescence lifetimes of BODIPY-Lys decreasing to about 1900 ps (150 cP) and 2340 ps (235 cP) in MCF-7 and HepG2 cell lines, respectively (Figure 6B,D). Despite both CADs being known for inducing lysosomal membrane permeabilization, leakage, and inhibition of SMPD1,[57] Ser and Ast exhibited opposite effects on the microviscosities of lysosomal membranes, with only Ast treatment resulting in less viscous, more fluid lysosomal membranes in cancer cells. The microviscosity measurements suggest that the mechanisms by which Ser and Ast permeabilize lysosomal membranes and induce lysosomal leakage may differ. We hypothesize that the different effects of Ast and Ser on the lysosomal membrane microviscosities may arise from the additional detergent-like properties of CADs.[60] In particular, larger Ast molecules with multiple lipophilic phenyl groups may integrate more easily into the lipid bilayer, exerting stronger detergent effects and creating more disordered, less viscous membranes compared to Ser. Of note, both Ser and Ast treatments resulted in larger lysosomes in cancer cells, likely due to inhibited lipid efflux and subsequent lipid accumulation (Figures 6 and S12). Moreover, in both Ser- and Ast-treated cells, lysosomes exhibited an irregular cellular distribution, formed clusters, and adopted irregular, noncircular shapes. Additionally, particularly large lysosomes in HepG2 cells showed discontinuities in BODIPY-Lys fluorescence intensities, likely due to ruptured lipid bilayers (Figures 6 and S10). We hypothesize that Ser-induced lysosomal leakage occurs through the distortion of lysosomal membranes and the formation of pores in the lipid bilayer. In contrast, Ast may induce lysosomal leakage through both the distortion and pore formation in the lysosomal membranes as well as by directly permeabilizing the lipid bilayer through the formation of an Ld lipid phase. Disordered lipid bilayers are generally more permeable to small solutes due to their increased fluidity, which allows for greater movement of molecules across the membrane.[61]

Interestingly, both Ast and Ser treatments resulted in a heterogeneous population of lysosomes with varying microviscosities in cancer cell lines (Figure 6). In both HepG2 and MCF-7, lysosomes with the highest microviscosities consistently showed reduced BODIPY-Lys accumulation, indicated by decreased fluorescence intensities relative to those of less viscous lysosomes. We attribute this reduced accumulation of BODIPY-Lys in highly viscous lysosomes to an increase in lysosomal pH rather than highly ordered membranes hindering probe penetration. This is supported by the fact that Ast-treated cancer cells, despite not displaying high lysosomal microviscosities, still showed uneven BODIPY-Lys fluorescence intensities, with more viscous lysosomes consistently displaying lower fluorescence signals (Figure 6B,D). The increase in lysosomal pH in CAD-treated cells is a well-known effect, driven in part by the basic nature of CADs and their membrane-permeabilizing effects, which facilitate the escape of H^+ ions.[62] Since BODIPY-Lys uptake is pH-dependent, its accumulation decreases in lysosomes with higher pH levels, as the morpholine group of BODIPY-Lys is less likely to become protonated. We hypothesize that the heterogeneous populations of lysosomes with two distinct microviscosities in Ast- and Ser-treated cancer cells appear due to the continuous formation of new lysosomes. As CADs increase the lysosomal pH, it is likely that lysosomes with the lowest fluorescence intensities of BODIPY-Lys have accumulated higher amounts of CADs, while lysosomes with the highest BODIPY-Lys fluorescence intensities are likely newly formed and have not yet experienced a CAD-induced pH increase. In Ser-treated cancer cells, BODIPY-Lys fluorescence lifetimes ranging from 2000 to 3000 ps likely indicate newly formed lysosomes, which share similar fluorescence lifetimes to those in untreated cells (Figure 6A,C). In contrast, lysosomes with BODIPY-Lys fluorescence lifetimes between 3000 and 4000 ps have likely accumulated significant amounts of Ser, leading to an increase in pH, reduced BODIPY-Lys fluorescence intensities, and inhibited cholesterol efflux, which in turn increase the microviscosity of lysosomal membranes. Similarly, in Ast-treated cells, lysosomes with the highest microviscosities show decreased fluorescence intensities, indicating a high accumulation of Ast (Figure 6B,D). However, unlike in Ser-treated cells, Ast treatment leads to a reduction in lysosomal microviscosity in cancer cells. We believe Ast exerts a stronger detergent-like effect on lysosomal membranes compared with Ser, initially reducing their microviscosity. Only after a significant buildup of cholesterol and sphingomyelin occurs, as a result of SMPD1 inhibition, do the fluorescence lifetimes of BODIPY-Lys rise to the 2000−3500 ps range (Figure 6B,D). Thus, Ast likely initially disrupts the lipid bilayers of lysosomal membranes through its detergent action, with the subsequent accumulation of cholesterol and sphingomyelin, leading to increased microviscosities. In contrast, Ser likely does not cause an initial disruption of the lipid bilayer, and the accumulation of cholesterol and sphingomyelin alone results in the observed increase in microviscosities.

Similar to the cancerous cell lines, a 24 h treatment of RPE-1 cells with Ser resulted in increased lysosomal microviscosities (Figure S14), with mean BODIPY-Lys fluorescence lifetimes

https://doi.org/10.1021/jacsau.5c00253
JACS Au 2025, 5, 2004−2014

increasing from 1500 ps (90 cP) to 2620 ps (300 cP). Given that the lysosomes in RPE-1 cells are nonviscous and presumably contain modest levels of saturated and oxidized lipids,[12,13] the accumulation of sphingomyelin and cholesterol following Ser treatment is likely insufficient to create the almost Lo lysosomal membranes observed in Ser-treated cancer cells. In contrast to the cancer cell lines, Ast treatment of RPE-1 cells resulted in slightly increased lysosomal microviscosities, with mean intensity-weighted fluorescence lifetimes of BODIPY-Lys increasing from 1500 ps (90 cP) to 1700 ps (120 cP). Most likely, the accumulation of sphingomyelin and cholesterol in the initially unsaturated and nonoxidized lysosomal lipid bilayer overcomes the detergent action of Ast, resulting in increased lipid bilayer microviscosities. Additionally, CAD-treated RPE-1 cells did not exhibit significant variations in lysosomal microviscosities (Figure S14), indicating that nearly all lysosomes respond similarly to the particular CAD treatment. Such microviscosity uniformity may be a result of slower lysosomal biogenesis in noncancer cells compared to malignant ones.[4] Finally, the fluorescence intensities of BODIPY-Lys in CAD-treated RPE-1 cells were uniform, suggesting that the pH values in different lysosomes are comparable (Figure S14).

3. CONCLUSIONS

In conclusion, we synthesized and investigated the photophysical properties of a new BODIPY-based molecular rotor, BODIPY-Lys. We showed that fluorescence decays of BODIPY-Lys are sensitive to viscosity over a large range, from 0.5 to 1457 cP, while remaining largely unaffected by solvent polarity and temperature. Through time-resolved fluorescence measurements on GUVs with Lo and Ld lipid phases, we demonstrated that BODIPY-Lys exhibits significantly different fluorescence lifetimes in Lo and Ld environments, enabling it to distinguish lipid phase transitions and assess cholesterol-induced changes in the Ld phase properties. Notably, BODIPY-Lys preferentially partitions into the lysosomes of live cells with minimal staining of the cytoplasm or plasma membrane. Our findings reveal that lysosomal membranes in cancerous cells exhibit about three times greater microviscosities compared to those in noncancerous cells, enabling the identification of cancerous cells through the imaging of lysosomal membrane microviscosities. Furthermore, our exploration of the effects of CADs Ser and Ast on cancerous and noncancerous cell lines has revealed that despite their functional similarity, these CAD exert opposite effects on the microviscosities of lysosomal membranes in cancerous cells, with Ser increasing the microviscosities and Ast decreasing them. Additionally, we discovered that in cancerous cells, both CADs induce two distinct populations of lysosomes with differing lipid phases, whereas CAD-treated noncancerous cells display relatively homogeneous lysosomal microviscosities. Our findings not only advance the understanding of lysosomal dynamics but also provide insights that could guide future research into the interplay between lipid composition and cellular health.

4. MATERIALS AND METHODS

4.1. Dyes, Reagents, and Solvents

The synthetic details of BODIPY-Lys, with mass and NMR spectra, are presented in the Supporting Information. NMR spectra were recorded on a Bruker Ascend 400 spectrometer (400 MHz for ^{1}H, 100 MHz for ^{13}C, 128.4 MHz for ^{11}B, 376.5 MHz for ^{19}F). NMR spectra were referenced to residual solvent peaks. HRMS spectra were recorded on a quadrupole time-of-flight mass spectrometer (micro-TOF-Q II, Bruker Daltonics). Column chromatography was performed using silica gel 60 (0.040−0.063 mm) (Merck). Thin-layer chromatography (TLC) was performed using TLC-aluminum sheets with silica gel (Merck 60 F254). Visualization was accomplished by using UV light. Melting points were determined in open capillaries with a digital melting point IA9100 series apparatus (Thermo Fisher) and were not corrected. Reagents and solvents for the organic synthesis of the BODIPY compounds were purchased directly from commercial suppliers; solvents were purified using known procedures. Stock solutions of 1 mM BODIPY-Lys were prepared in methanol or DMSO and diluted for further experiments in solvents or their mixtures. All solvents used were of spectroscopic grade and obtained from Sigma-Aldrich. DOPC, DPPC, and cholesterol were obtained from Avanti Polar Lipids. Ser and Ast were obtained from Sigma-Aldrich, and 10 mM stock solutions of Ser and Ast were prepared in DMSO and diluted for subsequent experiments. Neutral Red and DCFH-DA were purchased from Sigma-Aldrich. 10 and 5 mM stock solutions of Neutral Red and DCFH-DA were prepared in DMSO and diluted for use in live cell imaging staining.

4.2. Formation of GUVs

GUVs were formed by mixing lipids in appropriate ratios, followed by the addition of BODIPY-Lys at a dye-to-lipid ratio of 1:800. The resulting chloroform solution was then deposited onto a clean indium tin oxide (ITO) slide and evaporated under a nitrogen stream for at least 2 h. After drying, a chamber was assembled by using two ITO slides separated by a spacer and filled with a 400 mM sucrose solution. Electroformation was carried out by applying a sinusoidal voltage of 1 V at 10 Hz for 2 h, followed by a 30 min detachment phase at 2 Hz. For the DOPC/DPPC/Chol (1/5/5) mixture, electroformation was performed at an amplitude of 2.5 V and above the lipid melting temperature.

4.3. Absorption, Steady-State, and Time-Resolved Fluorescence

Absorption spectra were measured by using a Jasco V-670 spectrophotometer. Fluorescence spectra were recorded with an Edinburgh-F900 (Edinburgh Instruments) spectrophotometer using a Fianum white laser, together with band-pass filters (Thorlabs), emitting at 488 nm as an excitation source. Fluorescence decays were measured by using time-correlated single-photon counting. Fluorescence decays had 5000 counts at the peak of the decay, with a 20 ns time window and 4096 channels in the time domain. 10 mm quartz cuvettes were used for absorption and fluorescence measurements, with BODIPY-Lys concentrations of up to 2 μM. Fluorescence decays of BODIPY-Lys in solvent mixtures and pure solvents were taken at 20 °C. The instrument response function (IRF) was recorded using a scattering sample, and its full width at half-maximum was 415 ps.

4.4. Imaging of Live Cells

RPE-1, HepG2, A549, U-87, HEK 293T, MCF-7, and WPMY-1 cell lines were purchased from ATCC, and HMF cells were purchased from the National Cancer Institute of Lithuania. All of the imaged cells were cultured in Dulbecco's modified Eagle's medium supplemented with 10% fetal bovine serum (FBS), 100 IU/mL penicillin, and 100 μg/mL streptomycin (Thermo Fisher). The cells were incubated at 37 °C in 5% CO_2. Before imaging, cells were seeded into an Ibidi μ-Dish (Ibidi) at a seeding density of 10,000 cells/mL and allowed to grow for 24 h. For cell imaging, a 0.5 μM BODIPY-Lys solution (in DMSO) was added to the culture medium for 5 min at 37 °C. FLIM imaging was done at room temperature using a Leica SP8 microscope with a 63x objective (HC PL APO oil immersion, N.A. −1.4, Leica). For ROS imaging, cells were incubated with 5 μM DCFH-DA in an FBS-free medium for 30 min, followed by replacement with a fresh cell medium.

https://doi.org/10.1021/jacsau.5c00253
JACS Au 2025, 5, 2004−2014

4.5. FLIM

FLIM was done with a Leica SP8 microscope using a 63x objective (HC PL APO oil immersion, N.A. −1.4, Leica). The fluorescence decay signal was measured over the 505−550 nm range by using a 488 nm filter-supported white light laser excitation line. The FLIM images were produced in 512 × 512 pixel resolution with 128 channels in the time domain. The pixels were binned to have at least 1000 counts at the peak of the decay curve for reliable biexponential fitting. Only lysosome-containing pixels in the FLIM images were fitted. Lysosomes were identified based on their 100-fold greater fluorescence counts per pixel relative to the cytoplasm. The IRF was measured by recording the laser reflection signal on a glass coverslip.

4.6. Data Analysis

FLIM images were analyzed with FLIMFIT software (v4.6.1, Imperial College London). The biexponential fluorescence decay model with intensity-weighted mean lifetimes (eq 2) was applied for FLIM measurements:

$$\tilde{\tau} = \frac{\Sigma_i a_i \tau_i^2}{\Sigma_i a_i \tau_i} \quad (2)$$

where a_i and τ_i are the amplitudes of the individual components. The goodness-of-fit parameter (χ^2) was 1.3 or less.

■ ASSOCIATED CONTENT

Supporting Information

The Supporting Information is available free of charge at https://pubs.acs.org/doi/10.1021/jacsau.5c00253.

BODIPY-Lys spectra: fluorescence and absorption in various solvents (Figures S1 and S2); influence of protonation (Figure S3); temperature-dependent fluorescence decays in DMSO (Figure S4); NMR and HRMS (Figures S16−S20); microscopy: colocalization of BODIPY-Lys and Neutral Red (Figure S6); bright-field images after BODIPY-Lys addition (Figure S7); assessment of ROS levels (Figure S10); high-magnification images of lysosomal morphology (Figure S12); imaging of CADs in the noncancerous RPE-1 cell line (Figure S14); MTT assays (Figure S11); and synthesis of BODIPY-Lys (Figure S15) (PDF)

■ AUTHOR INFORMATION

Corresponding Author

Artūras Polita − *Department of Biospectroscopy and Bioelectrochemistry, Institute of Biochemistry, Life Sciences Center, Vilnius University, Vilnius LT-10257, Lithuania; Department of Organic Chemistry, Center for Physical Sciences and Technology, Vilnius LT-10257, Lithuania;* orcid.org/0009-0004-4944-112X; Email: arturas.polita@gmc.vu.lt

Authors

Rūta Bagdonaitė − *Department of Biospectroscopy and Bioelectrochemistry, Institute of Biochemistry, Life Sciences Center, Vilnius University, Vilnius LT-10257, Lithuania*

Rokas Žvirblis − *Department of Biothermodynamics and drug design, Institute of Biotechnology, Life Sciences Center, Vilnius University, Vilnius LT-10257, Lithuania*

Jelena Dodonova-Vaitkūnienė − *Department of Organic Chemistry, Faculty of Chemistry and Geosciences, Institute of Chemistry, Vilnius University, Vilnius LT-03225, Lithuania*

Complete contact information is available at: https://pubs.acs.org/10.1021/jacsau.5c00253

Author Contributions

CRediT: **Rūta Bagdonaitė** investigation, methodology, visualization; **Rokas Žvirblis** investigation, methodology; **Jelena Dodonova-Vaitkūnienė** investigation, methodology, writing - review & editing; **Artūras Polita** conceptualization, formal analysis, investigation, methodology, supervision, writing - original draft, writing - review & editing.

Notes

The authors declare no competing financial interest.

■ REFERENCES

(1) Ballabio, A.; Bonifacino, J. S. Lysosomes as dynamic regulators of cell and organismal homeostasis. *Nat. Rev. Mol. Cell Biol.* **2020**, *21*, 101−118.

(2) Olson, O. C.; Joyce, J. A. Cysteine cathepsin proteases: regulators of cancer progression and therapeutic response. *Nature Reviews Cancer* **2015**, *15*, 712−729.

(3) Debnath, J.; Gammoh, N.; Ryan, K. M. Autophagy and autophagy-related pathways in cancer. *Nat. Rev. Mol. Cell Biol.* **2023**, *24*, 560−575.

(4) Tang, T.; Yang, Z.; Wang, D.; Yang, X.; Wang1, J.; Li, L.; Wen, Q.; Gao, L.; Bian, X.; Yu, S. The role of lysosomes in cancer development and progression. *Cell Biosci.* **2020**, *10*, 131.

(5) Cao, M.; Luo, X.; Wu, K.; He, X. Targeting lysosomes in human disease: from basic research to clinical applications. *Signal Transduct. Target. Ther.* **2021**, *6*, 379.

(6) Iulianna, T.; Kuldeep, N.; Eric, F. The Achilles' heel of cancer: targeting tumors via lysosome-induced immunogenic cell death. *Cell Death Dis.* **2022**, *13*, 509.

(7) Pu, J.; Guardia, C. M.; Keren-Kaplan, T.; Bonifacino, J. S. Mechanisms and functions of lysosome positioning. *Journal of Cell Science* **2016**, *129*, 4329−4339.

(8) Kurz, T.; Eaton, J. W.; Brunk, U. T. Redox activity within the lysosomal compartment: implications for aging and apoptosis. *Antioxidants & Redox Signaling* **2010**, *13*, 511−523.

(9) Paez-Perez, M.; Vyšniauskas, A.; López-Duarte, I.; Lafarge, E. J.; Castro, R. L.-R. D.; Marques, C. M.; Schroder, A. P.; Muller, P.; Lorenz, C. D.; Brooks, N. J.; Kuimova, M. K. Directly imaging emergence of phase separation in peroxidized lipid membranes. *Commun. Chem.* **2023**, *6*, 15.

(10) Vyšniauskas, A.; Qurashi, M.; Kuimova, M. K. A Molecular Rotor that Measures Dynamic Changes of Lipid Bilayer Viscosity Caused by Oxidative Stress. *Chem.—Eur. J.* **2016**, *22*, 13210−13217.

(11) Borst, J. W.; Visser, N. V.; Kouptsova, O.; Visser, A. J. W. G. Oxidation of unsaturated phospholipids in membrane bilayer mixtures is accompanied by membrane fluidity changes. *Biochimica et Biophysica Acta (BBA) - Molecular and Cell Biology of Lipids* **2000**, *1487*, 61−73.

(12) Rysman, E.; Brusselmans, K.; Scheys, K.; Timmermans, L.; Derua, R.; Munck, S.; Veldhoven, P. P. V.; Waltregny, D.; Daniëls, V. W.; Machiels, J.; Vanderhoydonc, F.; Smans, K.; Waelkens, E.; Verhoeven, G.; Swinnen, J. V. De novo lipogenesis protects cancer cells from free radicals and chemotherapeutics by promoting membrane lipid saturation. *Cancer Res.* **2010**, *70*, 8117−8126.

(13) Sargeant, T. J.; Lloyd-Lewis, B.; Resemann, H. K.; Ramos-Montoya, A.; Skepper, J.; Watson, C. J. Stat3 controls cell death during mammary gland involution by regulating uptake of milk fat globules and lysosomal membrane permeabilization. *Nat. Cell Biol.* **2014**, *16*, 1057−1068.

(14) Kaiser, H.-J.; Lingwood, D.; Levental, I.; Sampaio, J. L.; Kalvodova, L.; Rajendran, L.; Simons, K. Order of lipid phases in model and plasma membranes. *Proc. Natl. Acad. Sci. U. S. A.* **2009**, *106*, 16645−16650.

(15) Bhat, O. M.; Li, P.-L. Lysosome Function in Cardiovascular Diseases. *Cell. Physiol. Biochem.* **2021**, *55*, 277−300.

(16) Schulze, H.; Sandhoff, K. Lysosomal Lipid Storage Diseases. *Cold Spring Harbor Perspectives in Biology* **2011**, *3*, a004804.

(17) Pu, J. Targeting the lysosome: Mechanisms and treatments for nonalcoholic fatty liver disease. *Journal of Cellular Biochemistry* **2022**, *123*, 1624−1633.
(18) Anand, A.; Liu, B.; Giacobini, J. D.; Maeda, K.; Rohde, M.; Jäättelä, M. Targeting lysosomes in human disease: from basic research to clinical applications. *Mol. Cancer Ther.* **2021**, *18*, 1602−1614.
(19) Aits, S.; Jäättelä, M.; Nylandsted, J. Methods for the quantification of lysosomal membrane permeabilization: A hallmark of lysosomal cell death. *Methods in Cell Biology* **2015**, *126*, 261−285.
(20) Halliwell, W. H. Cationic Amphiphilic Drug-Induced Phospholipidosis. *Toxicologic Pathology* **1997**, *25*, 53−60.
(21) Ostenfeld, M. S.; Fehrenbacher, N.; Høyer-Hansen, M.; Thomsen, C.; Farkas, T.; Jäättelä, M. Effective Tumor Cell Death by σ-2 Receptor Ligand Siramesine Involves Lysosomal Leakage and Oxidative Stress. *Cancer Res.* **2005**, *65*, 8975−8983.
(22) Ellegaard, A.-M.; Groth-Pedersen, L.; Oorschot, V.; Klumperman, J.; Kirkegaard, T.; Nylandsted, J.; Jäättelä, M. Sunitinib and SU11652 Inhibit Acid Sphingomyelinase, Destabilize Lysosomes, and Inhibit Multidrug Resistance. *Molecular Cancer Therapeutics* **2013**, *12*, 2018−2030.
(23) Petersen, N. H.; et al. Transformation-Associated Changes in Sphingolipid Metabolism Sensitize Cells to Lysosomal Cell Death Induced by Inhibitors of Acid Sphingomyelinase. *Cancer Cell* **2013**, *24*, 379−393.
(24) Polita, A.; Stancikaitė, M.; Žvirblis, R.; Maleckaitė, K.; Dodonova-Vaitkūnienė, J.; Tumkevičius, S.; Shivabalan, A. P.; Valinčius, G. Designing a green-emitting viscosity-sensitive 4,4-difluoro-4-bora-3a,4a-diaza-s-indacene (BODIPY) probe for plasma membrane viscosity imaging. *RSC Adv.* **2023**, *13*, 19257−19264.
(25) Polita, A.; Bagdonaitė, R.; Shivabalan, A. P.; Valinčius, G. Influence of Simvastatin and Pravastatin on the Biophysical Properties of Model Lipid Bilayers and Plasma Membranes of Live Cells. *ACS Biomaterials Science & Engineering* **2024**, *10*, 5714−5722.
(26) Wu, Y.; Štefl, M.; Olzyńska, A.; Hof, M.; Yahioglu, G.; Yip, P.; Casey, D. R.; Ces, O.; Humpolíčková, J.; Kuimova, M. K. Molecular rheometry: direct determination of viscosity in Lo and Ld lipid phases via fluorescence lifetime imaging. *Phys. Chem. Chem. Phys.* **2013**, *15*, 14986−14993.
(27) Zidar, J.; Merzel, F.; Hodošček, M.; Rebolj, K.; Sepčić, K.; Maček, P.; Janežič, D. Liquid-Ordered Phase Formation in Cholesterol/Sphingomyelin Bilayers: All-Atom Molecular Dynamics Simulations. *J. Phys. Chem. B* **2009**, *113*, 15795−15802.
(28) Haidekker, M. A.; Theodorakis, E. A. Molecular rotors—fluorescent biosensors for viscosity and flow. *Organic & Biomolecular Chemistry* **2007**, *5*, 1669−1678.
(29) Yin, J.; Huang, L.; Wu, L.; Li, J.; James, T. D.; Lin, W. Small molecule based fluorescent chemosensors for imaging the microenvironment within specific cellular regions. *Chem. Soc. Rev.* **2021**, *50*, 12098−12150.
(30) Kuimova, M. K. Mapping viscosity in cells using molecular rotors. *Phys. Chem. Chem. Phys.* **2012**, *14*, 12671−12686.
(31) Polita, A.; Toliautas, S.; Žvirblis, R.; Vyšniauskas, A. The effect of solvent polarity and macromolecular crowding on the viscosity sensitivity of a molecular rotor BODIPY-C10. *Phys. Chem. Chem. Phys.* **2020**, *22*, 8296−8303.
(32) Lee, S.-C.; Heo, J.; Woo, H. C.; Lee, J.-A.; Seo, Y. H.; Lee, C.-L.; Kim, S.; Kwon, O.-P. Fluorescent Molecular Rotors for Viscosity Sensors. *Chem.—Eur. J.* **2018**, *24*, 13706−13718.
(33) Kubánková, M.; López-Duarte, I.; Kiryushko, D.; Kuimova, M. K. Molecular rotors report on changes in live cell plasma membrane microviscosity upon interaction with beta-amyloid aggregates. *Soft Matter* **2018**, *14*, 9466−9474.
(34) Polita, A.; Žvirblis, R.; Dodonova-Vaitkūnienė, J.; Shivabalan, A. P.; Maleckaitė, K.; Valinčius, G. Bimodal effects on lipid droplets induced in cancer and non-cancer cells by chemotherapy drugs as revealed with a green-emitting BODIPY fluorescent probe. *J. Mater. Chem. B* **2024**, *12*, 3022−3030.
(35) López-Duarte, I.; Vu, T. T.; Izquierdo, M. A.; Bulla, J. A.; Kuimova, M. K. A molecular rotor for measuring viscosity in plasma membranes of live cells. *Chem. Commun.* **2014**, *50*, 5282−5284.
(36) Paez-Perez, M.; Kuimova, M. K. Molecular Rotors: Fluorescent Sensors for microviscosity and Conformation of Biomolecules. *Angew. Chem., Int. Ed.* **2023**, *63*, No. e202311233.
(37) Wang, L.; Xiao, Y.; Tian, W.; Deng, L. Activatable Rotor for Quantifying Lysosomal Viscosity in Living Cells. *J. Am. Chem. Soc.* **2013**, *135*, 2903−2906.
(38) Li, L.-L.; Li, K.; Li, M.-Y.; Shi, L.; Liu, Y.-H.; Zhang, H.; Pan, S.-L.; Wang, N.; Zhou, Q.; Yu, X.-Q. BODIPY-Based Two-Photon Fluorescent Probe for Real-Time Monitoring of Lysosomal Viscosity with Fluorescence Lifetime Imaging Microscopy. *Anal. Chem.* **2018**, *90*, 5873−5878.
(39) Colacurcio, D. J.; Nixon, R. A. Disorders of lysosomal acidification - the emerging role of v-ATPase in aging and neurodegenerative disease. *Ageing Research Reviews* **2016**, *32*, 75−88.
(40) Lo, C. H.; Zeng, J. Defective lysosomal acidification: a new prognostic marker and therapeutic target for neurodegenerative diseases. *Transl. Neurodegen.* **2023**, *12*, 29.
(41) Schwake, M.; Schröder, B.; Saftig, P. Lysosomal Membrane Proteins and Their Central Role in Physiology. *Traffic* **2013**, *14*, 739−748.
(42) Descalzo, A. B.; Ashokkumar, P.; Shen, Z.; Rurack, K. On the Aggregation Behaviour and Spectroscopic Properties of Alkylated and Annelated Boron-Dipyrromethene (BODIPY) Dyes in Aqueous Solution. *ChemPhotoChem.* **2020**, *4*, 120−131.
(43) Vyšniauskas, A.; Cornell, B.; Sherin, P. S.; Maleckaitė, K.; Kubánková, M.; Izquierdo, M. A.; Vu, T. T.; Volkova, Y. A.; Budynina, E. M.; Molteni, C.; Kuimova, M. K. Cyclopropyl Substituents Transform the Viscosity-Sensitive BODIPY Molecular Rotor into a Temperature Sensor. *ACS Sensors* **2021**, *6*, 2158−2167.
(44) Zhou, J.; del Rosal, B.; Jaque, D.; Uchiyama, S.; Jin, D. Advances and challenges for fluorescence nanothermometry. *Nat. Methods* **2020**, *17*, 967−980.
(45) Thelen, A. M.; Zoncu, R. Emerging Roles for the Lysosome in Lipid Metabolism. *Trends in Cell Biology* **2017**, *27*, 833−850.
(46) Fšbišn, B.; Vattulainen, I.; Javanainen, M. Protein Crowding and Cholesterol Increase Cell Membrane Viscosity in a Temperature Dependent Manner. *J. Chem. Theory Comput.* **2023**, *19*, 2630−2643.
(47) Nojima, Y.; Iwata, K. Viscosity Heterogeneity inside Lipid Bilayers of Single-Component Phosphatidylcholine Liposomes Observed with Picosecond Time-Resolved Fluorescence Spectroscopy. *J. Phys. Chem. B* **2014**, *118*, 8631−8641.
(48) Paez-Perez, M.; Dent, M. R.; Brooks, N. J.; Kuimova, M. K. Viscosity-Sensitive Membrane Dyes as Tools To Estimate the Crystalline Structure of Lipid Bilayers. *Anal. Chem.* **2023**, *95*, 12006−12014.
(49) Rodriguez-Navarro, J. A.; Kaushik, S.; Koga, H.; Dall'Armi, C.; Shui, G.; Wenk, M. R.; Paolo, G. D.; Cuervo, A. M. Inhibitory effect of dietary lipids on chaperone-mediated autophagy. *Proc. Natl. Acad. Sci. U. S. A.* **2012**, *109*, 705−714.
(50) Róg, T.; Pasenkiewicz-Gierula, M.; Vattulainen, I.; Karttunen, M. Ordering effects of cholesterol and its analogues. *Biochimica et Biophysica Acta (BBA) - Biomembranes* **2009**, *1788*, 97−121.
(51) Olšinová, M.; Jurkiewicz, P.; Pozník, M.; Šachl, R.; Prausová, T.; Hof, M.; Kozmík, V.; Teplý, F.; Svoboda, J.; Cebecauer, M. Di- and tri-oxalkyl derivatives of a boron dipyrromethene (BODIPY) rotor dye in lipid bilayers. *Phys. Chem. Chem. Phys.* **2014**, *16*, 10688−10697.
(52) Dent, M. R.; López-Duarte, I.; Dickson, C. J.; Geoghegan, N. D.; Cooper, J. M.; Gould, I. R.; Krams, R.; Bull, J. A.; Brooks, N. J.; Kuimova, M. K. Imaging phase separation in model lipid membranes through the use of BODIPY based molecular rotors. *Phys. Chem. Chem. Phys.* **2015**, *17*, 18393−18402.
(53) Repetto, G.; del Peso, A.; Zurita, J. L. Neutral red uptake assay for the estimation of cell viability/cytotoxicity. *Nat. Protoc.* **2008**, *3*, 1125−1131.

https://doi.org/10.1021/jacsau.5c00253
JACS Au 2025, 5, 2004−2014

(54) Shi, Z.; Han, X.; Hu, W.; Bai, H.; Peng, B.; Ji, L.; Fan, Q.; Li, L.; Huang, W. Bioapplications of small molecule Aza-BODIPY: from rational structural design to in vivo investigations. *Chem. Soc. Rev.* **2020**, *49*, 7533−7567.
(55) Reiniers, M. J.; van Golen, R. F.; Bonnet, S.; Broekgaarden, M.; van Gulik, T. M.; Egmond, M. R.; Heger, M. Preparation and Practical Applications of 2',7'-Dichlorodihydrofluorescein in Redox Assays. *Anal. Chem.* **2017**, *89*, 3853−3857.
(56) Escribá, P. V.; Ozaita, A.; Ribas, C.; Miralles, A.; Fodor, E.; Farkas, T.; García-Sevilla, J. A. Role of lipid polymorphism in G protein-membrane interactions: Nonlamellar-prone phospholipids and peripheral protein binding to membranes. *Proc. Natl. Acad. Sci. U. S. A.* **1997**, *94*, 11375−11380.
(57) Mir, I. H.; Thirunavukkarasu, C. The relevance of acid sphingomyelinase as a potential target for therapeutic intervention in hepatic disorders: current scenario and anticipated trends. *Arch. Toxicol.* **2023**, *97*, 2069−2087.
(58) Pagliero, R. J.; D'Astolfo, D. S.; Lelieveld, D.; Pratiwi, R. D.; Aits, S.; Jaattela, M.; Martin, N. I.; Klumperman, J.; Egan, D. A. Discovery of Small Molecules That Induce Lysosomal Cell Death in Cancer Cell Lines Using an Image-Based Screening Platform. *ASSAY and Drug Development Technologies* **2016**, *14*, 489−510.
(59) Kuzu, O. F.; Gowda, R.; Noory, M. A.; Robertson, G. P. Modulating cancer cell survival by targeting intracellular cholesterol transport. *Br. J. Cancer* **2017**, *117*, 513−524.
(60) Groth-Pedersen, L.; Jäättelä, M. Combating apoptosis and multidrug resistant cancers by targeting lysosomes. *Cancer Letters* **2013**, *332*, 265−274.
(61) Fralliciardi, J.; Melcr, J.; Siginou, P.; Marrink, S. J.; Poolman, B. Preparation and Practical Applications of 2',7'-Dichlorodihydro-fluorescein in Redox Assays. *Nat. Commun.* **2022**, *13*, 1605.
(62) Kendall, R. L.; Holian, A. Cholesterol-dependent molecular mechanisms contribute to cationic amphiphilic drugs' prevention of silica-induced inflammation. *European Journal of Cell Biology* **2023**, *102*, No. 151310.

https://doi.org/10.1021/jacsau.5c00253
JACS Au 2025, 5, 2004−2014

4th publication

Quantitative FLIM Imaging of Lipid Droplet Polarity with a BODIPY Probe Reveals Biophysical Signatures of Ferroptosis Resistance

R. Bagdonaitė, Z. Ö. Cinar, R. Žvirblis, J. Dodonova-Vaitkūnienė, and **A. Polita**

Chemical & Biomedical Imaging, 2026, 4, 867–876.

DOI: 10.1021/cbmi.5c00193

Author Contributions: Photophysical characterization of *BP-Ph-LD* in solvents of varying polarity; fluorescence lifetime imaging experiments; analysis and interpretation of spectroscopic and imaging data; preparation of figures; and writing of the original manuscript draft.

ACS Partner Journal

CHEMICAL & BIOMEDICAL IMAGING

pubs.acs.org/ChemBioImaging

Article

Quantitative FLIM of Lipid Droplet Polarity with a Deep-Red BODIPY Probe Reveals Signatures of Ferroptosis Resistance

Rūta Bagdonaitė, Zeynep Özlem Cinar, Rokas Žvirblis, Jelena Dodonova-Vaitkūnienė, and Artūras Polita*

Cite This: *Chem. Biomed. Imaging* 2026, 4, 867−876

Read Online

ACCESS | Metrics & More | Article Recommendations | Supporting Information

ABSTRACT: The efficacy of ferroptosis-based cancer therapies is often limited by acquired resistance, but the underlying adaptive mechanisms, particularly those involving lipid droplet (LD) remodeling, remain poorly understood. Existing methods for studying ferroptosis do not quantitatively capture the biophysical changes in LDs that support cell survival. Here, we report BP-Ph-LD, a red-emitting BODIPY probe that enables the quantitative mapping of LD polarity via fluorescence lifetime imaging microscopy (FLIM). Using this probe, we monitored the LD dynamics in breast cancer cells undergoing prolonged treatment with the ferroptosis inducer erastin. The resistant state was characterized by a marked decrease in LD polarity, indicating a metabolic shift toward more saturated and less oxidizable lipids. This shift coincided with spatial segregation of LDs: nonpolar LDs clustered near the nucleus, whereas more polar, peroxide-rich LDs localized at the cell periphery. Morphologically distinct, nonspherical LDs also emerged in resistant cells. In early ferroptosis, in contrast, LD polarity and positioning correlated with mitochondrial integrity, linking biophysical adaptation to organelle protection under oxidative stress. Collectively, these findings identify LD polarity as a functional biomarker for ferroptosis resistance and introduce a quantitative optical tool to investigate biophysical adaptation during drug tolerance in cancer.

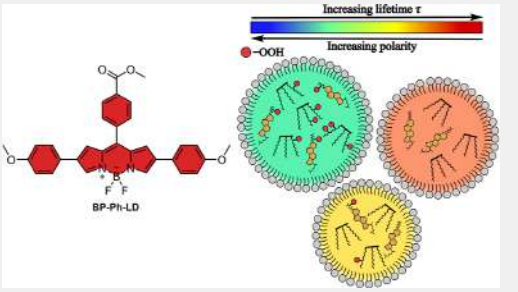

KEYWORDS: *ferroptosis, lipid droplets, fluorescence lifetime imaging microscopy, polarity, drug resistance, BODIPY*

INTRODUCTION

Lipid droplets (LDs) are cytoplasmic, lipid-rich organelles that regulate lipid storage, metabolism, and signaling in health and disease.[1,2] Composed of cholesterol esters and triacylglycerols enclosed by a phospholipid monolayer (Figure 1A), LDs can act as dynamic reservoirs that mitigate lipid peroxidation and oxidative stress.[3,4] Recent studies implicate LDs in ferroptosis,[3,5] a nonapoptotic, iron-dependent cell death pathway driven by lipid peroxidation.[6] Ferroptosis has gained significant attention in cancer biology as a potential strategy to overcome chemotherapy resistance, particularly in tumors that evade apoptosis.[7,8]

However, the efficacy of ferroptosis-inducing agents is often limited by the adaptability of the cancer cells. A subpopulation of cells can survive the initial ferroptotic insult and subsequently develop resistance, leading to treatment failure and tumor relapse.[9,10] The mechanisms that govern this transition from a ferroptosis-sensitive to a resistant state, particularly those enabling long-term survival, remain poorly understood.[10]

While the role of LDs in ferroptosis is increasingly appreciated, our ability to monitor the dynamic changes within them remains limited. Conventional fluorescent probes, such as BODIPY-C_{11}[11] and Liperfluo,[12] detect lipid peroxidation by irreversibly reacting with reactive oxygen species (ROS), offering only a transient snapshot of oxidative activity rather than a quantitative measure of the resulting lipid peroxides.[13] Because cells can neutralize ROS or repair the resulting lipid damage,[14,15] these probes fail to capture the downstream biochemical and biophysical adaptations within lipid environments that accompany the development of ferroptosis resistance.

To overcome this limitation, we hypothesized that polarity, a key biophysical parameter, could serve as a marker of ferroptosis resistance. Polarity is influenced by the chemical environment, and in the nonpolar surroundings of an LD, the incorporation of oxygen-containing functional groups, a characteristic feature of lipid peroxidation,[16] causes a significant increase in local polarity, reflecting enhanced

Received: October 13, 2025
Revised: December 2, 2025
Accepted: December 17, 2025
Published: December 22, 2025

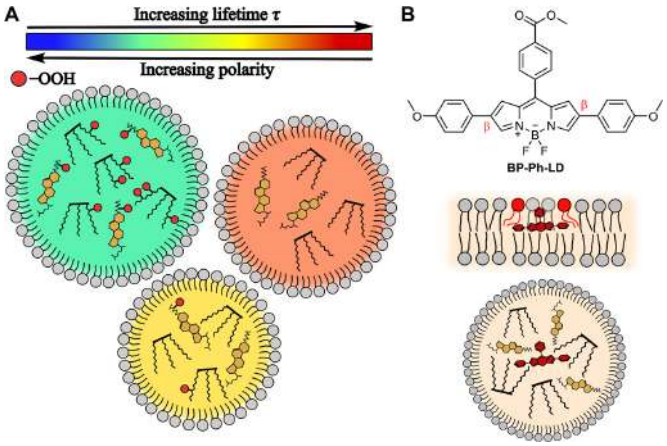

Figure 1. (A) Schematic representation of LDs, illustrating heterogeneity in polarity, which is influenced by differences in lipid peroxidation levels. (B) Chemical structure of BP-Ph-LD with proposed probe orientation in lipid bilayers and LDs.

hydrogen bonding capacity and dipolar interactions with the local medium.[17,18] By measuring the LD polarity, we can indirectly but quantitatively assess the accumulation of lipid peroxides. This approach moves beyond detecting transient ROS and provides a quantitative readout of the lipid compositional changes that underlie resistance.

Here, we introduce BP-Ph-LD (Figure 1B), a red-emitting BODIPY polarity probe specifically optimized for quantitative imaging using fluorescence lifetime imaging microscopy (FLIM). Unlike intensity-based measurements, the fluorescence lifetime is an intrinsic photophysical property that remains unaffected by probe concentration, photobleaching, or signal inhomogeneity, enabling quantitative, calibration-free imaging in live cells. We characterized BP-Ph-LD and confirmed that its fluorescence lifetime is sensitive to solvent polarity but remains insensitive to viscosity or temperature.

Using BP-Ph-LD with FLIM, we tracked LD polarity dynamics in MDA-MB-231 breast cancer cells during extended treatment with the ferroptosis inducer erastin.[19] FLIM revealed a dynamic adaptation process during resistance development. Over time, LDs reorganized spatially: nonpolar LDs localized near the nucleus, while polar, peroxide-rich LDs were pushed to the periphery, suggesting functional segregation into lipid reservoirs and detoxification sinks. Most strikingly, we observed the emergence of nonspherical, nonpolar LDs, which may result from the accumulation of high-melting-point lipids, likely saturated or monounsaturated species.

Together, these findings highlight the value of polarity sensing as an effective strategy to resolve biophysical heterogeneity in LDs and identify polarity-based signatures of ferroptosis resistance. BP-Ph-LD enables this through a lifetime-based readout, offering a sensitive optical tool to study lipid-based survival strategies in resistant cancer cells.

RESULTS AND DISCUSSION

Probe Design

We based our probe design on a BODIPY core, a widely used scaffold for imaging lipid environments in LDs,[20] lysosomes,[21] the plasma membrane,[22,23] and mitochondria.[24] While most BODIPY dyes function as environment-insensitive fluorophores, a subset has been engineered as molecular rotors, where fluorescence lifetime responds to local viscosity.[25] Building on this framework, we aimed to eliminate viscosity sensitivity while enhancing the responsiveness to environmental polarity.

To achieve this, we introduced two phenyl groups at the β-positions of the BODIPY core (Figure 1B). This substitution suppresses the intramolecular rotation responsible for viscosity-dependent fluorescence and extends conjugation, promoting red-shifted emission and polarity sensitivity.[26] Additional methoxy and ester groups establish a modest push−pull electronic effect and improve the aqueous solubility for live-cell imaging.

Beyond electronic tuning, we aimed to improve LD selectivity by modulating the molecular geometry. In contrast to lipid bilayers, where phospholipids are vectorially organized with headgroups and acyl chains aligned directionally and packed tightly, LDs consist of disordered triacylglycerols that lack orientational constraints. We reasoned that nonplanar probes would disrupt the ordered packing of bilayers by forcing lipid tails to bend around bulky substituents, creating an energetic barrier to insertion (Figure 1B). In BP-Ph-LD, the methoxyphenyl groups adopt a tilted conformation relative to the BODIPY plane,[27] producing a cross-like, nonplanar architecture. We hypothesized that this nonplanar shape would be energetically disfavored within the highly ordered anisotropic environment of membranes, yet readily accommodated by the isotropic, disordered interior of LDs.

While prior LD-targeting strategies have emphasized hydrophobicity,[20,28,29] our findings highlight that nonplanar molecular geometry is a key, and perhaps underappreciated, design parameter for achieving exceptional LD selectivity by exploiting the unique disordered, nonvectorial lipid environment. The synthesis of BP-Ph-LD is provided in the Supporting Information.

Absorption, Steady-State, and Time-Resolved Fluorescence

We investigated the photophysical properties of BP-Ph-LD to assess its suitability as a polarity sensor in biological environments. For this purpose, we conducted absorption,

https://doi.org/10.1021/cbmi.5c00193
Chem. Biomed. Imaging 2026, 4, 867−876

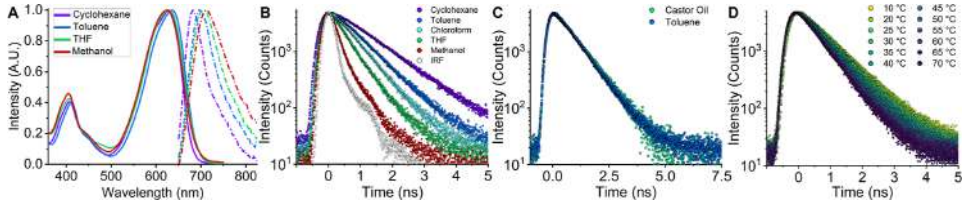

Figure 2. Photophysical characterization of BP-Ph-LD. (A) Absorption (solid lines) and fluorescence (dot-dashed lines) spectra of BP-Ph-LD in cyclohexane, toluene, THF, and methanol. (B) Time-resolved fluorescence decays of BP-Ph-LD in cyclohexane, toluene, chloroform, THF, and methanol. (C) Time-resolved fluorescence decays of BP-Ph-LD in castor oil and toluene. (D) Temperature-dependent time-resolved fluorescence decays of BP-Ph-LD in toluene.

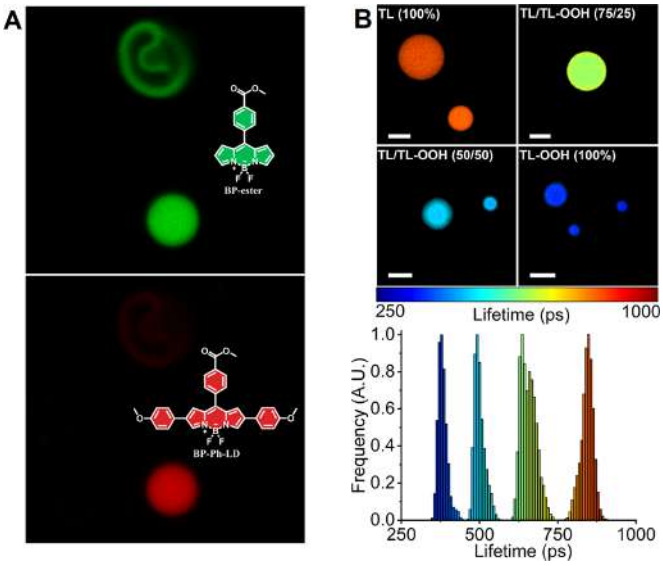

Figure 3. (A) Fluorescence intensity images of BP-ester (green, top) and BP-Ph-LD (red, bottom) the mixed aLD/MLV system. (B) FLIM images of BP-Ph-LD in aLDs with different lipid peroxide content, with the corresponding fluorescence lifetime histograms shown below. Scale bars: 5 μm.

steady-state, and time-resolved fluorescence measurements in solvents of varying polarities, viscosities, and temperatures (Figure 2). Like many other BODIPY derivatives, BP-Ph-LD exhibits two distinct absorption bands: a primary one in the visible region (500−700 nm) and a weaker, higher-energy band at 375−450 nm (Figure 2A). However, in contrast to conventional green-emitting *meso*-phenyl BODIPY dyes,[22,30] both bands are notably red-shifted. This shift primarily arises from extended π-conjugation introduced by additional phenyl substituents on the BODIPY core and is further enhanced by the modest push−pull character of the methoxyphenyl donor and ester acceptor groups. The probe shows minimal negative solvatochromism in absorption, with the peak maximum shifting only slightly from 630 nm (cyclohexane) to 626 nm (methanol). This polarity-independent absorption is a key advantage, ensuring consistent excitation efficiency across diverse cellular environments.

In contrast, the fluorescence emission of BP-Ph-LD is both polarity-sensitive and strongly red-shifted compared with conventional BODIPY dyes. The emission spectrum spans the far-red region (650−850 nm), with a moderate solvatochromic shift from 682 nm in nonpolar cyclohexane to 713 nm in polar methanol (Figure 2A). In toluene, the fluorescence quantum yield of BP-Ph-LD was determined to be Φ = 9.3% using Nile Blue in ethanol (Φ = 27%) as the reference standard (Figure S1).[31] This far-red fluorescence represents a substantial departure from the green fluorescence typical of most BODIPY derivatives and is particularly advantageous for biological imaging due to its deeper tissue penetration, lower autofluorescence, and reduced phototoxicity. To quantify this polarity dependence, we performed time-resolved fluorescence measurements in a series of solvents (Figures 2B and S2). BP-Ph-LD exhibited monoexponential decays that shortened dramatically from 1025 ps in cyclohexane to 178 ps in methanol. We used the Lippert−Mataga polarity parameter (Δf, eq 1), which combines the solvent's dielectric constant (ε) and refractive index (n) into a single value, to establish a calibration curve for converting measured lifetimes into standardized polarity values (Figure S3).

$$\Delta f = \frac{\varepsilon - 1}{2\varepsilon + 1} - \frac{n^2 - 1}{2n^2 + 1} \quad (1)$$

https://doi.org/10.1021/cbmi.5c00193
Chem. Biomed. Imaging 2026, 4, 867−876

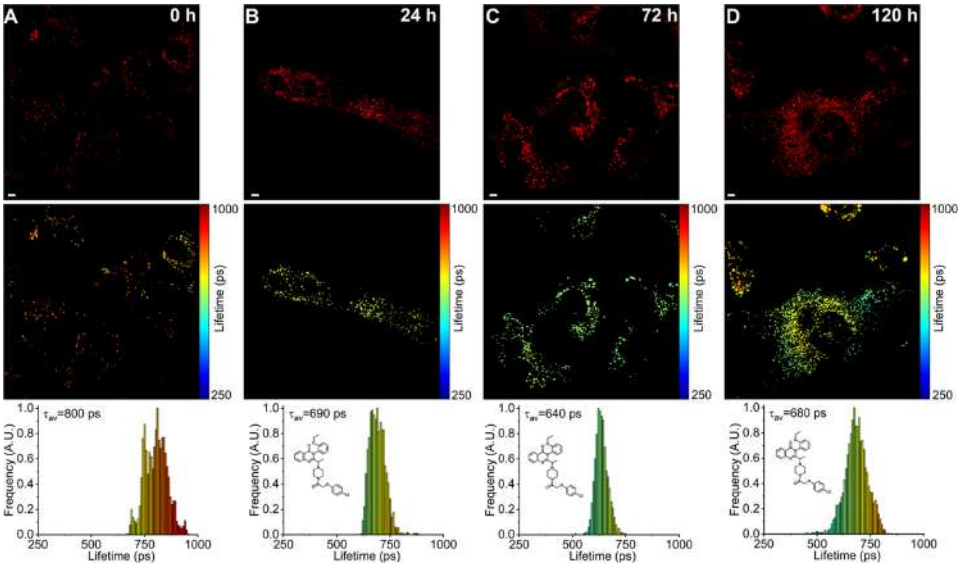

Figure 4. FLIM of BP-Ph-LD in live MDA-MB-231 human breast cancer cells. (A) Untreated cells, (B) erastin-treated for 24 h, (C) 72 h, and (D) 120 h. Top panel: fluorescence intensity images. Middle panel: FLIM maps. Bottom panel: corresponding lifetime histograms with intensity-weighted average fluorescence lifetimes (τ_{av}). Cells were stained with 250 nM BP-Ph-LD, which remained in the medium during imaging. Scale bars: 5 μm.

Many BODIPY dyes display fluorescence lifetime sensitivity to viscosity,[30,32] which can complicate polarity measurements when the two parameters are not correlated in biological environments. We therefore assessed the viscosity dependence of BP-Ph-LD by comparing its fluorescence decay in low-viscosity toluene (η = 0.6 cP) with that in highly viscous castor oil (η = 920 cP). After correction for the natural autofluorescence of castor oil by subtracting its background decay, the resulting lifetime profile for BP-Ph-LD was nearly identical to its decay in toluene (Figure 2C). This result indicates that BP-Ph-LD's fluorescence lifetime is insensitive to viscosity, effectively isolating its response to changes in polarity.

Finally, we evaluated the probe's temperature sensitivity, as the fluorescence lifetime of some BODIPY derivatives can be inherently temperature-dependent.[33] We measured fluorescence decays in toluene across a 10−70 °C range (Figure 2D) and calculated the relative sensitivity (S, eq 2), defined as the change in lifetime ($\delta\tau$) per degree of temperature change (δT).[34] Although the lifetime decreased from 759 ps (10 °C) to 499 ps (70 °C), the decays remained monoexponential throughout the temperature range. This corresponds to a low sensitivity value of S = 0.6%/°C, confirming that physiological temperature variations are unlikely to interfere with the polarity measurements.

$$S = \frac{|\delta\tau/\delta T|}{\tau} \times 100\% \quad (2)$$

Validating LD Selectivity and Lipid Peroxidation Response

To evaluate BP-Ph-LD as an LD probe, we assessed two key characteristics: selectivity for LDs over phospholipid bilayers and polarity-sensitive fluorescence lifetime response to lipid peroxidation. BP-Ph-LD was designed with methoxyphenyl substituents at the β-positions of the BODIPY core to enhance polarity sensitivity and red-shift emission, while reducing bilayer affinity by disrupting the planar packing of phospholipids (Figure 1B).

To test this, we prepared artificial LDs (aLDs; trilinolenin/DOPC, 90/10 mol %), which are inevitably accompanied by multilamellar vesicles (MLVs) from excess DOPC. This mixed system therefore contains both neutral lipid cores and ordered phospholipid bilayers, enabling direct assessment of probe partitioning. When costained with BP-Ph-LD and a structurally related planar BODIPY-ester lacking methoxyphenyl groups,[35] BP-Ph-LD selectively accumulated in aLDs with negligible fluorescence in MLV membranes (Figure 3A, bottom). In contrast, the planar BODIPY-ester stained both environments, showing only a modest enrichment in aLDs (20% higher intensity, Figure 3A, top). These results show that LD selectivity cannot be explained by hydrophobicity alone, since both probes are highly hydrophobic. Instead, it arises from the cross-shaped geometry of BP-Ph-LD, which is energetically disfavored in tightly packed bilayers but readily accommodated in isotropic neutral lipid cores.

To test whether BP-Ph-LD reports lipid peroxidation through a lifetime response, we prepared aLDs with increasing fractions of trilinolenin peroxide (TL-OOH). FLIM measurements revealed a systematic decrease in intensity-weighted lifetime with higher TL-OOH content, from 850 ps in nonoxidized aLDs to 650 ps (75/25 TL/TL-OOH), 480 ps (50/50), and 390 ps in fully oxidized aLDs (Figure 3B). This trend is consistent with the higher polarity of the lipid peroxides. Across all lipid environments, BP-Ph-LD displayed biexponential decays. This transition from the monoexponential profiles observed in solvents to biexponential behavior in lipid assemblies is consistent with the adoption of multiple

https://doi.org/10.1021/cbmi.5c00193
Chem. Biomed. Imaging 2026, 4, 867−876

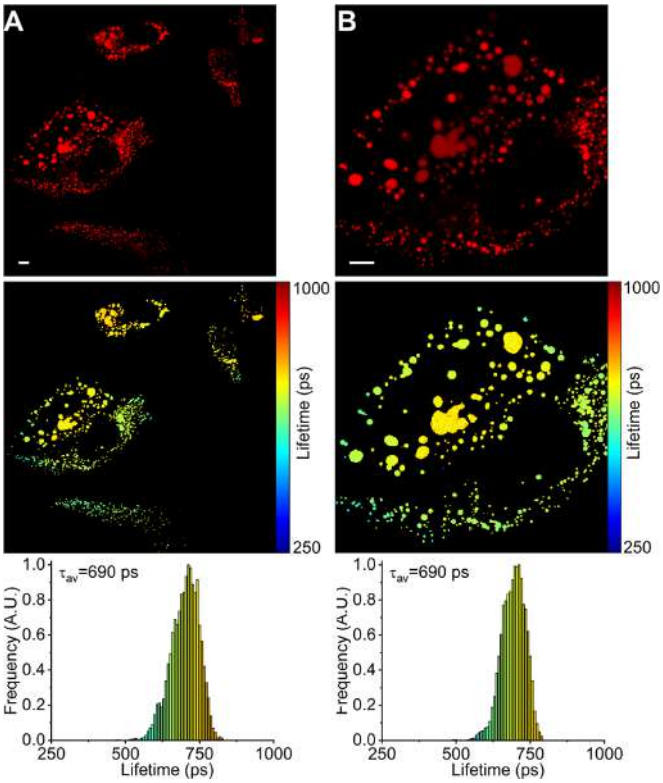

Figure 5. FLIM of BP-Ph-LD in erastin-treated live MDA-MB-231 human breast cancer cells. (A) Cells treated with erastin for 120 h. (B) High-magnification view of the same region, highlighting nonspherical LDs. Top panel: fluorescence intensity images. Middle panel: FLIM maps. Bottom panel: corresponding lifetime histograms with intensity-weighted average fluorescence lifetimes (τ_{av}). Cells were stained with 250 nM BP-Ph-LD, which remained in the medium during imaging. Scale bars: 5 μm.

probe orientations within the lipid matrix, a phenomenon previously reported for other BODIPY derivatives.[36,37] Steady-state spectra measured in LDs showed no additional bands and fluorescence maxima comparable to those of cyclohexane, supporting the absence of aggregation (Figure S4).

Together, these results demonstrate that BP-Ph-LD combines high LD selectivity, achieved through its nonplanar geometry, with clear sensitivity to polarity changes arising from lipid peroxidation. Our findings highlight the molecular shape as a critical, yet underappreciated, design parameter for next-generation LD probes.

Tracking Lipid Droplet Polarity Changes in Cells Adapting to Ferroptosis

To validate BP-Ph-LD as a live-cell LD polarity sensor, we first confirmed its targeting specificity, photophysical properties, and biocompatibility. Colocalization with the benchmark LD dye BODIPY 493/503[38] confirmed selective accumulation of BP-Ph-LD in LDs of live MDA-MB-231 cells, yielding over 100-fold higher fluorescence intensity in LDs relative to the cytoplasm (Figure S5). The probe's emission spectra in LDs closely matched those measured in organic solvents (Figure S6), and fluorescence lifetime analysis revealed biexponential decay kinetics, consistent with previous observations in model lipid systems. These results indicate that BP-Ph-LD remains monomeric within LDs and adopts multiple conformations in a lipid-rich environment. Importantly, at the working concentration (250 nM), BP-Ph-LD showed no detectable effects on cell morphology, and MTT assays performed after 24 h of probe incubation confirmed maintained cell viability at concentrations up to 5 μM, supporting its suitability for live-cell imaging (Figures S7 and S8). Before analyzing ferroptosis-induced changes in LD polarity, we confirmed that DMSO-treated cells showed no detectable changes in LD polarity relative to untreated controls and that LD polarity remained stable in cells cultured for 120 h, demonstrating that prolonged probe exposure and extended culture duration do not induce polarity drift (Figure S9). Additionally, we verified that treatment with erastin elevated ROS levels using the ROS-sensitive fluorescent probe H_2DCFDA (Figure S10).[39] Finally, treatment of cells with 25 μM of H_2O_2 for 2 or 4 h resulted in a marked decrease in BP-Ph-LD fluorescence lifetime in LDs, demonstrating that BP-Ph-LD is sensitive to oxidative conditions that are known to promote lipid peroxidation (Figure S11).[40]

Having established the probe's performance, we used BP-Ph-LD to track LD polarity dynamics during ferroptosis and adaptation to ferroptotic stress (Figure 4). In untreated cells, BP-Ph-LD reported a mean fluorescence lifetime of 800 ps,

https://doi.org/10.1021/cbmi.5c00193
Chem. Biomed. Imaging 2026, 4, 867−876

consistent with the expected low polarity of LDs under basal conditions (Figure 4A). The probe resolved modest cell-to-cell differences in the LD polarity, likely reflecting metabolic heterogeneity within the cancer cell population.

Following erastin treatment (2.2 μM, 24 h IC_{50} determined by MTT assay, Figure S12), LD polarity increased, evidenced by a decrease in lifetime to 690 ps after 24 h (Figure 4B). This likely reflects lipid peroxide accumulation, as LDs act as sinks for these reactive species.[41] Concurrently, the number of LDs increased, suggesting an acute adaptive response that sequesters lipid peroxides and buffers redox damage.

By 72 h, LDs exhibited further polarity increase (mean lifetime 640 ps) and enlarged, sometimes reaching micrometer-scale sizes (Figure 4C). This continued accumulation of polar lipids is consistent with sustained lipid peroxidation during prolonged erastin exposure and may indicate enhanced lipid storage as part of the acute adaptive response.

At 120 h, when cells had become resistant to erastin, we observed clear morphological changes: LDs became highly abundant, occupying much of the cytoplasm, and mean LD polarity partially recovered (lifetime 680 ps; Figure 4D). Parallel MTT assays indicated reduced erastin susceptibility at this stage, with IC_{50} values increasing by more than 4-fold (Figure S12).

Notably, the LD morphology also changed: many LDs adopted irregular shapes (Figures 4D and 5). To verify that these nonspherical structures were not caused by dye aggregation, we measured steady-state fluorescence spectra and time-resolved decays directly from the irregularly shaped LDs and confirmed that both photophysical signatures were consistent with those of nonaggregated BP-Ph-LD (Figure S13). Additionally, these structures persisted, even at a lower probe concentration (100 nM) (Figure S13). Normally, LDs are spherical because surface tension drives liquids to minimize their surface area.[42] The appearance of nonspherical LDs suggests a phase transition to a solid or semisolid state.[43] Despite this morphological shift, BP-Ph-LD lifetimes remained both high and spatially uniform within individual LDs, indicating that their cores still consisted of a single, predominantly nonpolar environment (Figure 5A). Additionally, high-magnification imaging confirmed that the observed phenomenon reflected a single continuous structure rather than multiple clumped LDs (Figure 5B).

Importantly, the extent of this morphological remodeling varied considerably between cells: some exhibited strongly irregular LD shapes, whereas others showed only minor distortions or maintained mostly spherical LDs (Figures 4D, 5, and S13). Moreover, even among apparently normal spherical LDs, we observed polarity gradients with more oxidized (higher polarity) LDs localizing toward the cell periphery and less oxidized LDs near the nucleus (Figure 4D). These patterns suggest that LD remodeling and redistribution may act in parallel: some LDs solidify and become inert, while others remain liquid-like and are repositioned within the cell, where peripheral, more oxidized LDs may act as sinks that isolate lipid peroxides, and central, less oxidized LDs can continue to support lipid metabolism.

We hypothesize that this morphological transformation of LDs may reflect metabolic remodeling rather than local oxidative damage. Specifically, prolonged erastin treatment could plausibly shift lipid synthesis toward saturated or monounsaturated fatty acids with higher melting points, potentially reducing the peroxidation susceptibility. As these lipids accumulate beyond their solubility limit in the LD core, LDs may undergo a phase transition into solid or semisolid states, where internal packing forces override the rounding effect of surface tension. Such irregularly shaped solidified LDs may serve as visual and biophysical markers of long-term ferroptosis resistance. While most current models focus on neutralizing or preventing lipid peroxides, our findings suggest an alternative, complementary strategy: cells adapt by fundamentally changing LD composition, replacing peroxidizable polyunsaturated fatty acids (PUFAs) with inert, saturated lipids to build a more permanent, peroxide-resistant lipid reservoir.

Previous reports propose that LDs protect cells by sequestering peroxidizable lipids away from critical membranes, thereby buffering oxidative stress.[44,45] Our observations refine this view by revealing a two-phase, time-dependent function of LDs during ferroptosis. In the acute phase of erastin-induced stress, LDs accumulate and sequester lipid peroxides, which may limit immediate membrane damage yet create a latent risk if these oxidized lipids are later mobilized. As ferroptosis progresses, LDs become spatially heterogeneous: more oxidized, high-polarity LDs localize toward the cell periphery, while less oxidized LDs remain perinuclear. This distribution likely reflects a protective diversion strategy, shuttling peroxidized lipids away from essential organelles such as mitochondria and the endoplasmic reticulum, consistent with the established role of LDs in buffering PUFA-induced lipotoxicity.[41]

In cells that survive prolonged erastin treatment, LDs undergo likely morphological remodeling, adopting nonspherical structures that are consistent with more ordered, possibly solid-like states. Such remodeling may reflect changes in lipid composition or packing that reduce the susceptibility to peroxidation. This shift suggests an adaptive metabolic response: by altering LD organization and phase behavior, cells may limit lipid peroxide accumulation and, thereby, enhance resilience under ferroptotic stress. Together, the peripheral recruitment of oxidized LDs and the emergence of irregular LD structures likely represent coordinated adaptations that mitigate oxidative damage during long-term stress. These observations highlight BP-Ph-LD's utility not only for visualizing LD polarity but also for revealing structural and metabolic signatures associated with ferroptosis resistance.

Linking Lipid Droplet Polarity to Ferroptotic Mitochondrial Changes

Recognizing that LDs closely interact with mitochondria, contribute to mitochondrial lipid balance,[1,46] and can sequester lipid peroxides,[41] while ferroptosis-induced oxidative stress leads to mitochondrial fragmentation, cristae disruption, and membrane depolarization,[8,47] we next explored whether LD polarity changes during early ferroptosis correlate with mitochondrial preservation. Although prior studies have examined LD abundance during ferroptosis,[44,45,48] the relationship between LD peroxide content, spatial distribution, and mitochondrial integrity remains poorly resolved. We hypothesized that LDs may protect mitochondria by acting as sinks for toxic lipid peroxides, with polarity shifts reflecting this protective capacity. Based on our earlier observation that LD abundance increases during ferroptosis (Figure 4), we sought to determine whether early polarity changes at 24 h coincide with differences in mitochondrial morphology. To test this, we performed dual labeling with BP-Ph-LD (250 nM) and

https://doi.org/10.1021/cbmi.5c00193
Chem. Biomed. Imaging 2026, 4, 867−876

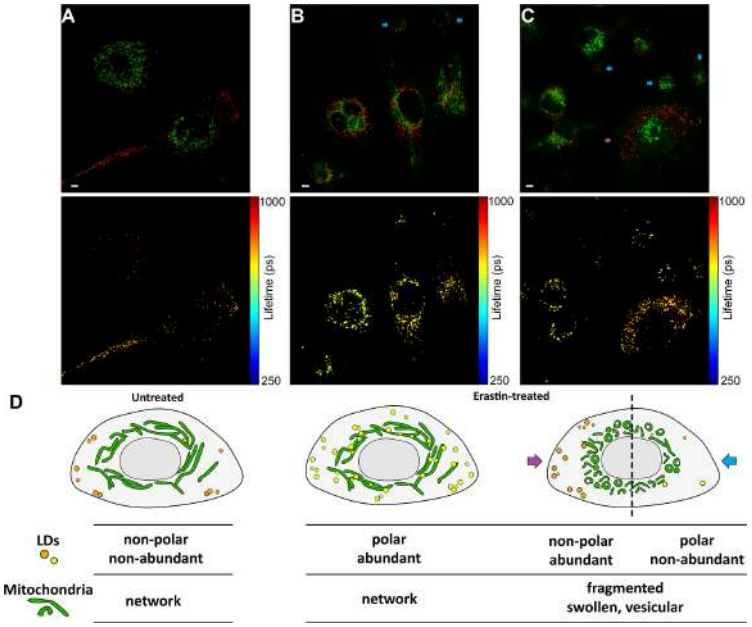

Figure 6. BP-Ph-LD and R6G imaging in live MDA-MB-231 human breast cancer cells. (A) Untreated control cells. (B,C) Cells treated with erastin for 24 h. Top panels: merged fluorescence intensity images (BP-Ph-LD, red; R6G, green). Middle panels: FLIM maps of BP-Ph-LD. (D) Cartoon representations summarizing lipid droplet polarity and mitochondrial morphology corresponding to each condition. Arrows highlight representative cells with distinct LD polarity and abundance patterns. Scale bars: 5 μm.

rhodamine 6G (R6G, 100 nM) to simultaneously visualize LD polarity (via FLIM) and mitochondrial structure (via intensity imaging) while also capturing LD-mitochondria spatial relationships (Figure 6).

In untreated MDA-MB-231 cells, mitochondria formed an elongated reticular network, while LDs were mostly nonpolar (800−850 ps) and peripherally distributed (Figure 6A). After 24 h of erastin treatment, cells diverged: some maintained relatively intact mitochondrial networks (Figure 6B), whereas others displayed pronounced swelling and fragmentation (Figure 6C). Cells with preserved mitochondria consistently exhibited abundant LDs of moderate polarity (700−800 ps), often positioned perinuclearly and in close proximity to the mitochondrial network (Figure 6B). These LDs may act as sinks for lipid peroxides, thereby limiting mitochondrial damage. In contrast, cells with abundant but nonpolar LDs (>800 ps) showed severe mitochondrial fragmentation, particularly when LDs were confined to the periphery (Figure 6C). Likewise, low LD abundance also correlated with mitochondrial disruption, even when the remaining LDs were more polar (Figure 6C).

To ensure that the observed LD−mitochondria relationships arise from ferroptotic conditions rather than general oxidative stress, we performed pretreatment with the antioxidant vitamin E, a known ferroptosis suppressor,[49−51] followed by continuous coincubation during erastin exposure. Under these conditions, cells largely preserved an elongated mitochondrial network and exhibited markedly reduced LD polarity shifts (BP-Ph-LD lifetimes of 770 ps), approaching values in untreated cells (Figure S14). Additionally, early time-point imaging confirmed that LD polarity begins to decrease before substantial mitochondrial fragmentation becomes apparent (Figure S15).

Collectively, these observations suggest that mitochondrial preservation during early ferroptosis may depend on three conditions: (i) high LD abundance, (ii) proximity of LDs to mitochondria, and (iii) uptake of lipid peroxides, as reflected in their polarity. Nonpolar LDs may simply indicate failure to acquire peroxides, leaving them within mitochondrial membranes where they promote damage. While correlative, these findings support a model in which LD remodeling contributes to mitochondrial integrity under ferroptotic stress.

■ CONCLUSIONS

In conclusion, we synthesized and characterized BP-Ph-LD, a red-emitting BODIPY-based polarity probe whose fluorescence lifetime is sensitive to solvent polarity but is largely unaffected by viscosity or temperature. The nonplanar probe design confers higher LD selectivity over lipid bilayers, enabling reliable polarity mapping in live cells. Using this probe, we showed that LD polarity increases progressively during ferroptosis, allowing the monitoring of changes in ferroptotic cells by LD-targeted lifetime imaging. At advanced stages, polarity changes were accompanied by distinct structural remodeling: some cells displayed spatial segregation of LDs, with polar LDs relocating to the periphery while less polar LDs remained perinuclear, whereas other cells developed morphologically distinct, nonspherical LDs that may reflect a transition to solid or semisolid lipid phases. Furthermore, LD polarity and positioning correlated with mitochondrial integrity, as cells enriched in perinuclear polar LDs generally preserved mitochondrial morphology, whereas those lacking such LDs

https://doi.org/10.1021/cbmi.5c00193
Chem. Biomed. Imaging 2026, 4, 867−876

displayed fragmentation and swelling. Together, these observations highlight LD polarity and morphology as markers of ferroptotic adaptation and resistance and demonstrate BP-Ph-LD as a useful tool for uncovering biophysical changes in cancer cell survival.

EXPERIMENTAL SECTION

Dyes, Reagents, and Solvents

Synthetic details of BP-Ph-LD, including NMR and HRMS spectra, are provided in the Supporting Information. NMR spectra were recorded on a Bruker Ascend 400 spectrometer (400 MHz for ^{1}H, 100 MHz for ^{13}C, 128.4 MHz for ^{11}B, and 376.5 MHz for ^{19}F) and referenced to residual solvent signals. High-resolution mass spectra (HRMS) were acquired on a quadrupole time-of-flight spectrometer (microTOF-Q II, Bruker Daltonics). Column chromatography was performed on silica gel 60 (0.040−0.063 mm, Merck). TLC was carried out on silica gel 60 F_{254} aluminum sheets (Merck) and visualized under UV light. Melting points were determined in open capillaries using a digital melting point apparatus (IA9100 series, Thermo Fisher) and are uncorrected. Reagents and solvents for BODIPY synthesis were purchased from commercial suppliers and purified by standard procedures when necessary. Stock solutions of BP-Ph-LD were prepared in toluene (2 mM) or DMSO (500 μM) and diluted with the appropriate solvents or mixtures for experiments. All solvents were of spectroscopic grade (Sigma). DOPC and trilinolenin were obtained from Avanti Polar Lipids. Stock solutions of erastin (10 mM), BODIPY 493/503 (1 mM), and α-tocopherol (10 mM) were prepared in DMSO, while rhodamine 6G (100 μM) was prepared in water; all stocks were diluted prior to use. BP-ester was synthesized as described previously.[35] For MTT viability assays, cells were seeded in a 96-well plate, allowed to attach overnight, and then treated for 24 h with varying doses of erastin or with BP-Ph-LD at the indicated concentrations. MTT reagent (Sigma) was added at a final concentration of 0.5 mg/mL and incubated for 1 h. The medium was then removed, and the formed formazan crystals dissolved in DMSO. Optical density at 570 nm was measured, and cell viability was calculated as a percentage relative to control cells.

Formation of Artificial Lipid Droplets

Artificial lipid droplets (aLDs) were prepared by mixing trilinolenin and DOPC at a 90:10 mol % ratio, followed by gentle vortexing to ensure homogeneity. For oxidized droplets, trilinolenin was first treated with 10 μM methylene blue and irradiated at 633 nm for 1 h to induce lipid peroxidation. The resulting lipid peroxides were purified by silica gel column chromatography before being mixed with DOPC.

Absorption, Steady-State, and Time-Resolved Fluorescence

Absorption spectra were recorded on a Jasco V-670 spectrophotometer. Steady-state fluorescence spectra were collected on an Edinburgh F-900 spectrometer (Edinburgh Instruments) using excitation at 633 nm (Fianum white laser). Time-resolved fluorescence decays were measured by time-correlated single-photon counting (TCSPC) with a 20 ns time window and 4096 channels, acquiring 5000 counts at the peak of the decay. Measurements were performed in 10 mm quartz cuvettes at BP-Ph-LD concentrations ≤2 μM to avoid aggregation. All fluorescence decays were recorded at 20 °C.

Imaging of Live Cells

The human breast cancer MDA-MB-231 cell line was obtained from ATCC. Cells were cultured in Dulbecco's Modified Eagle's Medium (DMEM) supplemented with 10% fetal bovine serum (FBS), 100 IU/mL penicillin, and 100 μg/mL streptomycin (Thermo Fisher). Cultures were maintained at 37 °C in a humidified atmosphere with 5% CO_2. For imaging, cells were seeded into Ibidi μ-Dishes (Ibidi) at a density of 10 000 cells/mL and allowed to grow for 24 h. BP-Ph-LD was added to the culture medium at a final concentration of 250 nM (in DMSO), and the cells were incubated for 15 min at 37 °C prior to imaging.

Fluorescence Lifetime Imaging Microscopy (FLIM)

FLIM was performed on a Leica SP8 microscope equipped with a 63× oil-immersion objective (HC PL APO, NA 1.4, Leica). Excitation was provided by the 633 nm line of a white-light laser, and fluorescence was collected in the 650−720 nm range. Images were acquired at 512 × 512 pixel resolution with 128 time channels. Pixels were binned to achieve at least 1000 counts at the decay maximum, ensuring reliable biexponential fitting. Only LD-containing pixels were analyzed; LDs were defined as regions with a 100-fold higher fluorescence intensity per pixel relative to the surrounding cytoplasm. The instrument response function (IRF) was measured from the scattered laser signal of a glass coverslip.

Data Analysis

TCSPC. Solution-phase fluorescence decays were analyzed by using the native software of the Edinburgh F900 spectrometer (Edinburgh Instruments). Decays were fitted to a monoexponential model, and fits with reduced chi-squared (χ^2) values ≤1.5 were considered acceptable.

FLIM. FLIM images were analyzed using FLIMFIT software (v4.6.1, Imperial College London). Fluorescence decays were fitted to a biexponential model, and intensity-weighted mean lifetimes were calculated according to eq 3

$$\bar{\tau} = \frac{\sum_i a_i \tau_i^2}{\sum_i a_i \tau_i} \tag{3}$$

where a_i and τ_i are the amplitude and lifetime of component i, respectively. Fits were considered acceptable when the reduced chi-squared (χ^2) value was ≤1.3.

ASSOCIATED CONTENT

Supporting Information

The Supporting Information is available free of charge at https://pubs.acs.org/doi/10.1021/cbmi.5c00193.

BP-Ph-LD photophysics: quantum yield; absorption and fluorescence spectra in various solvents; fluorescence lifetime as a function of solvent orientation polarizability; steady-state fluorescence spectra in LDs; colocalization of BP-Ph-LD and BODIPY 493/503; brightfield images after BP-Ph-LD addition; cell viability assays; synthesis of BP-Ph-LD; and NMR and HRMS (PDF)

AUTHOR INFORMATION

Corresponding Author

Artūras Polita − *Department of Biospectroscopy and Bioelectrochemistry, Institute of Biochemistry, Life Sciences Center, Vilnius University, Vilnius LT-10257, Lithuania; Department of Organic Chemistry, Center for Physical Sciences and Technology, Vilnius LT-10257, Lithuania;* orcid.org/0009-0004-4944-112X; Email: arturas.polita@gmc.vu.lt

Authors

Rūta Bagdonaitė − *Department of Biospectroscopy and Bioelectrochemistry, Institute of Biochemistry, Life Sciences Center, Vilnius University, Vilnius LT-10257, Lithuania*

Zeynep Özlem Cinar − *Department of Biospectroscopy and Bioelectrochemistry, Institute of Biochemistry, Life Sciences Center, Vilnius University, Vilnius LT-10257, Lithuania*

https://doi.org/10.1021/cbmi.5c00193
Chem. Biomed. Imaging 2026, 4, 867−876

Rokas Žvirblis − *Department of Biothermodynamics and Drug Design, Institute of Biotechnology, Life Sciences Center, Vilnius University, Vilnius LT-10257, Lithuania*

Jelena Dodonova-Vaitkūnienė − *Department of Organic Chemistry, Faculty of Chemistry and Geosciences, Institute of Chemistry, Vilnius University, Vilnius LT-03225, Lithuania*

Complete contact information is available at: https://pubs.acs.org/10.1021/cbmi.5c00193

Notes

The authors declare no competing financial interest.

REFERENCES

(1) Olzmann, J. A.; Carvalho, P. Dynamics and functions of lipid droplets. *Nat. Rev. Mol. Cell Biol.* **2019**, *20*, 137−155.
(2) Onal, G.; Kutlu, O.; Gozuacik, D.; Dokmeci Emre, S. Lipid Droplets in Health and Disease. *Lipids Health Dis.* **2017**, *16*, 128.
(3) Lee, H.; Horbath, A.; Kondiparthi, L.; Meena, J. K.; Lei, G.; Dasgupta, S.; Liu, X.; Zhuang, L.; Koppula, P.; Li, M.; et al. Cell cycle arrest induces lipid droplet formation and confers ferroptosis resistance. *Nat. Commun.* **2024**, *15*, 79.
(4) Lin, Z.; Liu, J.; Kang, R.; Yang, M.; Tang, D. Lipid Metabolism in Ferroptosis. *Adv. Biol.* **2021**, *5*, 2100396.
(5) Liang, D.; Minikes, A. M.; Jiang, X. Ferroptosis at the intersection of lipid metabolism and cellular signaling. *Mol. Cell* **2022**, *82*, 2215−2227.
(6) Dixon, S. J.; Olzmann, J. A. The cell biology of ferroptosis. *Nat. Rev. Mol. Cell Biol.* **2024**, *25*, 424−442.
(7) Wang, Y.; Wu, X.; Ren, Z.; Li, Y.; Zou, W.; Chen, J.; Wang, H. Overcoming cancer chemotherapy resistance by the induction of ferroptosis. *Drug Resist. Updates* **2023**, *66*, 100916.
(8) Liu, Y.; Lu, S.; Wu, L. l.; Yang, L.; Yang, L.; Wang, J. The diversified role of mitochondria in ferroptosis in cancer. *Cell Death Dis.* **2023**, *14*, 519.
(9) Zhang, X.; Li, X.; Xia, R.; Zhang, H.-S. Ferroptosis resistance in cancer: recent advances and future perspectives. *Biochem. Pharmacol.* **2024**, *219*, 115933.
(10) Friedmann Angeli, J. P.; Krysko, D. V.; Conrad, M. Ferroptosis at the crossroads of cancer-acquired drug resistance and immune evasion. *Nat. Rev. Cancer* **2019**, *19*, 405−414.
(11) Drummen, G. P. C.; van Liebergen, L. C.; den Kamp, J. A. O.; Post, J. A. C11-BODIPY$^{581/591}$, an oxidation-sensitive fluorescent lipid peroxidation probe: (micro)spectroscopic characterization and validation of methodology. *Free Radical Biol. Med.* **2002**, *33*, 473−490.
(12) Yamanaka, K.; Saito, Y.; Sakiyama, J.; Ohuchi, Y.; Oseto, F.; Noguchi, N. A novel fluorescent probe with high sensitivity and selective detection of lipid hydroperoxides in cells. *RSC Adv.* **2012**, *2*, 7894−7900.
(13) Feng, H.; Stockwell, B. R. Unsolved mysteries: How does lipid peroxidation cause ferroptosis? *PLoS Biol.* **2018**, *16*, No. e2006203.
(14) Ho, H.; Aoki, N.; Eguchi, M.; Gao, M.; Suzuki, H.; Mikami, M.; Chiba, H.; Hui, S.-P. Vitamin K2 Attenuates Mitochondrial Damage in Renal Proximal Tubular Cells. *J. Agric. Food Chem.* **2025**, *73*, 21857−21868.
(15) Kraft, V. A. N.; et al. GTP Cyclohydrolase 1/Tetrahydrobiopterin Counteract Ferroptosis through Lipid Remodeling. *ACS Cent. Sci.* **2020**, *6*, 41−53.
(16) Do, Q.; Zhang, R.; Hooper, G.; Xu, L. Differential Contributions of Distinct Free Radical Peroxidation Mechanisms to the Induction of Ferroptosis. *JACS Au* **2023**, *3*, 1100−1117.
(17) Wong-ekkabut, J.; Xu, Z.; Triampo, W.; Tang, I.-M.; Peter Tieleman, D.; Monticelli, L. Effect of Lipid Peroxidation on the Properties of Lipid Bilayers: A Molecular Dynamics Study. *Biophys. J.* **2007**, *93*, 4225−4236.
(18) M'Baye, G.; Mély, Y.; Duportail, G.; Klymchenko, A. S. Liquid Ordered and Gel Phases of Lipid Bilayers: Fluorescent Probes Reveal Close Fluidity but Different Hydration. *Biophys. J.* **2008**, *95*, 1217−1225.
(19) Co, H. K. C.; Wu, C.-C.; Lee, Y.-C.; Chen, S. h. Emergence of large-scale cell death through ferroptotic trigger waves. *Nature* **2024**, *631*, 654−662.
(20) Polita, A.; Žvirblis, R.; Dodonova-Vaitkūnienė, J.; Shivabalan, A. P.; Maleckaitė, K.; Valinčius, G. Bimodal effects on lipid droplets induced in cancer and non-cancer cells by chemotherapy drugs as revealed with a green-emitting BODIPY fluorescent probe. *J. Mater. Chem. B* **2024**, *12*, 3022−3030.
(21) Bagdonaitė, R.; Žvirblis, R.; Dodonova-Vaitkūnienė, J.; Polita, A. Cancer Cell Identification via Lysosomal Membrane Microviscosities Using a Green-Emitting BODIPY Molecular Rotor. *JACS Au* **2025**, *5*, 2004−2014.
(22) Polita, A.; Stancikaitė, M.; Žvirblis, R.; Maleckaitė, K.; Dodonova-Vaitkūnienė, J.; Tumkevičius, S.; Shivabalan, A. P.; Valinčius, G. Designing a green-emitting viscosity-sensitive 4,4-difluoro-4-bora-3a,4a-diaza-s-indacene (BODIPY) probe for plasma membrane viscosity imaging. *RSC Adv.* **2023**, *13*, 19257−19264.
(23) Polita, A.; Bagdonaitė, R.; Shivabalan, A. P.; Valinčius, G. Influence of Simvastatin and Pravastatin on the Biophysical Properties of Model Lipid Bilayers and Plasma Membranes of Live Cells. *ACS Biomater. Sci. Eng.* **2024**, *10*, 5714−5722.
(24) Yang, Z.; He, Y.; Lee, J.-H.; Park, N.; Suh, M.; Chae, W.-S.; Cao, J.; Peng, X.; Jung, H.; Kang, C.; Kim, J. S. A Self-Calibrating Bipartite Viscosity Sensor for Mitochondria. *J. Am. Chem. Soc.* **2013**, *135*, 9181−9185.
(25) Paez-Perez, M.; Kuimova, M. K. Molecular Rotors: Fluorescent Sensors for Microviscosity and Conformation of Biomolecules. *Angew. Chem., Int. Ed.* **2024**, *63*, No. e202311233.
(26) Žvirblis, R.; Maleckaitė, K.; Dodonova-Vaitkūnienė, J.; Jurgutis, D.; Žilėnaitė, R.; Karabanovas, V.; Tumkevičius, S.; Vyšniauskas, A. A red-emitting thiophene-modified BODIPY probe for fluorescence lifetime-based polarity imaging of lipid droplets in living cells. *J. Mater. Chem. B* **2023**, *11*, 3919−3928.
(27) Gómez-Durán, C. F. A.; Esnal, I.; Valois-Escamilla, I.; Urías-Benavides, A.; Bañuelos, J.; López Arbeloa, I.; García-Moreno, I.; Peña-Cabrera, E. Near-IR BODIPY Dyes à la Carte—Programmed Orthogonal Functionalization of Rationally Designed Building Blocks. *Chem.—Eur. J.* **2016**, *22*, 1048−1061.
(28) Collot, M.; Fam, T. K.; Ashokkumar, P.; Faklaris, O.; Galli, T.; Danglot, L.; Klymchenko, A. S. Ultrabright and Fluorogenic Probes for Multicolor Imaging and Tracking of Lipid Droplets in Cells and Tissues. *J. Am. Chem. Soc.* **2018**, *140*, 5401−5411.
(29) Zhao, Y.; Shi, W.; Li, X.; Ma, H. Recent advances in fluorescent probes for lipid droplets. *Chem. Commun.* **2022**, *58*, 1495−1509.
(30) Polita, A.; Toliautas, S.; Žvirblis, R.; Vyšniauskas, A. The effect of solvent polarity and macromolecular crowding on the viscosity sensitivity of a molecular rotor BODIPY-C_{10}. *Phys. Chem. Chem. Phys.* **2020**, *22*, 8296−8303.
(31) Sens, R.; Drexhage, K. H. Fluorescence quantum yield of oxazine and carbazine laser dyes. *J. Lumin.* **1981**, *24*−*25*, 709−712.
(32) Kuimova, M. K. Mapping viscosity in cells using molecular rotors. *Phys. Chem. Chem. Phys.* **2012**, *14*, 12671−12686.
(33) Vyšniauskas, A.; Cornell, B.; Sherin, P. S.; Maleckaitė, K.; Kubánková, M.; Izquierdo, M. A.; Vu, T. T.; Volkova, Y. A.; Budynina, E. M.; Molteni, C.; Kuimova, M. K. Cyclopropyl Substituents Transform the Viscosity-Sensitive BODIPY Molecular Rotor into a Temperature Sensor. *ACS Sens.* **2021**, *6*, 2158−2167.
(34) Zhou, J.; del Rosal, B.; Jaque, D.; Uchiyama, S.; Jin, D. Advances and challenges for fluorescence nanothermometry. *Nat. Methods* **2020**, *17*, 967−980.
(35) Cui, A.; Peng, X.; Fan, J.; Chen, X.; Wu, Y.; Guo, B. Synthesis, spectral properties and photostability of novel boron−dipyrromethene dyes. *J. Photochem. Photobiol., A* **2007**, *186*, 85−92.
(36) Dent, M. R.; López-Duarte, I.; Dickson, C. J.; Geoghegan, N. D.; Cooper, J. M.; Gould, I. R.; Krams, R.; Bull, J. A.; Brooks, N. J.; Kuimova, M. K. Imaging phase separation in model lipid membranes

through the use of BODIPY based molecular rotors. *Phys. Chem. Chem. Phys.* **2015**, *17*, 18393−18402.
(37) Olšinová, M.; Jurkiewicz, P.; Pozník, M.; Šachl, R.; Prausová, T.; Hof, M.; Kozmík, V.; Teplý, F.; Svoboda, J.; Cebecauer, M. Di- and tri-oxalkyl derivatives of a boron dipyrromethene (BODIPY) rotor dye in lipid bilayers. *Phys. Chem. Chem. Phys.* **2014**, *16*, 10688−10697.
(38) Wang, K.; Ma, S.; Ma, Y.; Zhao, Y.; Xing, M.; Zhou, L.; Cao, D.; Lin, W. Aurone Derivative Revealing the Metabolism of Lipid Droplets and Monitoring Oxidative Stress in Living Cells. *Anal. Chem.* **2020**, *92*, 6631−6636.
(39) Reiniers, M. J.; van Golen, R. F.; Bonnet, S.; Broekgaarden, M.; van Gulik, T. M.; Egmond, M. R.; Heger, M. Preparation and Practical Applications of 2',7'-Dichlorodihydrofluorescein in Redox Assays. *Anal. Chem.* **2017**, *89*, 3853−3857.
(40) Zheng, Y.; Sun, J.; Luo, Z.; Li, Y.; Huang, Y. Emerging mechanisms of lipid peroxidation in regulated cell death and its physiological implications. *Cell Death Dis.* **2024**, *15*, 859.
(41) Jarc, E.; Petan, T. A twist of FATe: Lipid droplets and inflammatory lipid mediators. *Biochimie* **2020**, *169*, 69−87.
(42) Thiam, A. R.; Farese Jr, R. V.; Walther, T. C. The biophysics and cell biology of lipid droplets. *Nat. Rev. Mol. Cell Biol.* **2013**, *14*, 775−786.
(43) Mahamid, J.; Tegunov, D.; Maiser, A.; Arnold, J.; Leonhardt, H.; Plitzko, J. M.; Baumeister, W. Liquid-crystalline phase transitions in lipid droplets are related to cellular states and specific organelle association. *Proc. Natl. Acad. Sci. U.S.A.* **2019**, *116*, 16866−16871.
(44) Chen, X.; Kang, R.; Kroemer, G.; Tang, D. Organelle-specific regulation of ferroptosis. *Cell Death Differ.* **2021**, *28*, 2843−2856.
(45) Bai, Y.; Meng, L.; Han, L.; Jia, Y.; Zhao, Y.; Gao, H.; Kang, R.; Wang, X.; Tang, D.; Dai, E. Lipid storage and lipophagy regulates ferroptosis. *Biochem. Biophys. Res. Commun.* **2019**, *508*, 997−1003.
(46) Talari, N. K.; Mattam, U.; Meher, N. K.; Paripati, A. K.; Mahadev, K.; Krishnamoorthy, T.; Sepuri, N. B. V. Lipid-droplet associated mitochondria promote fatty-acid oxidation through a distinct bioenergetic pattern in male Wistar rats. *Nat. Commun.* **2023**, *14*, 766.
(47) Li, D.; Li, Y. The interaction between ferroptosis and lipid metabolism in cancer. *Signal Transduct. Targeted Ther.* **2020**, *5*, 108.
(48) dos Santos, A. F.; Friedmann-Angeli, J. P. Troubling bonds: lipid unsaturation promotes selenium dependency and sensitivity to ferroptosis. *EMBO Mol. Med.* **2024**, *16*, 2657−2659.
(49) Hu, Q.; Zhang, Y.; Lou, H.; Ou, Z.; Liu, J.; Duan, W.; Wang, H.; Ge, Y.; Min, J.; Wang, F.; Ju, Z. GPX4 and vitamin E cooperatively protect hematopoietic stem and progenitor cells from lipid peroxidation and ferroptosis. *Cell Death Dis.* **2021**, *12*, 706.
(50) Luo, S.; Zeng, Y.; Chen, B.; Yan, J.; Ma, F.; Zhuang, G.; Hao, H.; Cao, G.; Xiao, X.; Li, S. Vitamin E and GPX4 cooperatively protect treg cells from ferroptosis and alleviate intestinal inflammatory damage in necrotizing enterocolitis. *Redox Biol.* **2024**, *75*, 103303.
(51) Hinman, A.; et al. Vitamin E hydroquinone is an endogenous regulator of ferroptosis via redox control of 15-lipoxygenase. *PLoS One* **2018**, *13*, No. e0201369.

https://doi.org/10.1021/cbmi.5c00193
Chem. Biomed. Imaging 2026, 4, 867−876

NOTES

NOTES

Artūras Polita

Design and Application of BODIPY Probes for Fluorescence Lifetime Imaging of Local Viscosity and Polarity in Lipid Microenvironments

Doctoral Dissertation
Natural Sciences
Biophysics (N 011)

Fluorescencijos gyvavimo trukmės jutiklių kūrimas ir taikymas lokalios klampos ir poliškumo vaizdinimui lipidinėse mikroaplinkose

Daktaro disertacija
Gamtos mokslai
Biofizika (N 011)

Vilnius University Press
Saulėtekio av. 9, Building III, LT-10222 Vilnius
Email: info@leidykla.vu.lt, www.leidykla.vu.lt
Print run of 15 copies